

# Robust Conformal Subcell Modeling for Electromagnetic Simulations in Time Domain



Diss. ETH No. 16969

# **Robust Conformal Subcell Modeling for Electromagnetic Simulations in Time Domain**

A dissertation submitted to the  
SWISS FEDERAL INSTITUTE OF TECHNOLOGY  
ZURICH

for the degree of  
Doctor of Sciences ETH Zürich

presented by  
STEFAN BENKLER  
Dipl. Rech. Wiss. ETH  
born June 4, 1974  
citizen of Switzerland

accepted on the recommendation of  
Prof. Dr. W. Fichtner, examiner  
Prof. Dr. N. Kuster, Prof. Dr. M. Popovic, co-examiner

2007



# Contents

<b>Summary</b>	<b>ix</b>
<b>Zusammenfassung</b>	<b>xi</b>
<b>Acknowledgments</b>	<b>xvii</b>
<b>I Background and Motivation</b>	<b>1</b>
<b>1 Introduction</b>	<b>3</b>
1.1 Motivation and Objectives . . . . .	3
1.2 Outline of Thesis . . . . .	5
<b>2 Numerical Solution of Maxwell's Equations</b>	<b>7</b>
2.1 Maxwell's Equations . . . . .	7
2.2 Numerical Methods . . . . .	8
2.2.1 Finite Differences (FDTD) . . . . .	9
2.2.2 Finite Integration Technique (FIT) . . . . .	9
2.2.3 Transmission Line Method (TLM) . . . . .	10
2.2.4 Finite-Element Time-Domain Method . . . . .	10
2.2.5 Finite-Volume Time-Domain Method . . . . .	11
2.2.6 Method of Moments (MoM) . . . . .	12
2.2.7 Generalized Multipole Technique (GMT) . . . . .	13
<b>3 Finite-Difference Time-Domain Method (FDTD)</b>	<b>15</b>
3.1 Essential Properties . . . . .	16
3.1.1 Yee Grid . . . . .	16

3.1.2	Divergence Free Nature . . . . .	18
3.1.3	Stability — Explicit Time Step . . . . .	19
3.2	Limitations of the FDTD Method . . . . .	19
3.3	Subcell Modeling . . . . .	20
3.3.1	Conformal Dielectric Models . . . . .	20
3.3.2	Conformal PEC Models . . . . .	22
3.3.3	Field Singularity Models . . . . .	24
3.4	Unconditionally Stable Methods . . . . .	24
3.4.1	Crank-Nicolson Scheme . . . . .	25
3.4.2	Alternating Direction Implicit FDTD Algorithm (ADI-FDTD) . . . . .	26
3.4.3	Subcell Enhanced ADI-FDTD Scheme . . . . .	27
<b>II Methods</b>		<b>29</b>
<b>4</b>	<b>Conformal Discretization Algorithm</b>	<b>31</b>
4.1	Abstract . . . . .	31
4.2	Introduction . . . . .	32
4.3	Method . . . . .	36
4.3.1	Modeling and CAD Import . . . . .	36
4.3.2	Generation of Grid Lines . . . . .	36
4.3.3	Discretization of Objects . . . . .	37
4.3.4	Computer-Graphic Methods . . . . .	37
4.3.5	Calculation of the Intersection . . . . .	39
4.3.6	Special Cases . . . . .	45
4.3.7	Consistency in Three Dimensions . . . . .	45
4.3.8	Conformal Merging of Different CAD Parts . . . . .	47
4.4	Conformal FDTD Method . . . . .	47
4.5	Comparison To Existing Publications . . . . .	49
4.5.1	Meshing Technique of Srisukh . . . . .	49
4.5.2	Meshing Technique of Waldschmidt . . . . .	49
4.5.3	Meshing Technique of Su . . . . .	50
4.5.4	Summary . . . . .	50
4.6	Results . . . . .	51
4.7	Conclusion . . . . .	56

<b>5</b>	<b>New 3-D Conformal PEC FDTD Scheme</b>	<b>59</b>
5.1	Abstract . . . . .	59
5.2	Introduction . . . . .	60
5.3	Method . . . . .	61
5.3.1	Proposed Algorithm . . . . .	63
5.3.2	<i>A Priori</i> Known Stability Criterion . . . . .	65
5.3.3	Short Simulation Time Versus Accuracy . . . . .	66
5.3.4	Optimal Geometric Precision for A Given Time Step . . . . .	67
5.3.5	Proposed Method Compared to Published Ones . . . . .	69
5.4	Numerical Results . . . . .	71
5.4.1	Mie Scattering of Metal Sphere . . . . .	71
5.4.2	Broadband Low Profile Antenna . . . . .	72
5.4.3	Mobile Phone . . . . .	73
5.5	Conclusion . . . . .	74
<b>6</b>	<b>Conformal Dielectric FDTD Schemes</b>	<b>79</b>
6.1	Introduction . . . . .	79
6.2	Method . . . . .	79
6.3	Results . . . . .	82
<b>7</b>	<b>Field Singularity Subcell Models</b>	<b>85</b>
7.1	Introduction . . . . .	85
7.2	Method . . . . .	85
7.3	Results . . . . .	87
<b>8</b>	<b>Subcell Model Enhanced ADI-FDTD Algorithm</b>	<b>91</b>
8.1	Abstract . . . . .	91
8.2	Method . . . . .	92
8.2.1	ADI-FDTD Coefficients Based on FDTD Coefficients . . . . .	92
8.2.2	Stability . . . . .	92
8.3	Subcell Methods . . . . .	93
8.3.1	Conformal Dielectric Model . . . . .	93
8.3.2	Conformal PEC Model . . . . .	94
8.3.3	Edge Singularity Model . . . . .	94
8.3.4	Versatile Concept for Subcell Modeling . . . . .	94
8.4	Numerical Results . . . . .	95

8.4.1	Mie Scattering . . . . .	95
8.4.2	Bent Coaxial Cable . . . . .	97
8.4.3	Patch Antenna . . . . .	99
8.5	Conclusion . . . . .	99
<b>9</b>	<b>ADI-FDTD Benchmark: NOKIA 8310</b>	<b>103</b>
9.1	Introduction . . . . .	103
9.2	Simulation Results . . . . .	105
9.3	Conclusion . . . . .	105
<b>III</b>	<b>Conclusions</b>	<b>109</b>
<b>10</b>	<b>Conclusion and Outlook</b>	<b>111</b>
<b>A</b>	<b>List of Acronyms</b>	<b>115</b>
<b>B</b>	<b>List of Symbols</b>	<b>117</b>
<b>C</b>	<b>Publications</b>	<b>121</b>
C.1	Journal Publications Included in this Thesis . . . . .	121
C.2	Other Journal Publications . . . . .	122
C.3	Other Publications . . . . .	122
	<b>Bibliography</b>	<b>125</b>
	<b>Curriculum Vitae</b>	<b>139</b>

# Summary

Rigorous competition in the sector of mobile telecommunication equipment and heavily reduced device development cycles force today's radio-frequency engineers to use new analysis and optimization tools. Through the exponential growth of computational power, technical computer aided design tools have allowed a further speedup of development cycles. In particular, the electromagnetic simulation method Finite-Difference Time-Domain (FDTD) has proven to be an efficient and flexible numerical electromagnetic (EM) solver to analyze highly complex configurations. However, the targeted applications are becoming electrically larger and involve smaller geometrical details, e.g., typically found in the medical sector: thermal ablation, applications in magnetic resonance imaging (MRI), and electromagnetic compatibility of pacemakers. These new application ranges push the capabilities of today's EM simulation platforms to the limits of computational power and memory consumption.

In spite of the prominent role of the FDTD method, inaccuracies introduced due to the staircase approximation of curved material interfaces and due to sharp edge field singularities require a (locally) fine grid resolution. Because of the explicit time integration scheme of the FDTD method, a small computational cell limits the maximal stable time step. Therefore, the simulation time can be impractically increased by resolving the geometry in detail. To counterbalance this, the *a priori* known field behavior can be incorporated into an 'intelligent' computational cell, known as the subcell modeling technique. The key point is to retrieve the same accuracy on a coarse grid using the subcell modeling technique as would be achieved on a fine mesh using the conventional FDTD scheme; thus the simulation time and

the memory consumption can be drastically reduced. Therefore, the main objective of this thesis was to investigate the efficiency of the existing subcell modeling techniques and to propose new, improved subcell models with a strong focus on robust applicability to real-world problems.

The detailed literature survey in section 3.3 revealed a broad variety of existing subcell models. However and in particular the conformal PEC models alter the conventional FDTD update equation, e.g., by splitting the common coefficient in front of the curl operator into four. Therefore, these models do not fit into the standard FDTD scheme and no stability criterion were derived. Thus, the existing models bear the potential of late time instabilities, especially when applied to real-world simulation scenarios.

Chapter 5 presents the novel conformal PEC FDTD model based on the conventional FDTD update equation but with locally modified and conformally enhanced update coefficients. The immediate benefits include the suitability of hardware acceleration and the derivation of a stability criterion. A derived stability criterion for conformal PEC subcell models is unique in the literature. Furthermore, the stability criterion was related to the accuracy of the geometrical fidelity, enabling the user to favor either a short simulation time or geometrical details depending on the controlling parameter CFL (ratio between chosen subcell time step and conventional FDTD time step). Given a time step, the best geometrical approximation is always ensured and the overall stability is maintained.

The basis of the conformal subcell models is a detailed conformal analysis of the model to simulate. Chapter 4 introduces a highly optimized algorithm to discretize arbitrarily complex models described by CAD data. Thousands of distinguished CAD parts and up to a billion computational cells are discretized within only minutes. The adaptation of computer-graphic methods to the conformal discretization algorithm greatly reduced the discretization time.

In chapter 6 a novel conformal dielectric model is introduced. The model is based on effective material parameters and takes advantage of the three-dimensional normal of the dielectric interface. The resulting effective permittivity recovers the theoretical findings of an exactly parallel and perpendicular dielectric interface normal to the electric edge. Furthermore, a comparison to existing effective permittivity

models is presented.

Chapter 7 demonstrates the reformulation of an existing field singularity subcell model with subsequent matching into the conventional update equations of the FDTD method.

The consequent reformulation of the subcell models with modified standard FDTD update coefficients provides the basis for profiting from the tremendous speedup using hardware acceleration solution. All of the FDTD subcell models derived and proposed in this thesis can profit from the speed of the hardware accelerated FDTD solver.

To overcome the time step restriction of the explicit FDTD algorithm, the unconditionally stable alternating direction implicit (ADI) time integration technique was investigated. The robustness and efficiency of the ADI-FDTD solver is demonstrated in chapter 9, reproducing a joint study with the Nokia Research Center simulating an entire CAD derived model of the mobile phone NOKIA 8310. This real-world benchmark clearly revealed that ADI-FDTD is suitable for engineering problems. Furthermore, the findings of the FDTD subcell models are adapted to the ADI-FDTD method. The proposed novel subcell modeling technique in the ADI-FDTD framework reveals the benefit in accuracy using the *a priori* known local field behavior within the updating scheme. In addition, the subcell enhanced ADI-FDTD method is equal to the conventional ADI-FDTD scheme in terms of memory and CPU consumption and should therefore always be favored over standard ADI-FDTD solvers. In chapter 8, the pioneering general approach for incorporating existing or novel subcell models into the ADI-FDTD scheme is described in detail.

Readers should note that this thesis consists of independent journal papers, resulting in unavoidable repetitions, mainly in the introductory sections of the chapters. Furthermore, a large amount of coding conducted within the framework of this thesis is not documented here.



# Zusammenfassung

Harte Konkurrenz im Bereich mobiler Telekommunikationsausrüstung resultiert in drastisch reduzierten Entwicklungszyklen um im heutigen Markt zu bestehen. Die modernen Entwicklungsingenieure sehen sich gezwungen neue Methoden für die Analyse und Optimierung der Prototypen zu suchen und anzuwenden. Die stark wachsende Rechenleistung moderner Computer sowie die Fortschritte bei CAD (Computerunterstütztes Design) Programmen helfen die Entwicklungszyklen weiter zu beschleunigen. Insbesondere die Methode FDTD (Finite Differenzen im Zeitbereich, Finite-Difference Time-Domain) zur Simulation von elektromagnetischen (EM) Feldern zeigte ihre Effizienz und Zuverlässigkeit in der Analyse von komplexen Modellen. Der Anwendungsbereich weitet sich stetig auf Modelle mit grösseren (elektrischen) Abmessungen und mit kleineren geometrischen Details aus. Beispiele im medizinischen Bereich sind thermische Abtragung von Krebsgewebe, Anwendungen in MRI (magnetic resonance imaging) sowie die elektromagnetische Verträglichkeit von Herzschrittmachern. Diese neuen Anwendungsbereiche arbeiten am Speicher- und Rechenleistungslimit heutiger EM Simulationsprogrammen.

Auch wenn die FDTD Simulationsmethode sehr häufig angewendet wird, müssen oft feine Rechengitter verwendet werden um die Genauigkeit der Lösung zu gewährleisten. Diese feinen Gitter sind zum einen nötig um gekrümmte Materialübergänge mit ihrer treppenähnlichen Annäherung im Rechengitter genügend genau nach zu bilden. Zum anderen erfordern grosse Feldgradienten, zum Beispiel in der Nähe von scharfen Metallkanten, eine lokal feine Gitterauflösung. Da die FDTD Methode eine explizite Zeitintegration verwendet, limitiert die kleinste numerische Zelle im Gitter den grössten Zeitschritt,

der die Stabilität noch garantiert. Daher kann die Simulationszeit zu drastisch verlängert werden, wenn alle geometrischen Details in die Simulation einfließen. Als Lösung zu diesem Problem kann das *a priori* bekannte Verhalten des elektrischen oder magnetischen Feldes in der Nähe von Materialübergängen und Metallkanten in eine ‘intelligente’ Rechenzelle eingeflochten werden. Diese Technik ist bekannt unter dem Namen Subzellenmodellierungstechnik (subcell modeling technique). Das Ziel ist, dass die erforderliche Genauigkeit der Lösung auf einem groben Gitter mit der Subzellentechnik erreicht wird und dadurch die Verwendung eines feines Gitters und des konventionellen FDTD Algorithmus umgangen werden kann. Die Simulationszeit und der Speicherverbrauch kann durch die Verwendung dieser Technik massiv verringert werden. Das Hauptziel dieser Dissertation war die Untersuchung der Effizienz von existierenden Subzellmodellen und die Entwicklung von neuen, verbesserten Ansätzen. Grosser Wert wurde auf die robuste Verwendbarkeit gelegt, um reale Ingenieurprobleme zu lösen.

Die detaillierte Literaturübersicht in Abschnitt 3.3 deckt die grosse Vielfalt der existierenden Subzellentechnikansätzen auf. Viele und insbesondere die Metallmodelle von gekrümmten Oberflächen verwenden eine abgeänderte Form der FDTD Updategleichungen, d.h sie teilen den gemeinsamen Koeffizienten vor dem Rotationsterm in vier individuelle Koeffizienten. Darum passen diese existierenden Modelle nicht in den herkömmlichen FDTD Algorithmus und kein Stabilitätskriterium konnte hergeleitet werden. Deshalb bergen diese Modelle das Potential, dass sie nach längerer Simulationzeit instabil werden. Im speziellen bei Simulation von komplexen CAD Modellen können diese Spätinstabilitäten auftreten.

Kapitel 5 beschreibt das neu entwickelte konforme Metall FDTD Subzellenmodell. Es basiert auf den konventionellen FDTD Updategleichungen. Die konventionellen Updatekoeffizienten werden aber lokal mit konformen Informationen berechnet und sind daher modifiziert. Der immense Vorteil liegt bei der Möglichkeit die Hardwarebeschleunigungskarten zu verwenden und dass ein Stabilitätskriterium hergeleitet werden kann. Ein hergeleitetes Stabilitätskriterium bei konformen Metallmodellen ist einzigartig in der Literatur. Überdies wurde das Stabilitätskriterium gewinnbringend benutzt um die Rechengenauigkeit mit dem geometrischen Auflösungsvermögen zu

verbinden. Dies erlaubt dem Benutzer stufenlos, d.h. abhängig von dem Kontrollparameter CFL (Verhältnis zwischen dem gewählten und konventionellen Zeitschritt), eine kurze Simulationszeit oder eine genaue geometrische Auflösung zu bevorzugen. Zu jedem gewählten Zeitschritt ist die bestmögliche geometrische Approximation gewährleistet und die Simulationsstabilität ist garantiert.

Die Grundlage von allen konformen Subzellmodellen ist eine detaillierte geometrische Analyse vom Simulationsmodell. Kapitel 4 beschreibt einen optimierten Algorithmus um komplizierte CAD basierte Modelle zu diskretisieren. Innert Minuten werden tausende von Einzelobjekten auf Gittern mit bis zu einer Milliarde Rechenzellen robust diskretisiert. Die Diskretisierungszeit konnte durch die Verwendung von Computergraphikmethoden stark reduziert werden.

Kapitel 6 beschreibt ein neues Subzellenmodell für dielektrische Materialübergänge. Das Modell verwendet die Technik der effektiven Materialparametern und die dreidimensionale Oberflächennormale des Materialüberganges. Die berechnete effektive Permittivität widerspiegelt die theoretischen Resultate von exakt parallelen und senkrechten dielektrischen Übergängen. Desweiteren werden im selben Kapitel verschiedene effektive Materialmodelle verglichen.

Kapitel 7 veranschaulicht die Reformulierung von existierenden Feldsingularitätsmodellen, um die Subzellmodelle mit den herkömmlichen FDTD Updategleichungen zu beschreiben.

Die konsequente Reformulierung von allen Subzellmodellen mit herkömmlichen Updatekoeffizienten, welche mit lokal konformen Informationen modifiziert werden, bildet das Fundament, um von der enormen Beschleunigung durch die Hardwarelösung zu profitieren. Alle Subzellmodelle, welche im Rahmen dieser Dissertation entwickelt wurden, können mit dieser neuen Hardware beschleunigt werden.

Um die Limitierung des Zeitschrittes des expliziten FDTD Verfahrens zu überwinden, wurde die unbedingt stabile Zeitintegrationsmethode ADI-FDTD (alternating direction implicit) eingehend studiert. Die Robustheit und Effizienz von diesem impliziten Verfahren wird im Kapitel 9 anhand einer Simulation eines kompletten kommerziellen Nokia 8310 Mobiltelefons demonstriert. Dieser reale Benchmark zeigte eindeutig, dass das ADI-FDTD Verfahren heutige Ingenieurprobleme lösen kann. Überdies konnten die Subzelltechnik aus der FDTD Methode auf das ADI-FDTD Schema übertragen werden.

Die Vorteile der Subzelltechnik im Rahmen des ADI-FDTD Algorithmus werden im Kapitel 8 präsentiert. Der allgemeine Ansatz zur Integration existierender und neuer Subzellmodellen ins ADI-FDTD Schema ist eine Pionierarbeit. Der Rechenaufwand und der Speicherbedarf ist zudem der gleiche für den Subzellmodell-ADI-FDTD Algorithmus wie für das herkömmliche Verfahren. Mit der verbesserten Genauigkeit sollte darum die neue Technik der Alten vorgezogen werden.

Der Leser möge berücksichtigen, dass diese Doktorarbeit aus unabhängigen Journal Publikationen besteht und darum einige Wiederholungen nicht auszuschliessen sind. Desweiteren wurde ein grosser Teil des Implementationsaufwandes nicht im Rahmen dieser Dissertation dokumentiert.

# Acknowledgments

This thesis is the result of my four years of work at the Foundation for Research on Information Technologies in Society (ITIS) and at the Bioelectromagnetics / EMC group of the Integrated Systems Laboratory (IIS) of ETH Zürich.

My sincere gratitude goes first of all to software group leader Dr. Nicolas Chavannes and the foundation leader Prof. Niels Kuster, for giving me the chance to carry out this thesis. I especially would like to thank Nik for the numerous discussions and his great support and feedback; I was able to profit greatly from his vast experience in numerical modeling and validation.

In particular, I wish to thank Prof. Wolfgang Fichtner for supervising my PhD within his excellent group. Furthermore, I wish to express my gratitude to Prof. Milica Popovic for immediately accepting being co-examiner of my thesis.

This thesis was generously supported by the Swiss Commission for Technology and Innovation (CTI) and Schmid & Partner Engineering AG (SPEAG), Switzerland. Special thanks go to Phonak, Switzerland, Motorola Electronics Private Ltd., Singapore, and Nokia Research Center NRC, Finland, for providing detailed CAD data and their friendly cooperation.

Moreover, I would like to express my gratitude to all of the people involved in the SEMCAD X project. In particular, my appreciation goes to Hansueli Gerber for his ingenious, extendable GUI framework, which was the starting point of my conformal discretization algorithm. Thanks to Emilio Cherubini; the generated conformal information is displayed with his high end `QTech` rendering engine based on `OpenGL`. In addition, using the `boost` library he interfaced the scripting lan-

guage Python, which was of great value while validating the conformal dielectric and conformal metal models. Without the integration work of Harald Songoro, the subcell algorithm could not have been implemented in a such straightforward way — thank you. Especially his pioneering work within the ADI-FDTD framework enabled the chapter about subcell modeling for this implicit method. Furthermore, I would like to thank my PhD colleagues Stefan Schild and Esra Neufeld for numerous technical and non-technical discussions. Thanks to the untiring (release) testing of Peter Futter, Erdem Ofli, and Wayne Jennings; the discretization algorithm and the subcell models profited from their valuable input. Without the porting effort of Guillermo del Castillo the kernel would only run on Windows, and Francisco Nunez, with his genetic optimization algorithm, greatly broadened the application horizon — thank you all.

Furthermore, my gratitude goes to Jürg Fröhlich and Andreas Christ for the many good discussions and valuable feedback. In addition, I want to acknowledge all of the other IT'IS members: Clementine, Veronica, Glen, Sven, Sven, Markus, Martin, Jürgen, Eugenia, Anja, Katharina, Albert, Denis, Peter, Martin. My special thanks go to Michelle Stubbs, who had the pleasure of proofreading all of my jumbled English sentences of this thesis and previous publications and to Jonathan Gubler for end-designing the posters in the nights before conferences. At this point I want to acknowledge the administrative efforts carried out by Jacqueline Pieper, Monica Lewis, Theresa Jäggin, and Sibyl Akrong. Thanks also to all IIS members, especially to Christine Haller, Dölf Aemmer and Norbert Felber, for the very pleasant atmosphere at the institute.

Special thanks go to all my friends supporting me during my PhD and to my family. In particular, I wish to thank Dorothea Lüdi for her encouragement to continue my study at ETH after my microtechnique engineering degree and Monica Benkler for giving me (additional) financial support during my ETH study.

In the end, my deepest thanks goes to my parents for all their support and care in every respect throughout all the years and to Edith, who makes my life bright.

Part I

Background and  
Motivation



# Chapter 1

## Introduction

### 1.1 Motivation and Objectives

From the large number of methods used to simulate electromagnetic (EM) fields, the Finite-Difference Time-Domain algorithm (FDTD) originally proposed by Yee back in 1966 [1] has gained the most interest both among researchers and for commercial simulation platforms. For high frequency applications, the FDTD method has proven to be a very flexible, efficient, robust, and versatile scheme for the full wave simulations of electromagnetic problems in the time domain. Especially within the sector of mobile telecommunication equipment, the usage of technical computer aided design (TCAD) has gained increased interest; the FDTD method has proven its efficient and reliable prediction of measurement results of virtual highly complex CAD based prototypes. Motivated by positive experience in the mobile telecommunication sector, the targeted applications are becoming electrically larger, involving smaller geometrically details, e.g., in the medical sector. Typical applications could include the simulation of pacemakers/leads in a human body placed with a magnetic resonance imaging (MRI) system. Similar dimensions could be targeted in the automotive industry regarding cabling and EMI issues. The introduction of 64 bit computers was a significant step towards allowing larger simulations. However, the staircasing approximation of curved

material interfaces due to the orthogonal grid can lead to significant inaccuracies in electromagnetic simulations. Furthermore, field singularities at sharp material edges have to be resolved in detail to achieve accurate results. Since the explicit time step is limited by the smallest spatial step, the smallest spatial step should be kept as coarse as possible. The subcell modeling technique can be used to introduce ‘intelligent’ computational cells, improving the local field with *a priori* known field behavior knowledge.

Another strategy to overcome the time step restriction is to switch to implicit time integration schemes. Whereas fully implicit solvers for Maxwell’s equations are computationally too expensive, the alternating direction implicit (ADI) technique has attracted the research community. The ADI-FDTD scheme can be efficiently implemented and is unconditionally stable. The subcell modeling technique in the framework of ADI-FDTD has not yet been addressed by the research community.

Since 2005, the conventional FDTD update equations have been incorporated onto NVIDIA graphics cards with onboard FGPA (field programmable gate array). With the hardware acceleration, the simulation time is thus reduced by a factor of at least ten compared to even highly optimized FDTD solvers fully implemented in software. Hence, optimization of complex models can now be targeted based on the drastically reduced simulation times. However, using the simulation platform in an optimization process implies a very robust gridding–discretizing–simulating–analyzing–optimizing procedure. Therefore, every substep has to be highly automated, tolerant, and efficient. Furthermore, in order to also use the hardware acceleration card for subcell model enhancements, the models need to be formulated within the conventional FDTD update equation framework, i.e., with modified material parameters.

The objectives of this thesis were the development and analysis of new generally applicable and robust FDTD subcell models and their integration into the continuously developed 3-D EM simulation platform SEMCAD X [2]. The investigations to achieve these demands consisted of the following parts:

- Detailed and topical literature research on existing subcell modeling techniques: conformal dielectric–dielectric and dielectric–

PEC material interfaces and quasistatic field singularity models.

- Development and implementation of a highly efficient and robust conformal discretization algorithm. The accurate conformal discretization is the basis of all subcell models.
- Development and validation of existing and new conformal PEC subcell models with a strong focus on applicability to real-world problems. Therefore, the novel model needs to provide a rigorous stability criterion.
- Investigations on conformal dielectric–dielectric subcell models based on existing and novel approaches of effective material properties.
- Review of field singularity subcell models and their reformulation within the conventional FDTD update equation.
- Benchmarking of the implicit time integration ADI-FDTD algorithm compared to the conventional FDTD method. The suitability of the ADI-FDTD technique on real-world simulations is investigated.
- Development of a subcell model technique within the framework of the ADI-FDTD method. A novel versatile general approach to incorporate conformal and/or field singularity models is derived.

## 1.2 Outline of Thesis

The remaining chapters of this thesis are outlined as follows:

*Chapter 2:* The mathematical formulation of Maxwell’s equations is introduced in differential and integral form. The numerical aspects of solving Maxwell’s problem are discussed with a short overview of different numerical schemes.

*Chapter 3* reviews the Finite-Difference Time-Domain method. In addition to from the advantageous properties of the FDTD scheme, its limitations are also investigated. Detailed topical literature on

the conformal subcell modeling of dielectric–dielectric and dielectric–PEC material interfaces as well as on edge field singularity models is presented. Important results and findings are reviewed and open issues are identified.

*Chapter 4:* A novel conformal discretization algorithm is described in detail. The efficient and robust algorithm is designed to cope with real-world CAD models with thousands of distinguished parts.

*Chapter 5* introduces the novel, robust and accurate conformal PEC model based on the conventional FDTD update equation. The derivation of the stability criterion enabled the new algorithm to achieve the best accuracy for a given time step.

*Chapter 6* and *Chapter 7* shortly summarize the theory and some results of the conformal dielectric and edge field singularity subcell models.

*Chapter 8:* The findings of the FDTD subcell models are adapted to the ADI-FDTD method. A new general concept is introduced to adapt existing or novel FDTD subcell models to the ADI-FDTD scheme with minor effort by modifying the conventional update coefficients.

*Chapter 9* revisits a joint study carried out with the Nokia Research Center within the framework of the ADI-FDTD solver. The efficiency and benefits of the ADI-FDTD algorithm are demonstrated on a real-world application, a complete mobile phone.

# Chapter 2

## Numerical Solution of Maxwell's Equations

### 2.1 Maxwell's Equations

In 1865, James Maxwell introduced a pioneering way of describing electromagnetic phenomena [3]. In differential form Maxwell's equations read

$$\nabla \times \vec{E}(\vec{x}, t) = - \frac{\partial \vec{B}(\vec{x}, t)}{\partial t}, \quad (2.1a)$$

$$\nabla \times \vec{H}(\vec{x}, t) = \frac{\partial \vec{D}(\vec{x}, t)}{\partial t} + \vec{J}_E(\vec{x}, t), \quad (2.1b)$$

$$\nabla \cdot \vec{D}(\vec{x}, t) = \rho(\vec{x}, t), \quad (2.1c)$$

$$\nabla \cdot \vec{B}(\vec{x}, t) = 0. \quad (2.1d)$$

The symbols can be found in appendix B. Equations (2.1c) and (2.1d) can be derived by calculating the divergence ( $\nabla \cdot$ ) of (2.1a) and (2.1b), using the charge continuity equation

$$\frac{\partial \rho(\vec{x}, t)}{\partial t} = -\vec{J}_E(\vec{x}, t), \quad (2.2)$$

and divergence free initial  $\vec{D}(\vec{x}, 0)$  and  $\vec{B}(\vec{x}, 0)$  fields. Integrating equations (2.1a) and (2.1b) on an arbitrary surface  $A$  and equations (2.1c) and (2.1d) on an arbitrary volume  $V$  yield Maxwell's equations in integral form:

$$\oint_{\partial A} \vec{E}(\vec{x}, t) \cdot d\vec{s} = - \frac{\partial}{\partial t} \iint_A \vec{B}(\vec{x}, t) \cdot d\vec{A}, \quad (2.3a)$$

$$\oint_{\partial A} \vec{H}(\vec{x}, t) \cdot d\vec{s} = \frac{\partial}{\partial t} \iint_A \vec{D}(\vec{x}, t) \cdot d\vec{A} + \iint_A \vec{J}_E(\vec{x}, t) \cdot d\vec{A}, \quad (2.3b)$$

$$\oiint_{\partial V} \vec{D}(\vec{x}, t) \cdot d\vec{A} = \iiint_V \rho(\vec{x}, t) dV = Q, \quad (2.3c)$$

$$\oiint_{\partial V} \vec{B}(\vec{x}, t) \cdot d\vec{A} = 0 \quad (2.3d)$$

where  $\partial X$  denotes the border of domain  $X$ . Both forms of Maxwell's equations (2.3) and (2.1) are not well defined, because there are too many degrees of freedom for the fields  $\vec{E}$ ,  $\vec{H}$ ,  $\vec{D}$ , and  $\vec{B}$ .

For linear, isotropic and non-dispersive materials, the following constitutive relations can be written

$$\vec{D}(\vec{x}, t) = \epsilon \vec{E}(\vec{x}, t), \quad (2.4a)$$

$$\vec{B}(\vec{x}, t) = \mu \vec{H}(\vec{x}, t), \quad (2.4b)$$

and with linear electric losses

$$\vec{J}_E(\vec{x}, t) = \sigma \vec{E}(\vec{x}, t). \quad (2.4c)$$

Important to note is that the fluxes  $\vec{D}$  and  $\vec{B}$  with units per surface  $\frac{\star}{m^2}$  are connected with equations (2.4) to the field strengths  $\vec{E}$  and  $\vec{H}$  with units per length  $\frac{\star}{m}$ . Therefore, even if the relations in (2.4) look simple, the relation is physically complex and not trivial (line versus surface). However, in a homogeneous region the constitutive relations describe the physics accurately.

## 2.2 Numerical Methods

Even though equations (2.1a) and (2.1b), together with the constitutive relations (2.4), form a set of linear hyperbolic equations, boundary and interface conditions make Maxwell's equation hard to solve

analytically. Only a limited range of idealized cases (e.g., sphere, infinite cylinder) can be analytically solved. Most real-world applications require the numerical solution of a discretized reformulation of the original problem. Numerous methods have been proposed based on Maxwell's differential form (2.1), on the integral form (2.3), the Poisson, or the Helmholtz equation. A few methods are shortly summarized with no claim to completeness, see also [4, 5, 6].

### 2.2.1 Finite Differences (FDTD)

Back in 1966, K. Yee [1] introduced an ingenious and second order accurate scheme for solving Maxwell's equations in differential form (2.1). Because this scheme is the main topic of this thesis, a detailed description of the algorithm can be found in chapter 3. In short, the electric  $\vec{E}$  and magnetic  $\vec{H}$  fields are used to represent the solution to the differential form of Maxwell's equations (2.1).

### 2.2.2 Finite Integration Technique (FIT)

Using the integral form of Maxwell's equation (2.3) on a rectilinear grid leads for equation (2.3a) to

$$\begin{aligned} \bar{e}_x(i, j, k) + \bar{e}_y(i + 1, j, k) - \bar{e}_x(i, j + 1, k) - \bar{e}_y(i, j, k) = \\ - \frac{d}{dt} \bar{b}_z(i, j, k) \end{aligned} \quad (2.5)$$

where  $\bar{e}_m$  is the path integral of  $\vec{E}$  along the edge  $m$  and  $\bar{b}_z$  is the face integral of  $\vec{B}$  with normal  $z$  [7]. Equation (2.5) is an exact representation of equation (2.3a), because the exact integrals are used. Introducing a dual grid (see [7]), equation (2.3b) is discretized in a similar way using  $\bar{h}$  and  $\bar{d}$ . To connect the two grids, the constitutive relations come in use and are the only approximation in the scheme.

The formulation is not restricted to an orthogonal grid. However, for non-orthogonal grids the constitutive relation matrices are no longer diagonal. Therefore, all fields  $\vec{E}$ ,  $\vec{D}$ ,  $\vec{H}$  and  $\vec{B}$  need to be stored. Further references on subgridding, conformal extensions, etc. can be found in [8] and the references therein.

However, applied on orthogonal rectilinear grids, the algorithm of FIT is formally equivalent to FDTD, if proper material parameters at interfaces are assigned in the FDTD method.

### 2.2.3 Transmission Line Method (TLM)

TLM is similar to the FDTD method in terms of its capabilities. As in the FDTD scheme, the analysis is performed in the time domain and the entire spatial domain is meshed. However, instead of interleaving  $E$  and  $H$  fields on the primary and secondary grids, a single grid is established and the nodes of the grid are interconnected by virtual transmission lines. Currents  $I$  and voltages  $V$  of the transmission lines are then updated each time step.

A theoretical field comparison can be found in [9], which reveals the advantages of FDTD (physical versus non-physical eigenmodes).

### 2.2.4 Finite-Element Time-Domain Method

The Finite-Element Time-Domain (FETD) method solves Maxwell's equations in a weak sense with a variational formulation [10, 11, 6]. In detail, in the lossless case, equation

$$\epsilon \frac{\partial^2}{\partial t^2} \vec{E} + \nabla \times \frac{1}{\mu} \nabla \times \vec{E} = \vec{0} \quad (2.6)$$

(eliminate  $\vec{H}$  in (2.1a) with (2.1b)) is solved in a weak sense: Find  $\vec{E} \in H(\text{curl}; \Omega)$  such that

$$\int_{\Omega} \left( \epsilon \frac{\partial^2}{\partial t^2} \vec{E} \cdot \vec{w} + \frac{1}{\mu} \nabla \times \vec{E} \cdot \nabla \times \vec{w} \right) d\Omega = \vec{0} \quad (2.7)$$

for all  $\vec{w} \in H(\text{curl}; \Omega)$ , where  $H(\text{curl}; \Omega) := \{ \vec{v} : \vec{v} \in (L^2(\Omega))^3, \nabla \times \vec{v} \in (L^2(\Omega))^3 \}$ ,  $L^2(\Omega) := \{ f : \int_{\Omega} f^2 d\Omega < \infty \}$ , and  $\Omega$  is the domain of interest.

On tetra- or hexahedral meshes, *edge* or *Whitney* elements [12] serve as the numerical subspace of  $H(\text{curl}; \Omega)$ . Finally, the discrete problem is a huge but sparse matrix equation representing an ordinary differential equation system in time. To obtain an explicit scheme on

a general unstructured grid is difficult [10]. Mass lumping is a popular approximation to produce diagonal mass matrices in FETD [13]. However, mass lumping often destroys positive definiteness, leading to unconditional instabilities [14].

Differential forms can be used as an alternative mathematical language to formalize Maxwell's equations [15]. Differential forms provide a very concise and mathematically elegant language to treat the classical EM theory on a lattice. They allow for the factorization of the field equations into a topological part and a metric part. The resulting topological equations are invariant under homeomorphisms, i.e., invariant for lattices with the same topological structure. All of the usual vector calculus operators are unified by a single operation, the exterior derivative, which admits a trivial and exact discretization on an arbitrary lattice through the use of its discrete adjoint, the boundary operator. Metric concepts need to be invoked only in connection with the Hodge operators [15], which also generalize the constitutive relations of the medium. In [16] the formal connection between this approach with the FIT method are shown and explained.

Even though the FETD method is applicable to unstructured meshes and accurately solves curved boundaries, the burden on the memory side for storing the matrix entries and on larger dispersion errors limits the use of FETD schemes on huge problems.

The equivalence of FDTD and FETD algorithm on orthogonal, hexahedral grids is shown, e.g., in [11]. A stable hybrid solver FDTD-FETD is proposed in the thesis of Andersson [10].

### 2.2.5 Finite-Volume Time-Domain Method

In the Finite-Volume Time-Domain (FVTD) method, Maxwell's curl equations are reformulated in conservation law form  $\partial u/\partial t + \nabla \cdot u = 0$  and then integrated over a volume [17, 18]. In the lossless case, the integral reads

$$-\frac{\partial}{\partial t} \iiint_V \vec{B} dV = \oint_{\partial V} \vec{n} \times \vec{E} dA, \quad (2.8a)$$

$$\frac{\partial}{\partial t} \iiint_V \vec{D} dV = \oint_{\partial V} \vec{n} \times \vec{H} dA, \quad (2.8b)$$

where  $V$  denotes an arbitrary volume [19]. The discretized equations in a polyhedral cell are then written

$$-\frac{\partial}{\partial t} \langle \vec{B} \rangle_V = \frac{1}{V} \sum_k F_k \cdot \vec{n}_k \times \langle \vec{E} \rangle_{F_k}, \quad (2.9a)$$

$$\frac{\partial}{\partial t} \langle \vec{D} \rangle_V = \frac{1}{V} \sum_k F_k \cdot \vec{n}_k \times \langle \vec{H} \rangle_{F_k}, \quad (2.9b)$$

where  $\langle \cdot \rangle$  denotes spatial mean values and the polyhedron with volume  $V$  is bounded by  $k$  faces with area  $F_k$ .

Approximations of (2.9) are necessary to enable their processing in a computer. A large variety of different FVTD schemes exist. The algorithm variations are basically distinguished by three characteristics: finite-volume discretization, flux approximation, and time-stepping scheme. Further information can be found in, e.g., [19].

## 2.2.6 Method of Moments (MoM)

Similar to finite element method, MoM is a technique for solving complex integral equations by reducing them to a system of simpler linear equations [20]. In contrast to the variational approach of the finite element scheme, MoM employs a technique known as the *method of weighted residuals*.

All weighted residual techniques begin by establishing a set of trial solution functions with one or more variable parameters. The residuals are a measure of the difference between the trial solution and the true solution. The variable parameters are determined in a manner that guarantees a best fit of the trial function based on a minimization technique.

While MoM is an approach with general usability in the time domain [21], the method is usually applied on the time harmonic equation ( $\partial/\partial t = -j\omega$ , in equation (2.1)). In this case, the equation solved by the MoM technique is generally a form of the *electric field integral equation* (EFIE) or the *magnetic field integral equation* (MFIE). For a PEC scatterer the equation reads for the MFIE

$$\vec{n}(\vec{s}) \times \vec{H}^{\text{inc}}(\vec{s}) = \frac{1}{2} \vec{J}(\vec{s}) - \vec{n}(\vec{s}) \times \iint_A \vec{J}(\vec{x}) \times \nabla \left( \frac{e^{-jk|\vec{s}-\vec{x}|}}{4\pi|\vec{s}-\vec{x}|} \right) dA(\vec{x}) \quad (2.10)$$

and for the EFIE

$$\begin{aligned}
 -j\omega\epsilon\vec{n}(\vec{s}) \times \vec{E}^{\text{inc}}(\vec{s}) = \vec{n}(\vec{s}) \times \left[ k^2 \iint_A \vec{J}(\vec{x}) \left( \frac{e^{-jk|\vec{s}-\vec{x}|}}{4\pi|\vec{s}-\vec{x}|} \right) dA(\vec{x}) + \right. \\
 \left. \nabla \iint_A \nabla \cdot \left( \vec{J}(\vec{x}) \left( \frac{e^{-jk|\vec{s}-\vec{x}|}}{4\pi|\vec{s}-\vec{x}|} \right) \right) dA(\vec{x}) \right]
 \end{aligned}
 \tag{2.11}$$

where  $\vec{E}^{\text{inc}}$  and  $\vec{H}^{\text{inc}}$  are the given incident electric and magnetic fields, respectively, and  $\vec{s}$  is a point on the surface  $A$  of the scatterer (equation (140) and (141) of [22]). The current density  $\vec{J}(\vec{s})$  on the scatterer's surface is the unknown variable. Replacing the current surface density  $\vec{J}(\vec{s})$  with a discrete current mesh yields a linear equation system for the unknown current strength.

Aside from the different context harmonic or time dependent, MoM has its strength in solving PEC structures efficiently, whereas highly complex dielectric models quickly exceed the capabilities of today's computers because of solving a full matrix system.

### 2.2.7 Generalized Multipole Technique (GMT)

GMT [23] is a frequency domain technique (like MoM) based on the method of weighted residuals. However, GMT is unique in that the expansion functions are analytical solutions of the fields generated by sources. The expansion functions are spherical wave field solutions corresponding to multipole sources. As with MoM, a system of linear equations is developed and then solved to determine the coefficients of the expansion functions that yield the best solution. GMT shares the advantages and limitations of MoM.



## Chapter 3

# Finite-Difference Time-Domain Method (FDTD)

In 1966, Kane S. Yee introduced his pioneering algorithm to numerically solve Maxwell's equations for initial boundary value problems in isotropic medias and in the time domain [1]. Yee's innovation was the proposition of a Cartesian staggered grid (see section 3.1.1), i.e.,  $\vec{E}$  and  $\vec{H}$  are separated by half a time step and each vector component is *not* spatially co-allocated with the others. In [24] and [25] the advantage of the chosen staggered grid is demonstrated and compared with other finite difference discretization possibilities.

Shlager and Schneider published detailed surveys about FDTD development [26, 27]. In addition, they maintain an online database [28], which is a good starting point to explore the heavily growing number of FDTD related publications. Taflove published comprehensive books about the FDTD method and related topics [29, 30, 6].

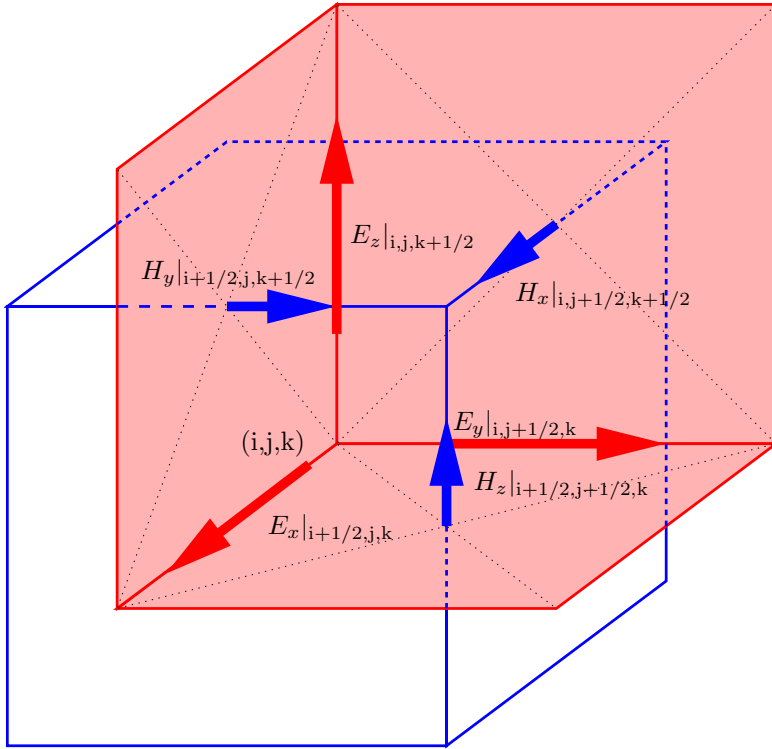


Figure 3.1: Spatially staggered Yee grid.

## 3.1 Essential Properties

### 3.1.1 Yee Grid

Yee's innovation was the spatially and temporally staggered grid [1, 6]. The spatially staggered grid is shown in Figure 3.1. Each electric component  $E_i$  is offset by half a grid step in the direction  $i$ , whereas the magnetic component  $H_i$  is offset by half a grid step in every direction but  $i$ . Another interpretation is a dual grid where the primary and secondary grids are red and blue, respectively. Thus, the electric field  $\vec{E}$  is defined on primary grid edges, whereas the magnetic field  $\vec{H}$  is

located on secondary grid edges.

The great advantage of Yee's grid is that all of the spatial derivatives can be expressed as centered differences leading to second order accuracy:

$$E_x|_{i+1/2,j,k}^{n+1} = \alpha_E|_{i+1/2,j,k} \cdot E_x|_{i+1/2,j,k}^n + \beta_E|_{i+1/2,j,k} \cdot \left( \frac{H_z|_{i+1/2,j+1/2,k}^{n+1/2} - H_z|_{i+1/2,j-1/2,k}^{n+1/2}}{\Delta y_j^s} - \frac{H_y|_{i+1/2,j,k+1/2}^{n+1/2} - H_y|_{i+1/2,j,k-1/2}^{n+1/2}}{\Delta z_k^s} \right) \quad (3.1a)$$

$$H_x|_{i,j+1/2,k+1/2}^{n+1/2} = \alpha_H|_{i,j+1/2,k+1/2} \cdot H_x|_{i,j+1/2,k+1/2}^{n-1/2} + \beta_H|_{i,j+1/2,k+1/2} \cdot \left( \frac{E_z|_{i,j,k+1/2}^n - E_z|_{i,j+1,k+1/2}^n}{\Delta y_j^p} - \frac{E_y|_{i,j+1/2,k}^n - E_y|_{i,j+1/2,k+1}^n}{\Delta z_k^p} \right) \quad (3.1b)$$

where  $\Delta i_j^p$  and  $\Delta i_j^s := (\Delta i_j^p + \Delta i_{j-1}^p)/2$  denote the local spatial step in direction  $i$  on the primary ( $p$ ) and secondary ( $s$ ) grids, respectively. In addition and as expressed with the time subscript  $n$ , the time is discretized with the so-called Leap-Frog scheme (centered differences, second order), leading to half a time step offset between  $\vec{E}$  and  $\vec{H}$ . The update coefficient functions are

$$\alpha_E := \exp\left(-\frac{\sigma \Delta t}{\epsilon}\right) \xrightarrow{\sigma \rightarrow 0} 1 \quad (3.2a)$$

$$\beta_E := \frac{1 - \alpha_E}{\sigma} \xrightarrow{\sigma \rightarrow 0} \frac{\Delta t}{\epsilon} \quad (3.2b)$$

$$\alpha_H := 1 \quad (3.2c)$$

$$\beta_H := -\frac{\Delta t}{\mu}. \quad (3.2d)$$

Keeping the continuous spatial derivation, Yee's equation (3.1) can

be rewritten in matrix form

$$\vec{E}^{n+1} = \alpha_E(\Delta t) \cdot \vec{E}^n + \beta_E(\Delta t) \cdot \tilde{\mathcal{R}} \vec{H}^{n+1/2} \quad (3.3a)$$

$$\vec{H}^{n+1/2} = \alpha_H(\Delta t) \cdot \vec{H}^{n-1/2} + \beta_H(\Delta t) \cdot \tilde{\mathcal{R}} \vec{E}^n \quad (3.3b)$$

where

$$\tilde{\mathcal{R}} := \begin{pmatrix} 0 & -\partial_z & \partial_y \\ \partial_z & 0 & -\partial_x \\ -\partial_y & \partial_x & 0 \end{pmatrix} \quad (3.4)$$

is the matrix representation of the curl operator  $\nabla \times$ . This formulation will be used later in section 3.4.

### 3.1.2 Divergence Free Nature

If nonlossy simulations are considered ( $\sigma = 0$ ,  $\rho = 0$ ), the divergence of  $\vec{D}$  (2.1c) and  $\vec{B}$  (2.1d) are vanishing. Using the equivalent integral form of Maxwell's equation (2.3c) and (2.3d) on the secondary grid, the FDTD method numerically preserves these results. This essential property of the FDTD algorithm is even fulfilled on nonuniform grids and inhomogeneous material distributions using the following discrete form of the divergence:

$$\begin{aligned} \oint_{\partial V} \vec{D} \cdot d\vec{A} \approx & \\ & (\epsilon|_{i+1/2,j,k} E_x|_{i+1/2,j,k} - \epsilon|_{i-1/2,j,k} E_x|_{i-1/2,j,k}) \Delta y_j^s \cdot \Delta z_k^s + \\ & (\epsilon|_{i,j+1/2,k} E_y|_{i,j+1/2,k} - \epsilon|_{i,j-1/2,k} E_y|_{i,j-1/2,k}) \Delta x_i^s \cdot \Delta z_k^s + \\ & (\epsilon|_{i,j,k+1/2} E_z|_{i,j,k+1/2} - \epsilon|_{i,j,k-1/2} E_z|_{i,j,k-1/2}) \Delta x_i^s \cdot \Delta y_j^s, \end{aligned} \quad (3.5)$$

because the spatially varying  $\epsilon|_{i+1/2,j,k}$  are compensated in the  $E$  update, e.g., the  $E_x$  update

$$\begin{aligned} E_x|_{i+1/2,j,k}^{n+1} = & E_x|_{i+1/2,j,k}^n + \frac{\Delta t}{\epsilon|_{i+1/2,j,k}} \cdot \\ & \left( \frac{H_z|_{i+1/2,j+1/2,k}^{n+1/2} - H_z|_{i+1/2,j-1/2,k}^{n+1/2}}{\Delta y_j^s} - \right. \\ & \left. \frac{H_y|_{i+1/2,j,k+1/2}^{n+1/2} - H_y|_{i+1/2,j,k-1/2}^{n+1/2}}{\Delta z_k^s} \right) \end{aligned} \quad (3.6)$$

and all  $H$  field components cancel out. Therefore, an initial (numerically) divergence-free electric flux ( $t = 0$ ) will vanish for  $t > 0$ .

On the other hand, if a modification to the FDTD algorithm can be formulated within the FDTD update equations, i.e., with modified permittivity and permeability, the divergence-free nature of the modified FDTD algorithm is inherited and fulfilled.

### 3.1.3 Stability — Explicit Time Step

The explicit leap frog time integration scheme is conditionally stable. Using a von Neumann frequency analysis on an infinite uniform grid [6], a stable time step can be derived

$$\Delta t < \sqrt{\frac{\epsilon\mu}{\frac{1}{\Delta x^2} + \frac{1}{\Delta y^2} + \frac{1}{\Delta z^2}}}, \quad (3.7)$$

where  $1/\sqrt{\epsilon\mu}$  is the speed of light  $c$  of the material. Therefore, the smallest computational cell determines the largest time step.

Denecker [31] rigorously proved a largest maximal time step for inhomogeneous material distributions in a metal box. For practical grid sizes, the predicted stable time step in [31] is only slightly larger than the one predicted with equation (3.7). At the limit of an infinitely large number of grid lines the two predicted time steps are equal. In general, the time step formula (3.7) is commonly used for nonuniform grids and inhomogeneous material distributions.

## 3.2 Limitations of the FDTD Method

Even though FDTD solvers are efficient and powerful in a wide range of complex engineering applications, the FDTD method has several drawbacks. The smallest computational cell defines the largest stable time step and, therefore, the overall simulation time due to the explicit time stepping scheme. Thus, the chosen computational grid is always a trade off between a short simulation time and the accurate resolution of geometrical details. This resolution has a strong impact on the field distribution. On one hand, the staircasing approximation of curved objects (Lego bricks) can lead to inaccuracies in EM simulations [32]

and [33]. On the other hand, field singularities near sharp material discontinuities needs to be resolved with small spatial steps due to the piecewise linear approximation of the singularity.

Another limitation of FDTD's accuracy is dispersion [34]. With the anisotropic dispersion error, the FDTD method is not designed for electrically large simulation regions. However, Christ [25] introduced a phase velocity corrected FDTD scheme. The dispersion error will not be further investigated in this thesis.

This thesis addresses the limiting factor of the largest stable time step which is determined by the smallest spatial step (3.7). Subcell modeling techniques can be used to overcome the staircasing errors and the strong field singularity gradients. The major objective is to calculate accurate results on a coarse grid and to circumvent a fine mesh, as in the conventional FDTD technique. In addition, unconditionally stable time integration schemes can be used to increase the time step above the limit calculated by equation (3.7).

### 3.3 Subcell Modeling

Subcell modeling adds local ‘cell-intelligence’ to the update equation to take into account local staircasing or strong field gradient effects. Therefore, the mesh size can be reduced while the accuracy is maintained. The following sections provide a survey of conformal dielectric, conformal PEC and edge field singularity subcell models [6].

#### 3.3.1 Conformal Dielectric Models

One strategy to reduce the staircasing errors is to use non-orthogonal grids or curvilinear coordinates instead of orthogonal Yee meshes [35, 36, 37, 38]. The conformal grids follow the exact shape of the objects in the simulation. Even though these methods improve the accuracy, such approaches not only considerably increase the complexity of the algorithm, but they can also cause numerical artifacts due to a highly irregular grid, like time instability, velocity dispersion and spurious wave reflection [39]. A preferable option is to exploit an orthogonal mesh as much as possible and to introduce distorted cells only where necessary, i.e., in the vicinity of material disconti-

nities. For those special cells, a contour-path FDTD (CP-FDTD) algorithm can be obtained directly from Maxwell's equations in integral form (2.3) [40, 41]. The CP-FDTD method can still contain cells that potentially generate late time instability [39] because of non-reciprocal nearest neighbor borrowing [39]. In addition, the conventional FDTD update equations are altered, resulting in slightly increased memory consumption and simulation time as compared to Yee's scheme. In [39, 42, 38], improvements to CP-FDTD methods are proposed to solve the instability issue. Another approach for reducing the staircasing error is to refine the grid in the vicinity of the material interfaces, the so-called subgridding technique, e.g., [43]. However, subgridding algorithms introduce modifications in the time updating procedure. Therefore, the technique is more complicated to implement, in addition to other numerical issues like spurious wave reflection and stability. For an overview see the thesis of Chavannes [43] and the references therein. The latest achievements with digital filtering can be found in [44, 45].

A different technique, specifically for dielectric interfaces, is to use effective permittivities for partially filled computational cells. The orthogonal grid remains undistorted and, therefore, the efficiency of the original FDTD method is maintained. The challenge is to choose the permittivity with the best approximation of the dielectric discontinuity. An early attempt in this direction has been made for modeling thin material sheets [46]. The procedure is limited to rectangular objects aligned with the grid and auxiliary terms for field components normal to the interface have to be used. In 1997, Kaneda *et al.* [47] introduced a phenomenological formula for the calculation of the effective permittivity for arbitrarily curved dielectric interfaces based on the orientation of the considered electric edge and arithmetic/harmonic volume weighted average. Kaneda's formula matches the rigorous derivations of [48, 49] who investigated the case of electric edges parallel and perpendicular to the material interfaces.

These effective permittivities improve the accuracy of the FDTD method, while preserving the stability and simple structure of the original algorithm. However, there is no guarantee that the formula fulfills the proper boundary conditions at a curved interface or simply at a flat interface tilted with respect to the mesh axes. There are several publications presenting other kinds of effective permit-

tivities: a volume average [50], a first-neighbor average of staircase cells [51], and other phenomenological derivations [52]. These proposals are not fundamentally more accurate than Kanedas approach. The main problem with the formulation of effective permittivities resides in the vectorial nature of the electromagnetic field. In fact, the same discontinuity can lead to quite different effective permittivity values depending on the orientation of the electric field with respect to the interface [48, 49]. Therefore, it is crucial that in the derivation of the effective permittivities, not only the geometry, but also the proper boundary conditions are taken into account. Along this line a non-diagonal effective-permittivity-tensor can be obtained via the homogenization of a partially filled cell [53, 54]. However, its implementation requires the usage of both  $\vec{E}$  and  $\vec{D}$ , implying more storage and CPU time. Moreover, because the field components are not defined in the same position in the FDTD method, a nearest-neighbor average is required for linking  $\vec{E}$  with  $\vec{D}$ . Such an average can blur the fulfillment of the boundary conditions at the interface.

Recently, there have been other original ideas that improve the accuracy of the FDTD method under rigorous treatment of the electromagnetic field at the dielectric interface, even though these ideas increase the complexity of the algorithm above the derivation of effective permittivities [55, 56, 57, 58, 59].

In 2005, Mohammadi *et al.* [60] presented a 2-D model using the normal of the interface. They compared the volume averaged effective permittivity method [50] with their exact contour path averaging and a volume averaged with normal weighted approximation. Their approximation (volume average with normal weight) results in the same accuracy level as their exact contour path model, whereas [50] is less accurate.

This thesis investigates different averaging schemes and proposes a 3-D variety of [60]. The findings can be found in chapter 6.

### 3.3.2 Conformal PEC Models

An excellent overview of PEC conformal subcell models can be found in Railton's publication [61] in 1999. Without going into the complexity of generalized nonorthogonal coordinates or a totally unstructured grid, the FDTD method was rewritten in terms of the integral form of

Maxwell's equation (2.3) instead of the differential form (2.1). While integrating Maxwell's equation, the curved PEC boundaries are taken into account, leading to the CP-FDTD method. This algorithm was applied to various scattering problems such as a radar cross section (RCS) calculation for double spheres [41]. Even though the benefit in accuracy of the CP-FDTD algorithm is clearly shown in various scattering benchmarks (e.g. [41]), due to the noncausal and nonreciprocal nearest neighbor approximation which is invoked, the technique is likely to exhibit late time instability regardless of how small a time step is used [37, 62]. Based on the knowledge of [62], a stabilized CP-FDTD was published [39]. In parallel, an automatic approach for generating the enlarged cells used in the CP-FDTD method was presented in [63]. Both methods [39, 63] are stable for a finite time step because of the maintained reciprocity. However, generation of the enlarged cells is complex.

In 1997, Dey *et al.* [64] proposed an FDTD algorithm based on contracted instead of enlarged cells. Even though the method [64] is much simpler to implement, and it maintains reciprocity, the algorithm suffers from late time instabilities [65]. The remedy of the same research group was the introduction of a method [65] in which the reduction of the PEC-free surface in the  $H$  update is ignored and only the shorting of the  $E$  field are applied. As pointed out by [66], the convergence rate of the method [65] is only first order, whereas the original scheme [64] was second order.

In the context of the finite integration technique (FIT) Zagorodnov *et al.* [67] published two conformal PEC schemes. In 2004, Xiao *et al.* [66] introduced a so-called enlarged cell technique (ECT) to overcome the staircasing limitation. Similar to [67], ECT uses a more complex magnetic flux calculation during the time update. On the other hand, according to the authors [67] and [66], their methods are stable with the conventional FDTD time step. A theoretical derivation of this claim is missing as it was only confirmed with numerical experiments.

The lack of a derived stability criterion and the drawback of the altered standard FDTD update scheme is addressed in this thesis. A rigorous analysis and details regarding the newly developed algorithm are presented in chapter 5.

### 3.3.3 Field Singularity Models

Large errors arise in regions where the fields rapidly change within a computational cell, as is the case in regions next to field singularities. Such singularities occur at sharp corners of material discontinuities dielectric/PEC or dielectric/dielectric [68]. As always, a finer discretization of these regions improves the accuracy. However, simultaneously the number of computational cells is increased as well as the largest time step is decreased. A more efficient way is to use correction factors in the FDTD update equations for cells adjacent to corners and edges of field singularities. The calculation of the correction factors is based on the *a priori* knowledge of the local field behavior, and it is performed during the setup of the simulation.

Back in 1981, Mur [69] introduced a first model to take into account edge field singularity. Shorthouse *et al.* [70] used five correction factors per update equation. Adaptation of the method to curved boundaries can be found in [71]. Esselle *et al.* [72] applied the idea to treat sharp metal edge field singularities lying 2-D diagonal in the computational domain. Foroughipour *et al.* [73] extended the same idea to 3-D diagonal microstrips. A hybrid between edge singularity and conformal PEC model was used in [74] to analyze a bow tie antenna.

In December 2005, Railton *et al.* [75] published a generalization of the correction factor calculation based on a correction with modified material parameters. In May 2006, Zscheile *et al.* [76] introduced a novel strategy to deduce the singularity exponent  $\nu$ . The method is based on a numerically calculated static field solution of the vicinity of the material discontinuity.

This thesis investigated the possibility of rewriting the field singularity models with the conventional FDTD update equation but modified  $\alpha_E$ ,  $\alpha_H$ ,  $\beta_E$ , and  $\beta_H$ . The details are found in chapter 7.

## 3.4 Unconditionally Stable Methods

As pointed out in section 3.2, the FDTD method becomes highly inefficient when geometrical details of the simulated model require a spatial resolution of a tiny fraction of the wavelength. The use of

unconditionally stable time integration schemes solves the time step limitation. However, using unconditionally stable methods for the time integration requires the solution of a (sparse) linear equation system in each time step. Therefore, the crucial point of all unconditionally stable time domain schemes is an efficient linear equation system solver.

### 3.4.1 Crank-Nicolson Scheme

The first choice for a unconditionally, non dissipative time integration method is the Crank-Nicolson scheme:

$$\frac{\partial \vec{x}}{\partial t} = f(\vec{x}, t) \quad (3.8)$$

$$\frac{\vec{x}(t + \Delta t) - \vec{x}(t)}{\Delta t} \approx \frac{f(\vec{x}, t + \Delta t) + f(\vec{x}, t)}{2}.$$

Applying the second order Crank-Nicolson scheme (3.8) to Maxwell's equations leads to

$$\vec{E}^{n+1} = \alpha_E(\Delta t) \cdot \vec{E}^n + \beta_E(\Delta t) \cdot \tilde{\mathcal{R}} \frac{\vec{H}^{n+1} + \vec{H}^n}{2}, \quad (3.9a)$$

$$\vec{H}^{n+1} = \alpha_H(\Delta t) \cdot \vec{H}^n + \beta_H(\Delta t) \cdot \tilde{\mathcal{R}} \frac{\vec{E}^{n+1} + \vec{E}^n}{2}, \quad (3.9b)$$

referred to below as CN-FDTD. In space, the same staggered grid as in the Yee scheme is used to approximate the curl operator. Substituting equation (3.9b) into (3.9a) leads to a sparse block diagonal matrix for  $\vec{E}^{n+1}$  with twelve off-diagonal matrix entries per row. The resulting matrix equation has to be numerically solved by direct or iterative solvers. Thereafter,  $\vec{H}^{n+1}$  is calculated explicitly with equation (3.9b). As intended, the numerical algorithm is unconditionally stable.

However, for tenth of millions of unknowns, even iterative solvers are too inefficient for typical simulation scenarios when the CN-FDTD method is used. Therefore, the CN-FDTD scheme is considered as numerically too expensive.

### 3.4.2 Alternating Direction Implicit FDTD Algorithm (ADI-FDTD)

In 1999, Namiki [77] published a pioneering article using the alternating direction implicit (ADI) technique for electromagnetic computations. Splitting the curl operator  $\tilde{\mathcal{R}}$  into its odd and even parts

$$\tilde{\mathcal{R}}_e := \begin{pmatrix} 0 & 0 & \partial_y \\ \partial_z & 0 & 0 \\ 0 & \partial_x & 0 \end{pmatrix}, \quad \tilde{\mathcal{R}}_o := \begin{pmatrix} 0 & -\partial_z & 0 \\ 0 & 0 & -\partial_x \\ -\partial_y & 0 & 0 \end{pmatrix} \quad (3.10)$$

the Crank-Nicolson equations (3.9) can be reformulated with the two subiterations (3.11) and (3.12). The two subiterations read

$$\vec{E}^{\text{tmp}} = \alpha_E(\Delta t/2) \cdot \vec{E}^n + \beta_E(\Delta t/2) \cdot \left( \tilde{\mathcal{R}}_e \vec{H}^{\text{tmp}} + \tilde{\mathcal{R}}_o \vec{H}^n \right) \quad (3.11a)$$

$$\vec{H}^{\text{tmp}} = \alpha_H(\Delta t/2) \cdot \vec{H}^n + \beta_H(\Delta t/2) \cdot \left( \tilde{\mathcal{R}}_e \vec{E}^{\text{tmp}} + \tilde{\mathcal{R}}_o \vec{E}^n \right) \quad (3.11b)$$

and

$$\begin{aligned} \vec{E}^{n+1} = & \alpha_E(\Delta t/2) \cdot \vec{E}^{\text{tmp}} + \\ & \beta_E(\Delta t/2) \cdot \left( \tilde{\mathcal{R}}_e \vec{H}^{\text{tmp}} + \tilde{\mathcal{R}}_o \vec{H}^{n+1} \right) \end{aligned} \quad (3.12a)$$

$$\begin{aligned} \vec{H}^{n+1} = & \alpha_H(\Delta t/2) \cdot \vec{H}^{\text{tmp}} + \\ & \beta_H(\Delta t/2) \cdot \left( \tilde{\mathcal{R}}_e \vec{E}^{\text{tmp}} + \tilde{\mathcal{R}}_o \vec{E}^{n+1} \right) \end{aligned} \quad (3.12b)$$

where  $\vec{E}^{\text{tmp}}$  and  $\vec{H}^{\text{tmp}}$  denote intermediate but non-physical fields. Note that in subiteration (3.11), the even part of  $\tilde{\mathcal{R}}$  is implicitly calculated and the odd part is explicitly treated, whereas in the second subiteration (3.12) it is vice versa. Following the procedure of the Crank-Nicolson scheme, the implicit  $H$  fields are substituted into the corresponding  $\vec{E}$  equation, leading to three tridiagonal linear equation systems for  $\vec{E}$  per subiteration. The great advantage of this algorithm is that computationally efficient solvers for the tridiagonal equation system exist, e.g., [78].

The extension to three dimensions was published by Namiki [79] and Zheng *et al.* [80] in 2000. The 3-D ADI-FDTD scheme is unconditionally stable and of second order, because the method is a

second order perturbation of the CN-FDTD scheme. However and as pointed out by Garcia *et al.* [81], the dispersion equation of the ADI-FDTD method reveals an additional term compared to the CN-FDTD method. This additional dispersion term scales like  $\Delta t^2$ , which becomes dominant for large time steps. Therefore and even though the method is unconditionally stable, predicting an appropriate time step for the targeted accuracy is a difficult task. Nevertheless and if properly used, the ADI-FDTD technique can save computer resources (memory, CPU) for highly overdiscretized simulations [82].

Further references to the ADI-FDTD method can be found in [83, 84, 85] (sources), [86, 87, 88] (perfectly matched layer absorbing boundary conditions). Different approaches of splitting the CN-FDTD curl operator can be found in [89] and the references therein. Essentially, they have all the same source of dispersion error.

### 3.4.3 Subcell Enhanced ADI-FDTD Scheme

The explicit FDTD method and the implicit CN-FDTD and ADI-FDTD schemes are very similar. They differ only in the approximation of the time integration. The spatial discretization is the same and can be expressed with the same update coefficient functions  $\alpha_E$ ,  $\alpha_H$ ,  $\beta_E$ , and  $\beta_H$ . Therefore, the ideas of section 3.3 can be adapted to the ADI-FDTD method, if the subcell models are properly formulated with these update coefficient functions. The adaptation leads to a novel, pioneering, and versatile approach for subcell modeling in the ADI-FDTD technique.

Very recently (May 2006), Chai *et al.* [90] published a conformal PEC ADI-FDTD scheme adapting Dey's FDTD algorithm [64] to ADI-FDTD. Because Dey's algorithm does not fit into the conventional FDTD update equations, Chai was also forced to modify the time updating routine of the ADI-FDTD scheme.

This thesis investigates the possibility of incorporating the subcell modeling technique into standard ADI-FDTD codes with minor efforts. The resulting new pioneering technique is described in detail in chapter 8.



**Part II**

**Methods**



# Chapter 4

# Conformal Discretization Algorithm

## 4.1 Abstract

A robust and automatic discretization algorithm for complex conformal finite-difference time-domain (C-FDTD) simulation is presented in this chapter. The targeted application range is to enable C-FDTD simulations for real world engineering problems. Based on computer-graphic methods, complex CAD models with thousands of distinct parts can be efficiently and robustly discretized. A versatile concept is introduced to avoid numerical inaccuracies while calculating intersections and to lead to a symmetric discretization without the overhead of ‘virtual lines’. In addition, a necessary three-dimensional consistency check/correction, as well as merging of conformal cells of different CAD parts are explained.

The robustness and performance of the presented discretization algorithm is demonstrated with CAD models of increasing complexity towards real world benchmarks. A conformal FDTD simulation with 80 million computation cells and 229 distinguished parts representing

a complete mobile phone and a head with hand demonstrates the capabilities of the versatile technique.

## 4.2 Introduction

The basis of all C-FDTD schemes is knowledge of the geometrical details of the model. Therefore, the conformal discretization algorithm needs to collect the intersection points along an FDTD-edge with the surface of an object. In 2002, Srisukh *et al.* [91] published an efficient discretization method for staircasing meshes based on CAD models and computer-graphic methods. In 2004, Su *et al.* [92] presented their latest work to conformally discretize CAD based models. Their approach is to extract a polyline representing a grid plane cutting the CAD model. The polylines are then conformally discretized. Also in 2004, Waldschmidt *et al.* [93] published their conformal discretization algorithm based on a CAD facet mesh. The shown canonical sphere and cylinder cavity benchmarks compare C-FDTD simulation with (1) CAD based discretization [93] and (2) a discretization based on analytical functions [61]. However, the presented CAD models are trivial.

Targeting industrial simulation problems, the main focus of this chapter is on an efficient and robust discretization algorithm for thousands of different parts in the CAD model on huge grids with hundreds of millions of computational cells. Dealing with large highly nonuniform grids on complex CAD models with many distinguished parts reveals substantial challenges. In the following the challenges are shortly summarized.

1. *Modeling*: To model thousands of distinct parts is very time consuming. Moreover, if the data could have been provided in standard CAD formats the remodeling is very cumbersome and errorprone. Therefore, robust CAD importers are necessary to process the huge amount of data.
2. *Non-Uniform Grid Lines*: Automatically producing an acceptable nonuniform rectilinear but orthogonal grid for thousands of parts is not trivial. In addition, certain constraints like grading ratios (neighboring grid steps can only vary in a predefined

range) and a certain number of grid lines per wavelength are required to guarantee accurate FDTD simulations.

3. *Efficient Model Discretization*: Determining the material properties (permittivity, conductivity, etc.) to each computational cell can lead to a computationally intensive task especially while calculating conformal information.
4. *Discretization of Aligned Objects*: Although C-FDTD simulations are basically designed for non-aligned object surfaces, grid lines touching an object's face are common. Therefore, the interface may cut the crossing node of three grid lines (Figure 4.1). However, numerical calculations will result in slightly different floating point numbers of the intersection point with the surface. This may lead to inconsistencies in cases such as depicted in Figure 4.1, which have to be resolved automatically.
5. *Discretization of Special Cases*: Symmetry is the targeted issue of this item. Figure 4.2 shows a grid line touching the faces between point  $P_1$  and  $P_2$  and between  $P_4$  and  $P_5$ . With floating point operations described in item 4, the theoretical intersection points  $P_1$ ,  $P_2$ ,  $P_4$ , and  $P_5$  may or may not be calculated numerically. Without further investigations this may lead to asymmetries and/or inconsistencies.

Furthermore, the case between points  $P_4$  and  $P_5$  is called in this thesis 'step', whereas, the case between points  $P_1$  and  $P_2$  is referred to as 'box'. These two situations 'step' and 'box' have to be distinguished, such that no computational overhead is introduced (in contrast to the concept of 'virtual lines' [92]) and without breaking the object's symmetry.

6. *Conformal Merging of Different CAD Parts*: Two touching objects theoretically share the interface. With the CAD representation, this is not always guaranteed. Therefore, merging the conformal information of several CAD parts needs to be considered and automatically solved.
7. *Robust C-FDTD Method*: After gathering the conformal information, the electromagnetic solver has to conformally enhance

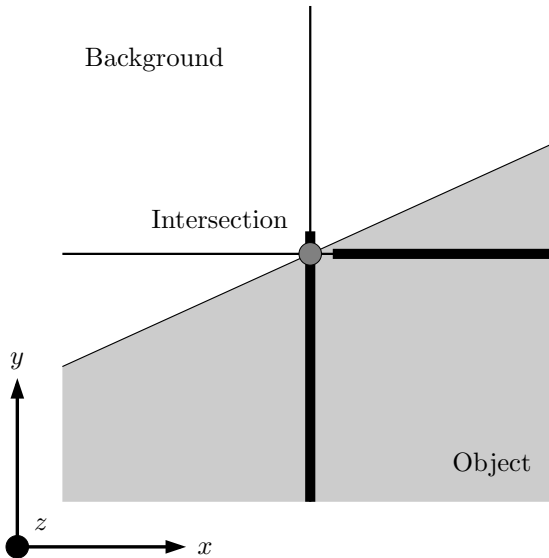


Figure 4.1: The grid line along  $z$  passes directly along the surface of the 3D object and passes through the gray point. The orthogonal grid line along  $x$  and  $y$  theoretically intersects the surface in the gray point. In numerical calculations, the calculated intersections are shifted (marked with the end of the bold lines). An inconsistency is produced because for the grid line along  $y$ , the gray point lies inside and for the grid line along  $x$ , the point lies outside.

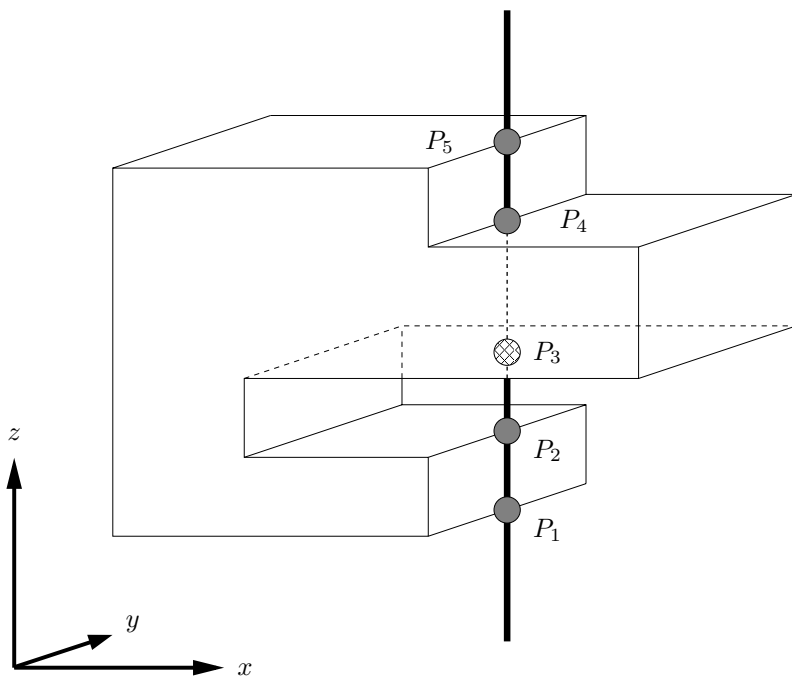


Figure 4.2: The gray dots denote the theoretical intersection points of the grid line along  $z$  and the object. The situation between  $P_4$  and  $P_5$  defined in this chapter as ‘step’, needs to be distinguished from the case between  $P_1$  and  $P_2$  denoted by ‘box’. The algorithm should be able to symmetrically discretize these situations.

the updating scheme. The applied FDTD method has to be robust for any complex material distribution, and the computational overhead and complexity of the algorithm should be kept to a minimum. If the conventional updating scheme is recovered, the adaption of the conformal method to hardware accelerated FDTD solvers (e.g., [94]) and/or to parallelized FDTD codes is straightforward.

To overcome these challenges is essential for simulating complex engineering problems. If optimization is targeted as well, the robustness of the method becomes crucial. The next section explains the details of the presented approach.

## 4.3 Method

### 4.3.1 Modeling and CAD Import

Most CAD software packages can export the description of their objects in terms of an oriented<sup>1</sup> facet mesh. Each facet mesh can be transformed into an oriented regular surface triangle mesh, which is the starting point of the presented conformal mesher. The simulation platform [2] uses the third party toolkit ACIS® [95] for modeling. In addition to the powerful modeling features, the simulation platform is capable of importing different CAD data formats (SAT, IGES, STEP, CATIA, 3DS, STL, etc.) and to transform them into a surface triangle mesh.

Based on this oriented surface triangle mesh, grid lines and the material property assignment to edges/cells can be implemented. The following sections describe details of the algorithm.

### 4.3.2 Generation of Grid Lines

The target is to generate nonuniform grid lines representing an orthogonal rectilinear computational grid. The nonuniform grid lines depend on each object in the simulation domain. The object's bounding box<sup>2</sup> defines fixed grid lines for the grid generation. If required

---

<sup>1</sup>The normal of the facet always points away from the object.

<sup>2</sup>The smallest cuboid parallel to the grid containing the object.

(e.g., for metal objects), the location of sharp edges define additional grid lines. Electromagnetic properties are used to determine the maximal grid step ( $< \lambda/10$  or similar, where  $\lambda$  is the wavelength). Defining a maximal grading ratio ensures a controlled reflection in a graded region. Starting with a geometric series, the grid is optimized towards a minimum number of grid lines, while maintaining the grading ratios and a minimal number of grid cells per wavelength.

### 4.3.3 Discretization of Objects

Given the three nonuniform axes of section 4.3.2, the computational edges and cells (voxels) need to have their material properties assigned. Furthermore, the conformal geometric information needs to be gathered near the object's interfaces.

The presented algorithm discretizes each object of the model with its surface triangle mesh sequentially. Therefore, a natural priority for overlapping objects is given by the discretization order (next object overwrites overlapping regions of previous objects). The conformal information between two touching objects is automatically merged (section 4.3.8).

The following sections describe the algorithm to discretize one object.

### 4.3.4 Computer-Graphic Methods

Each object is discretized using ideas from computer graphics (ray tracing, scan conversion) as introduced by Srisukh *et al.* [91]. The basic principle is to reduce the complexity of the algorithm from the order of three to two dimensions. Instead of testing each computational cell within the bounding box of the object (three-dimensional), the intersection of the grid line with the object's surface (two-dimensional) is used to determine the material properties. Figure 4.3 depicts the projection of a three-dimensional object onto the  $xz$ -plane (dark part). With the help of the exact intersection points, three regions can be defined: (1) the dark regions (between exit and entry point), which are completely inside, (2) the white regions, which are completely outside the object, and (3) the light gray regions (single FDTD-edges), which are cut at some point. The big advantage is that without any further

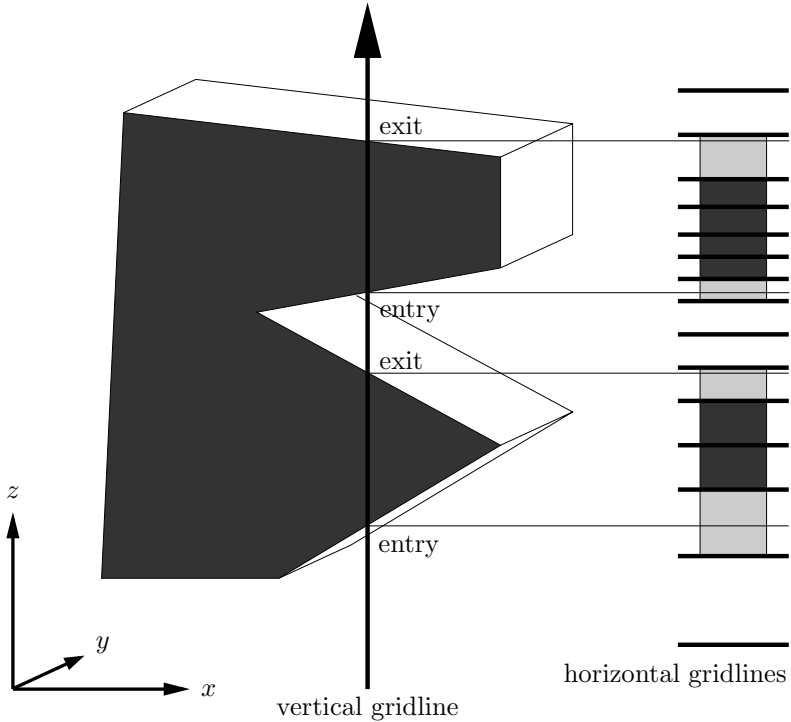


Figure 4.3: Scan conversion algorithm: the intersection points define segments on the grid line along  $z$  (light gray regions depicted to the right). Independent of how many segments (edges) are between an entry and an exit point, these edges can be efficiently assigned to the considered object.

computation the dark part can be assigned to the dark material independent of how many cells are between an entry and an exit point. Furthermore, computationally intensive tasks (three-dimensional consistency checks, writing conformal information to disc, etc.) are performed only on the light gray region. This procedure greatly reduces the discretization time.

### 4.3.5 Calculation of the Intersection

The conventional attempt in computer-graphic methods is to find every intersection point with objects along a single grid line. In principle, each triangle of the surface mesh of an object needs to be tested for a possible intersection. This is highly inefficient for the purpose of the discretization, even though tree-based methods and fast pretests can reduce the complexity.

In contrast, the presented approach reverses the algorithm: instead of finding all surface triangles intersecting a given grid line, all grid lines are searched which intersect a given surface triangle. With the help of the bounding box of a triangle the latter search is very efficient due to the rectilinear nature of the grid.

The direction of the grid line defines the projection of the three-dimensional surface triangle. This projected triangle needs to be intersected with the given grid line. Before calculating the intersection point, a preliminary check has to be passed to ensure that the three vertex points of the projected triangle do not lie on one line, i.e., the triangle is not badly shaped.

#### Badly Shaped Triangles

In Figure 4.4 two typical badly shaped triangles are depicted. Triangle (a) is characterized by a small edge length. The triangle is considered as badly shaped if its smallest edge length is below a certain tolerance. In the current implementation  $10^{-5} \cdot \Delta_{\min}$  is used as tolerance where  $\Delta_{\min}$  denotes the smallest spatial step in the computational domain. Triangle (b) is characterized by a small triangle height and is considered as badly shaped if its smallest height is below a tolerance (current implementation  $10^{-5} \cdot \Delta_{\min}$ ). Triangle (a) is a special case

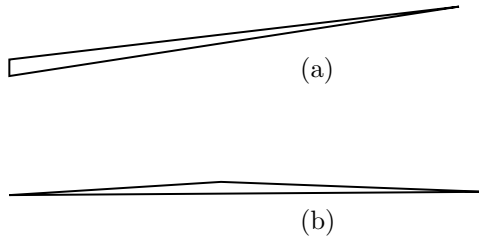


Figure 4.4: Badly shaped triangles can cause numerical inaccuracies while calculating intersections. Therefore, triangles with edge lengths smaller than a tolerance (a) are skipped. Case (b): the smallest height of the triangle is smaller than a tolerance. Aside from badly shaped surface triangles, the projection of them on, e.g., the  $xy$  plane can result in very elongated triangles.

of (b). However, its computation is more efficient and therefore, the badly-shaped-triangle test can be accelerated.

If this test is passed, i.e., the triangle is not badly shaped, the triangle forms a regular triangle and no numerical problems are expected during the calculation of the intersection.

### Tolerances for Triangles

The discretization challenges described in items 4 and 5 of the introduction are mainly due to errors in floating point operations and shape inaccuracies introduced by the representation with a surface triangle mesh. As a solution, introducing a tolerance strip around the triangle (current implementation  $10^{-3} \cdot \Delta_{\min}$ ) depicted in Figure 4.5 has several advantages:

- The grid line always hits the surface triangles describing the object in Figure 4.2 on points  $P_1$ ,  $P_2$ ,  $P_4$ , and  $P_5$ .
- With badly shaped triangles (Figure 4.4), floating point arithmetic can lead to increased inaccuracies. Therefore, possible numerical gaps between adjacent surface triangles are filled.
- Representation inaccuracies, i.e., curved surfaces approximated with surface triangles, are smoothed. In Figure 4.6, a very coarse

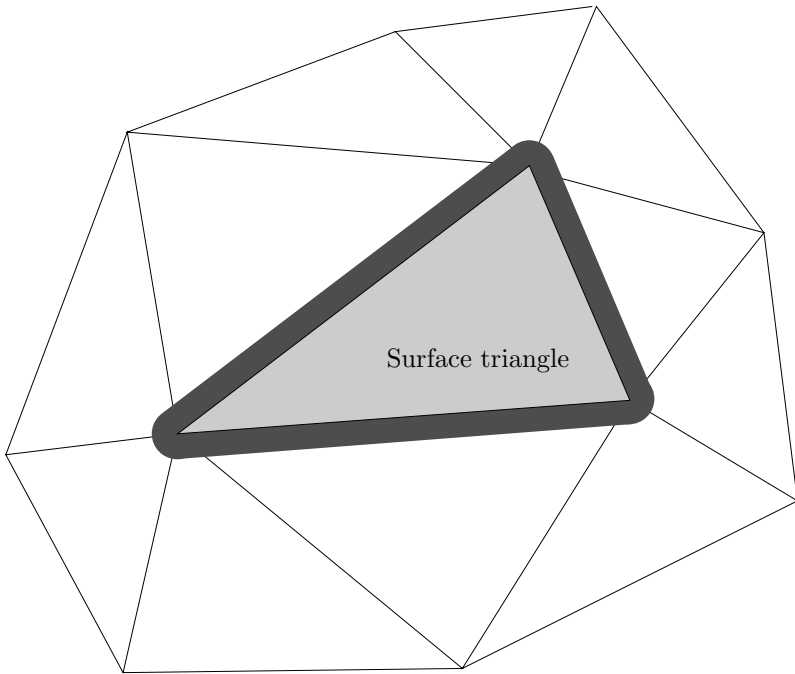


Figure 4.5: Surface triangle mesh: a single surface triangle (light gray) is shown with its tolerance strip (dark gray). The tolerance strip ensures that no numerical gap is between the surface triangles due to floating point operations.

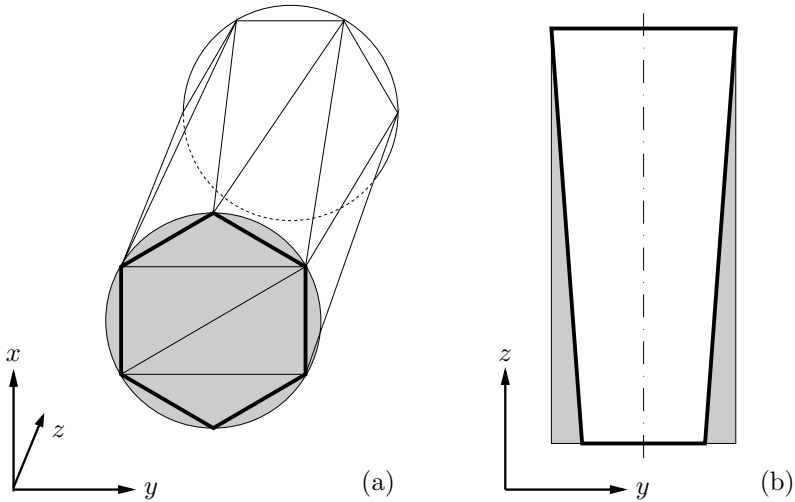


Figure 4.6: In (a), a very coarse surface triangle mesh of a cylinder is shown. Because the surface triangle representation of the top and bottom face are rotated by  $90^\circ$ , the  $y$  width on the front face represented by the triangles is smaller than on the back face. The projection on the  $yz$  plane is depicted in (b). The representation inaccuracy is highlighted in gray. With a tolerance strip, this discrepancy can be smoothed.

mesh of a cylinder is sketched. Along the  $y$  axis, the front face appears to have a smaller diameter than the back face due to the different vertex points (rotated by  $90^\circ$ ).

The next section shows how the tolerance can be easily incorporated into the algorithm.

### Calculation of Intersection Coordinates

The proposed method is based on barycentric coordinates  $s_i$  sketched in Figure 4.7

$$P_{\text{test}} = s_1 P_1 + s_2 P_2 + s_3 P_3 \quad (4.1)$$

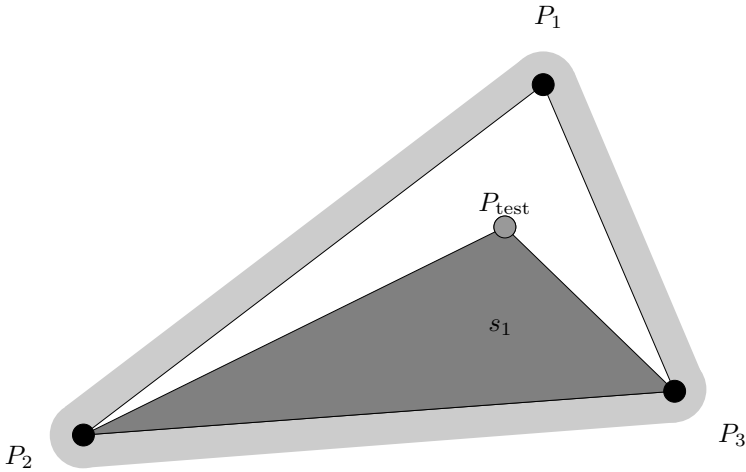


Figure 4.7: Barycentric coordinates:  $s_1$  is defined as the area ratio between the gray triangle and the total triangle ( $P_1$ ,  $P_2$ , and  $P_3$ ).

where, e.g.,  $s_1$  corresponds to the ratio of the area of triangle  $P_{\text{test}}$ ,  $P_2$ , and  $P_3$  and the total area defined by the points  $P_1$ ,  $P_2$ , and  $P_3$ .

Based on the three barycentric coordinate values, the following cases can be distinguished:

- $s_i \in [0, 1], \forall i \in \{1, 2, 3\}$ : normal case where point  $P_{\text{test}}$  is completely inside. Calculate intersection coordinate with equation (4.1).
- $s_i < 0$ : point  $P_{\text{test}}$  lies below the edge opposite point  $P_i$ . Calculate the distance from point  $P_{\text{test}}$  to the edge sketched in Figure 4.8. If the distance is within the tolerance strip width, a second test is needed to distinguish whether  $P_{\text{test}}$  projected onto the edge lies between the vertex points. Specifically, if the projection ratio  $p = \vec{e} \cdot \vec{t} / |\vec{e}|^2$  is between zero and one,  $P_{\text{test}}$  is an intersection point with the surface triangle including the tolerance strip. If  $p$  is below zero or above one, the distance of  $P_{\text{test}}$  to the closest vertex has to be within the tolerance. If not, there is no intersection with the surface triangle. Then and if

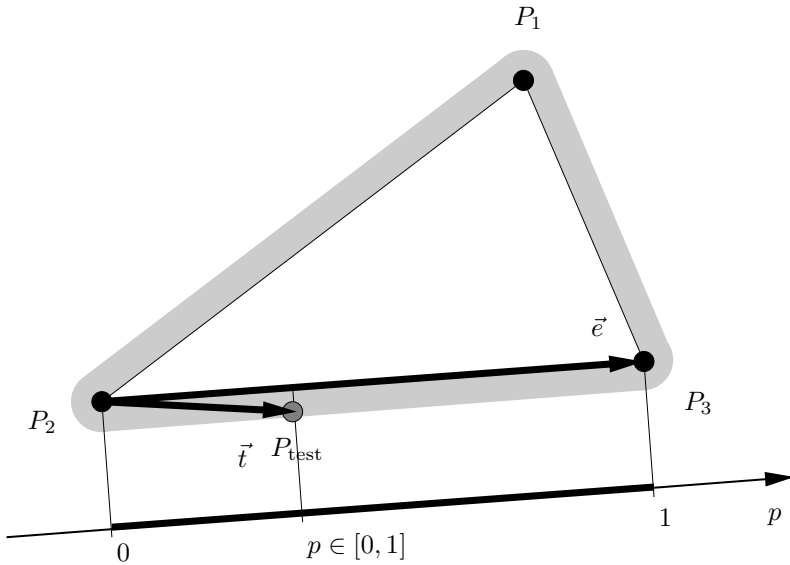


Figure 4.8: Case  $s_1 < 0$ : The point  $P_{\text{test}}$  lies below the line  $\overline{P_2P_3}$ . The triangle is considered as intersected if the distance between this point and the line  $\overline{P_2P_3}$  is within the tolerance strip. If the point  $P_{\text{test}}$  is within the tolerance strip, the on the edge  $\vec{e}$  projected vector  $\vec{t}$  needs to be within  $P_2$  and  $P_3$  or in the circle around these vertex points.

the test was successful, the intersection is calculated again with equation (4.1).

- $s_i > 1$ : If one  $s_i$  is larger than one, then at least one of the other  $s_j$  is negative. Therefore, this case is handled by the case  $s_i < 0$ .

With the surface normal information, each intersection point has a flag to indicate whether it is an entry or exit point (see Figure 4.3). Having calculated all intersection points of one object, the gathered data consist of a collection of grid line indices along of which the corresponding sorted intersection points with the entry/exit flags are stored.

### 4.3.6 Special Cases

The next step is to analyze the calculated intersection points along one grid line. Multiple entry or exit intersection points have to be merged if the distance between them is within a certain tolerance, because they originate from the same surface though the grid line hits two or more adjacent triangles.

The resulting entry–exit pattern could look like in Figure 4.9. To solve the problem described in item 5 of the introduction, a robust, symmetric approach was implemented:

1. keep only the first of consecutive entry points, and
2. keep only the last of consecutive exit points

along one grid line. The case sketched in Figure 4.9 is solved by removing the exit point  $P_4$ , because the following point  $P_5$  is again an exit point. No further computations are needed and the two situations ‘step’ and ‘box’ described in the caption of Figure 4.2 are correctly and automatically discretized.

### 4.3.7 Consistency in Three Dimensions

The technique described in sections 4.3.4 and 4.3.6 is straightforward in one dimension. As already described in item 4 of the introduction, the consistency may be violated in three dimensions. Therefore,

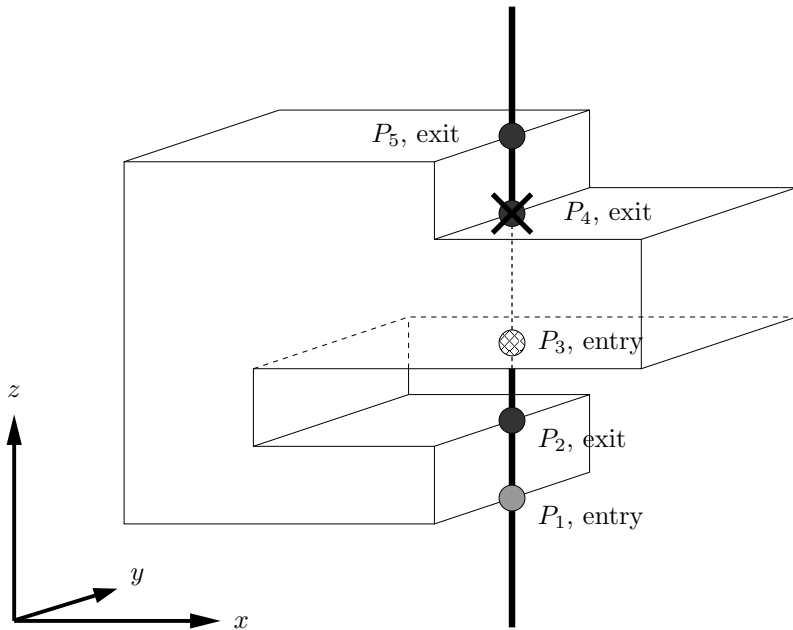


Figure 4.9: Resolve automatically and symmetrically the cases described in section 4.2 by looking at the pattern of entry and exit points: keep only the first of the consecutive entry points and keep only the last of the consecutive exit points. For the depicted situation, exit point  $P_5$  follows exit point  $P_4$ . Following the rule,  $P_4$  is removed from the list. No computational overhead is introduced.

checks and, if necessary, corrections in three dimensions are needed to obtain a consistent conformal mesh. The main strategy is to adjust the stored intersection points. As an example, consider the situation depicted in Figure 4.1. Along the grid line  $y$  the gray point lies inside whereas, along  $x$  the gray point is outside. Lets assume that the grid line along the  $z$  considers the point as lying inside. In this case, the numerical intersection point along the  $x$  is slightly shifted to the left, i.e., to the other side of the gray point.

To accelerate this consistency check, the tested cells are restricted to the vicinity of the object's surface, i.e., the light gray region in Figure 4.3. Finally, the consistent (conformal) mesh is stored with the efficient scan conversion technique explained in section 4.3.4 and sketched in Figure 4.3.

### 4.3.8 Conformal Merging of Different CAD Parts

The last sections described the discretization process for one CAD part. As already mentioned in section 4.3.3, two touching CAD objects need to be merged automatically. Representation inaccuracies of the CAD mesh as demonstrated in Figure 4.6 can lead to empty and overlapping regions while merging two touching objects as depicted in Figure 4.10. As a solution, the conformal information is gathered globally, i.e., one database for all CAD parts, instead of storing the information per part. In addition, while inserting a new conformal cell, the new and the possibly already stored cell is merged. The merging consists of adjusting the vertex materials and the cut-position of the edges. Finally, the merged cell is checked – and if necessary corrected – before storing in the global database.

## 4.4 Conformal FDTD Method

The primary intension of this chapter is the description of a conformal discretization algorithm. The details of the new and robust C-FDTD scheme is introduced in chapter 5.

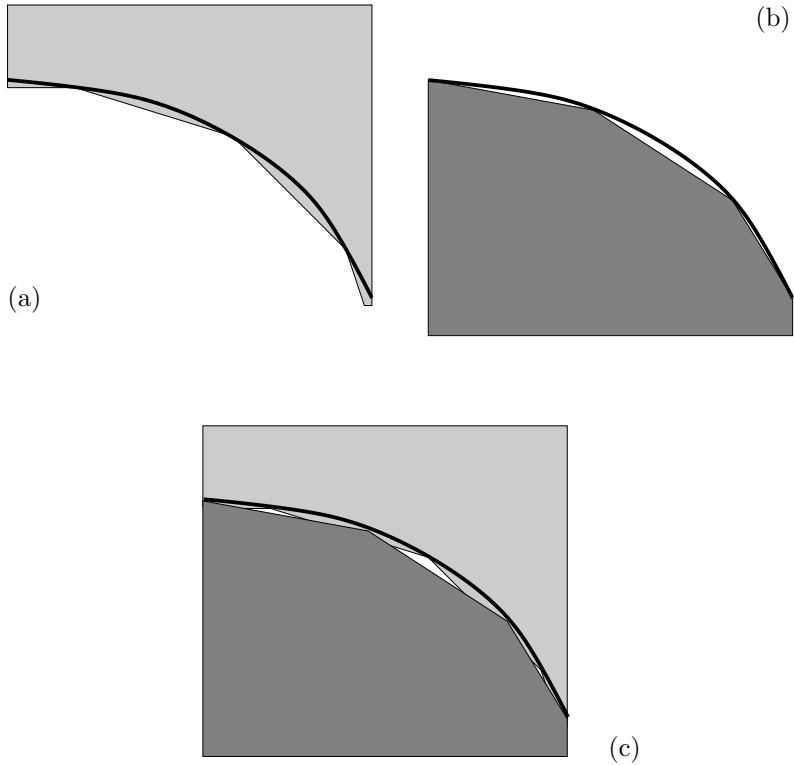


Figure 4.10: In (a) and (b), the two touching CAD parts are sketched with their linear approximation (triangle mesh) of the curved surface. Because their mesh may consist of different surface triangles in the general case, the theoretical interface (bold line) is not exactly represented and can lead to the situation depicted in (c) where some regions are empty and others overlap.

## 4.5 Comparison To Existing Publications

None of the existing publications targeted the efficient and reliable conformal discretization of highly complex CAD models. Therefore, the already published algorithms only partly revealed the sensitive parts.

### 4.5.1 Meshing Technique of Srisukh

Although Srisukh *et al.* [91] calculate staircase meshes on uniform meshes only, they also use the computer-graphic method to accelerate their discretization. For staircase meshes they only discretize along the axis with the longest extent. Therefore, no three-dimensional consistency check was performed.

The intersection point calculation is different, because their first test is to check whether the plane spanned by the facet crosses the grid line. In the algorithm of this chapter, only grid lines within the bounding box of a surface triangle are considered as potentially intersecting, which is much more restrictive to potential intersection lines and, therefore, is more efficient.

In addition, the winding number calculation of [91] is replaced with the computation of barycentric coordinates in the here presented algorithm. Where the winding number calculation is too inaccurate, they introduced the special cases of ‘edge points’ and ‘vertex points’. In the currently presented scheme, these cases could be covered again with the barycentric coordinates in section 4.3.5 and the tolerance strip.

The most complex benchmark is based on two CAD parts with in total 5286 triangular facets. Therefore, the model complexity is beyond the targeted application range of this chapter.

### 4.5.2 Meshing Technique of Waldschmidt

In 2004, Waldschmidt *et al.* published a conformal discretization algorithm based on CAD data [93]. The conformal discretization is based on facets produced with a finite element (FE) mesh generator and on a uniform grid.

The discretization algorithm also calculates the intersection with the plane equation (plane which is spanned by the facet), whereas no tolerances are mentioned to fill numerical gaps between facets to treat badly shaped facets. The computational effectiveness of ‘begins by locating the FDTD edges near the facet’<sup>3</sup> cannot be estimated.

The benchmarks only include sphere and cylinder cavities and a twisted elliptical waveguide. Therefore, the underlying CAD models are trivial. However, the discussion of the results strengthens (1) the effectiveness of the C-FDTD algorithm and (2) the possibility to model the canonical benchmarks with facets instead of analytical functions.

### 4.5.3 Meshing Technique of Su

Su *et al.* [92] developed a general conformal discretization software based on CAD data. However, to reuse their two-dimensional conformal polyline discretization algorithm, they employ the surface triangle description to determine the polylines intersecting a grid plane. Therefore, their approach is different from the efficient three-dimensional scan conversion algorithm used in this chapter. For complex structures, the determination of the polylines from the surface mesh is a computationally intensive operation and, in addition, might become a difficult task for real world models with hundreds of thousands of surface triangles per part. Nevertheless, Su *et al.* were forced to use the concept of ‘virtual lines’ to distinguish between the cases ‘step’ and ‘box’ sketched in Figure 4.2. These additional lines introduce an additional computational overhead and could have been avoided with the same concept described in section 4.3.6 of this chapter.

The presented discretization benchmarks are canonical validations (sphere, tube) and few simple CAD models.

### 4.5.4 Summary

In contrast to the already published discretization techniques, this chapter presents a general and versatile concept, based on the tolerance strip and the entry-exit point pattern along a grid line, to target symmetric discretization, to handle inaccuracies in floating point

---

<sup>3</sup>page 1660 in [93].

operations, and to smooth surface triangle representation. Therefore, no overhead like ‘virtual lines’ and special intersection points ‘edge/vertex points’ are necessary. In addition, the reversed loop in the scan-conversion algorithm of section 4.3.4 is very efficient for calculating all intersections, because the first criterion (within the bounding box) restricts the potential intersection grid lines to only a few. Furthermore, the technique of the efficient scan-conversion algorithm is used throughout the algorithm to accelerate the discretization.

The consistency check in three dimensions (section 4.3.7) for each part and merging of the conformal information into the global discretization database (section 4.3.8) have not yet been mentioned in previous publications. However, they are vital for a consistent conformal mesh.

## 4.6 Results

The conformal discretization algorithm described in section 4.3.3 has proven its performance for complex models. Because of the powerful CAD import and modeling capabilities of the simulation, the discretization of complex environments is straightforward. Therefore, only a selected collection is presented in this chapter.

The first benchmark is the helix antenna shown in Figure 4.11. The CAD model (a) represented with 29’494 surface triangles (b) is shown. The maximal grid spacing was chosen to be the wire radius, and the grid size was  $166 \times 29 \times 30$ . In the same figure the resulting staircase (c) and conformal (d) discretization is shown. The benchmark is highly sensitive to precisely hitting every entry and exit point, because of the approximation of the curved wire surface with surface triangles (Figure 4.6). Therefore, even the grid line running through the outer and inner radius of the helix, which only touch the analytical helix’s surface, is discretized robustly with the help of the tolerance strip and the three-dimensional consistency check.

To extend the CAD model to multiple parts, a flip phone serves as the second benchmark. With 40 distinguished parts represented by in total 230’546 surface triangles, the merging of conformal information of different parts into the global database is demonstrated. The flip phone model in Figure 4.12 was discretized in 24 seconds on both the

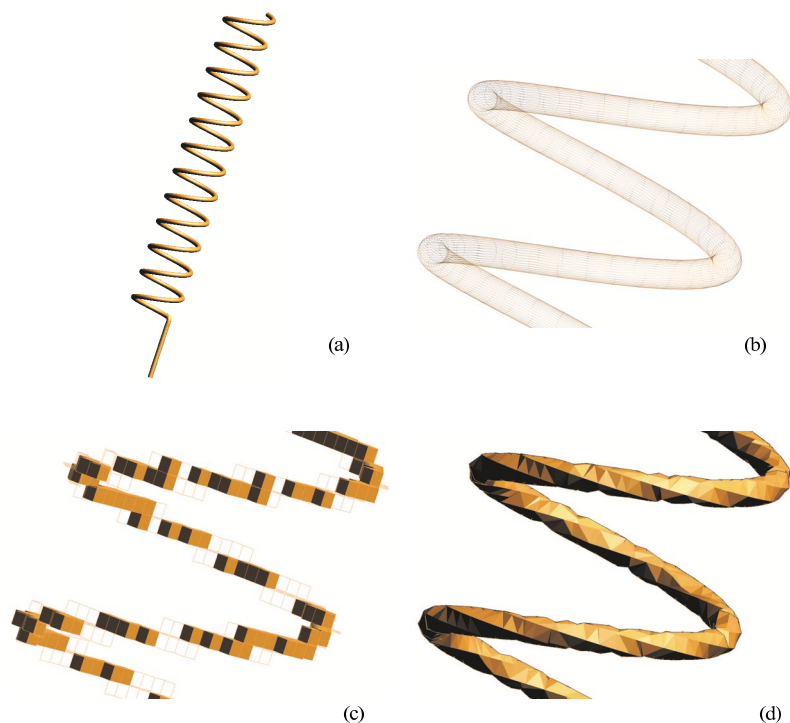


Figure 4.11: Canonical benchmark of a helix antenna: CAD model (a), surface triangles (b) and the staircasing (c) and conformal (d) discretization. The surface triangle mesh consists of 29'494 surface triangles. A nonuniform grid was used with a maximal grid spacing of the wire radius.

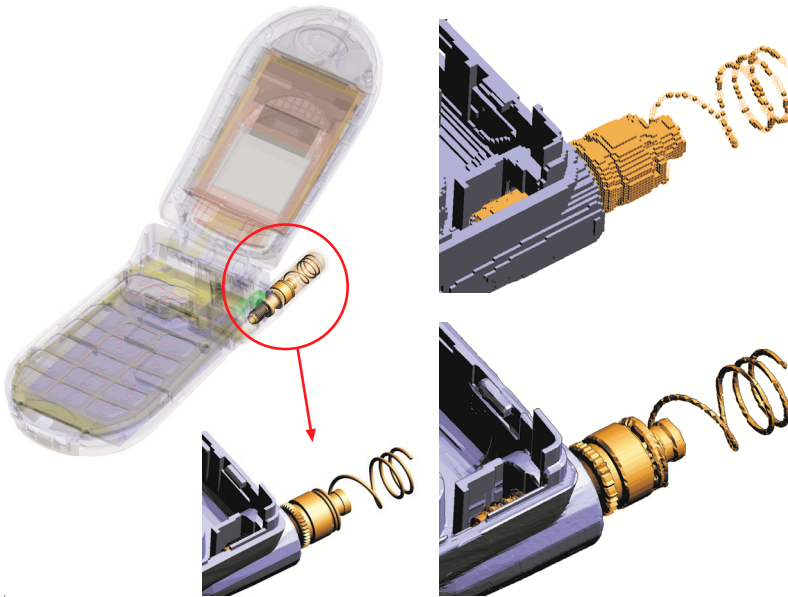


Figure 4.12: Commercial flip phone consisting of 40 distinguished parts. The shown antenna and the case part is represented with 39'960 and 11'280 surface triangles, respectively. The smallest grid spacing is 0.3 mm, whereas the grid consists of 14.6 million cells with a maximal grading ratio of 1.15.

primary and secondary grid on a P4 3GHz. The grid size is  $205 \times 366 \times 195$  with a maximal grading ratio of 1.15. The highly complex phone case and antenna are automatically and robustly discretized.

The commercial hearing aid shown in Figure 4.13 extends the complexity towards real world applications. The more than 100 parts are automatically imported into the simulation platform [2] within minutes. The parts are highly complex, curved and are touching each other. Therefore, aside from the important three-dimensional consistency check per part, the merging of conformal cells of different parts into one overall conformal cell becomes vital.

The last benchmark demonstrates, in addition to the powerful



Figure 4.13: Hearing aid: 106 parts are discretized on a  $201 \times 186 \times 107$  grid. The parts are highly curved. Therefore, conformal simulations have to be favored.



Figure 4.14: Staircase and conformal discretization of the mobile phone and hand is shown together with the SAM CAD model.

conformal discretization, the robustness of the C-FDTD method [96] due to the derived stability criterion. The benchmark was performed within a study with Motorola, investigating the detuning effect by placing the hand and fingers close to the antenna [97]. The model consists of 229 different subparts: complete phone, head and hand with skin, bones and muscles. A conformal simulation with 80 million cells was performed, demonstrating the robustness of the discretization and the C-FDTD method (conformal time step was fixed to 70% of the conventional time step as a tradeoff between accuracy and short simulation time). The boundary is truncated with UPML. In Figure 4.14 the staircase and conformal discretization is shown. A screen shot of the zoomed staircase and conformal discretization is shown in Figure 4.15. Figure 4.16 shows the current distribution on the antenna and some PCB's of the mobile phone.

In summary, the proposed discretization scheme is well suited to robustly discretize complex engineering models. The benchmarks clearly show the benefits of importing CAD formats and the automatic, accurate, and robust discretization.

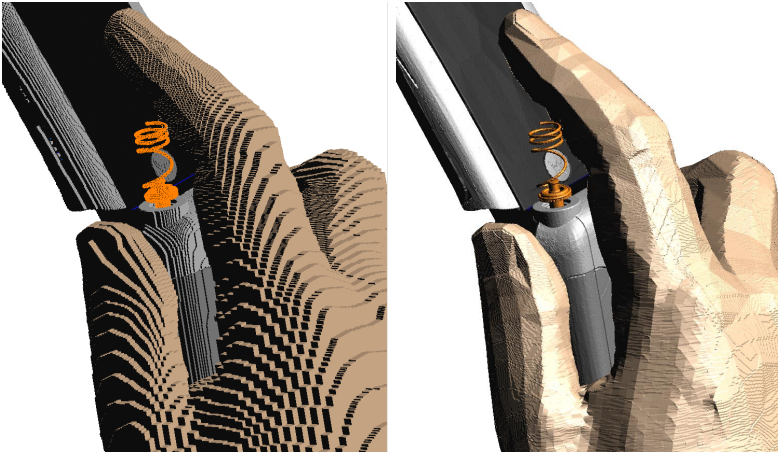


Figure 4.15: Zoom of the staircase and conformal discretization near the antenna of the mobile phone.

## 4.7 Conclusion

The aim of this chapter was to target a conformal mesh generator for highly complex C-FDTD simulations with several hundred millions computational cells and thousands of different parts in the CAD model, represented by surface triangle meshes. Using the scan conversion algorithm borrowed from computer-graphic methods, but looping over the surface triangles instead of grid lines, leads to a highly efficient algorithm suitable for huge grid sizes. Introducing a general concept based on the tolerance strip around a triangle and the entry-exit pattern along a grid line circumvents the inaccuracies of floating point operations and leads to symmetric discretization without the computational overhead of ‘virtual lines’ [92]. In addition, a consistency check in three dimensions performed after calculating all intersections of a CAD part with the grid lines is introduced in this chapter to guarantee a consistent conformal mesh. Merging of the conformal information of different CAD parts is addressed as well, since touching CAD parts do not necessarily share the same surface triangle mesh, which may lead to inconsistencies.

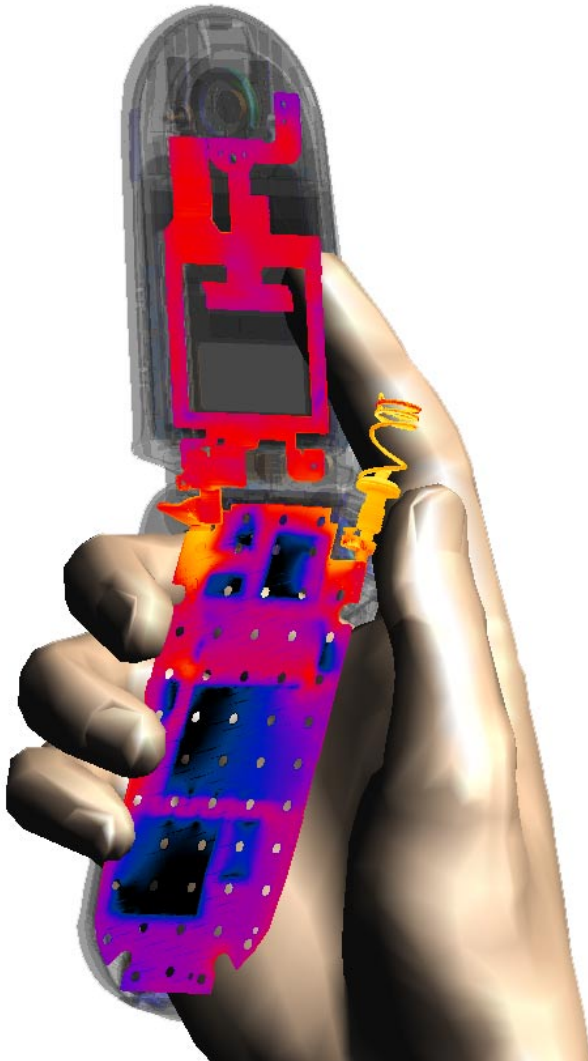


Figure 4.16: Current distribution on the Antenna and the PCB's. The finger close to the antenna is introduced to show the detuning of the antenna while operating.

The discretization algorithm demonstrates its performance in various benchmarks with increasing complexity. As last benchmark, a complete mobile phone next to a head and with fingers placed around the antenna was conformally discretized and simulated.

# Chapter 5

## New 3-D Conformal PEC FDTD Scheme

### 5.1 Abstract

A new conformal finite-difference time-domain (C-FDTD) updating scheme for metallic surfaces nonaligned in the grid is presented in this chapter. In contrast to existing conformal models, the new model can be formulated with the original Yee FDTD update equation. Therefore the proposed scheme can be easily added in standard FDTD codes even if the codes are already parallelized or hardware-accelerated.

In addition, based on the commonly used conventional stability criterion, a derivation of the stability is presented and based on the conformal geometric information, a time step reduction formula is presented. The time step reduction is used as a user-defined parameter to trade off a short simulation time versus accuracy. The achievable geometric precision is optimized to a given time step. Therefore, even with the conventional time step (no reduction) the presented scheme profits from the conformal discretization.

To show the performance and robustness of the proposed scheme canonical validations and two real world applications were investigated. A broadband low profile (circular) antenna was successfully simulated showing the benefit of the conformal FDTD method com-

pared to the conventional scheme. Furthermore, a CAD based mobile phone was conformally discretized and successfully simulated showing that the proposed scheme is highly suited for the simulation of advanced engineering problems.

## 5.2 Introduction

An overview of existing conformal PEC models was presented in section 3.3.2. Therefore, only the recent approaches are summarized here mainly to introduce scheme abbreviations. The latest scheme, using only an altered  $H$  update and an unmodified  $E$  update, was proposed by Dey and Mittra (referred throughout this chapter as DM, [64]). Although the accuracy-gain is good, [65] states that the scheme may suffer from late time instabilities. A remedy for the instabilities was proposed by Yu and Mittra (YM, [65]). Even though YM's approach does not require a time step reduction, [66] reports that the accuracy of the DM algorithm is not maintained.

Recently two schemes have been proposed by Xiao (ECT (enlarged cell technique), [66]) and in the context of the finite integration technique (FIT) by Zagorodnov (USC (uniformly stable conformal), [67]) which do not require a time step reduction but use information from neighboring cells. These schemes are quite simple but are still more difficult to implement than the conventional FDTD codes due to more complex magnetic flux calculations.

This chapter introduces a broad generalization of the approaches of the schemes of YM and DM. The proposed scheme allows to trade off accuracy versus short simulation time. An *a priori* fixed time step reduction is used as the controlling parameter. Inclusion of a derived stability criterion (based on the commonly used conventional stability criterion) maintains constant scheme stability. In addition, incorporating the stability criterion the presented scheme ensures the optimal achievable geometric precision for a given time step while maintaining stability. The proposed scheme recovers the conventional FDTD updating equations but with locally modified coefficients and is therefore more efficient in memory (no split coefficients to store) and in time per update cycle (less multiplications) than YM and DM. In addition because of the simple formulation, every Yee FDTD code

can be enhanced with the conformal scheme by simply modifying the calculation of update coefficients.

### 5.3 Method

In the conformal FDTD algorithm for perfectly electric conductors (PEC) with the conventional staggered grid, the electric ( $\vec{E}$ ) and magnetic fields ( $\vec{H}$ ) are updated in the same way as in the conventional FDTD scheme. Only in the close vicinity of PEC objects the scheme is altered using Faraday's law

$$\frac{\partial}{\partial t} \iint_A \mu \vec{H} \cdot d\vec{A} = - \oint_{\partial A} \vec{E} \cdot d\vec{s} \quad (5.1)$$

where  $A$  denotes an area and  $\partial A$  its boundary,  $t$  is the time, and  $\mu$  is the permeability. The grid nonconformally aligned surface of the object (see Figure 5.1) is taken into account while calculating equation (5.1). The already conventionally discretized result of equation (5.1) yields

$$\begin{aligned} H_z|_{i,j,k}^{n+1/2} = & H_z|_{i,j,k}^{n-1/2} + \frac{\Delta t}{\mu \cdot A_z|_{i,j,k}} \cdot \\ & \left( E_x|_{i,j+1,k}^n \cdot l_x|_{i,j+1,k} - E_x|_{i,j,k}^n \cdot l_x|_{i,j,k} \right. \\ & \left. - E_y|_{i+1,j,k}^n \cdot l_y|_{i+1,j,k} + E_y|_{i,j,k}^n \cdot l_y|_{i,j,k} \right) \end{aligned} \quad (5.2)$$

where  $n$  denotes the time step index,  $\Delta t$  is the time step,  $A_z|_{i,j,k}$  denotes the PEC-free area of the cell face  $(i, j, k)$  with normal  $z$ , and  $l_x|_{i,j,k}$  is the PEC-free edge length of the edge at  $(i, j, k)$  directed along  $x$ . The DM algorithm employs the discretized equation (5.2) with all its advantages but lacks an *a priori* known stable time step.

Recalling the Yee FDTD updating formula (equation (5.2) with

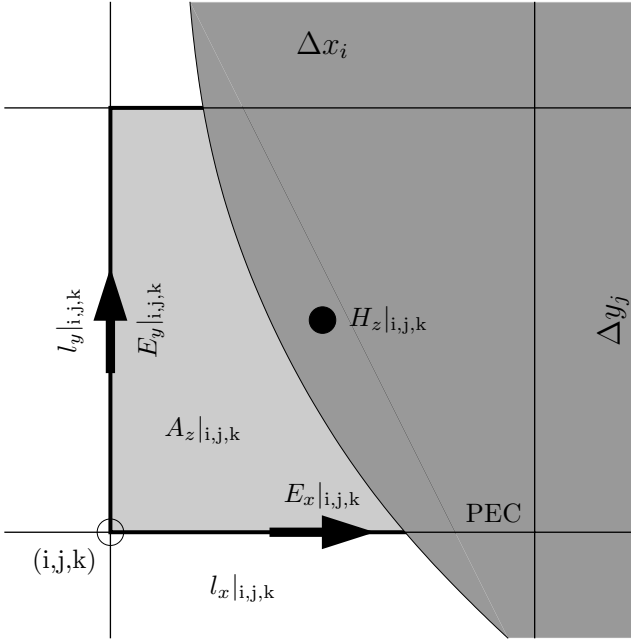


Figure 5.1: A face of a standard Yee cell cut by a PEC object. The lengths  $l_x(i, j, k)$ ,  $l_y(i, j, k)$ , and the area  $A_z(i, j, k)$  are the PEC-free parts.

$$A_z = \Delta x_i \cdot \Delta y_j, \quad l_x = \Delta x_i, \quad l_y = \Delta y_j$$

$$H_z|_{i,j,k}^{n+1/2} = H_z|_{i,j,k}^{n-1/2} + \frac{\Delta t}{\mu} \cdot \left( \frac{E_x|_{i,j+1,k}^n - E_x|_{i,j,k}^n}{\Delta y_j} - \frac{E_y|_{i+1,j,k}^n - E_y|_{i,j,k}^n}{\Delta x_i} \right) \quad (5.3)$$

a curl coefficient can be defined as the factor  $\Delta t/\mu$ . Looking again at equation (5.2), each  $E$  field value is individually shortened by its effective metal-free length, therefore splitting the curl coefficient into four coefficients (referred to below as the *split curl coefficient*).

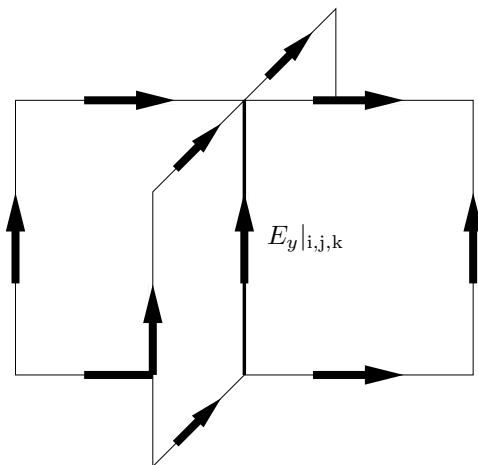


Figure 5.2: The four Yee cell faces sharing the same electric edge  $E$ . In each face,  $E_y|_{i,j,k}$  is shortened by the same factor  $l_y|_{i,j,k}$  according to equation (5.2).

### 5.3.1 Proposed Algorithm

#### Circumvent the Split Curl Coefficient

Considering a single electric edge  $E_y|_{i,j,k}$  and all cell faces containing that edge ( $A_z|_{i,j,k}$ ,  $A_z|_{i-1,j,k}$ ,  $A_x|_{i,j,k}$ ,  $A_x|_{i,j,k-1}$ , see Figure 5.2) the conformal FDTD equation (5.2) always describes the *same* prefactor  $l_y|_{i,j,k}$ . This important fact can be used to circumvent the split coefficients in equation (5.2) by directly storing the product  $l_y|_{i,j,k} \cdot E_y|_{i,j,k}$  instead of only  $E_y|_{i,j,k}$  in the memory. It is worth noting that the algorithm does not change numerically but that only a different value is stored in the memory. The immediate benefits are that equation (5.2) with the above modification performs faster (less multiplications) and that the equation is closer to the Yee update (no split curl coefficient) while still different from the conventional FDTD update (5.3).

### ***H* update equation**

To derive the same update equation for the conformal and conventional updates, some further manipulations are needed. With the definition of the PEC-free relative area and edge ratio (see Figure 5.1)

$$A_z^{\text{ratio}}|_{i,j,k} := \frac{A_z|_{i,j,k}}{\Delta x_i \Delta y_j} \quad (5.4a)$$

$$\Delta_x^{\text{ratio}}|_{i,j,k} := \frac{l_x|_{i,j,k}}{\Delta x_i} \quad (5.4b)$$

equation (5.2) can be reformulated to

$$H_z|_{i,j,k}^{n+1/2} = H_z|_{i,j,k}^{n-1/2} + \frac{\Delta t}{\mu \cdot A_z^{\text{ratio}}|_{i,j,k}} \cdot \left( \frac{E_x|_{i,j+1,k}^n \cdot \Delta_x^{\text{ratio}}|_{i,j+1,k} - E_x|_{i,j,k}^n \cdot \Delta_x^{\text{ratio}}|_{i,j,k}}{\Delta y_j} - \frac{E_y|_{i+1,j,k}^n \cdot \Delta_y^{\text{ratio}}|_{i+1,j,k} - E_y|_{i,j,k}^n \cdot \Delta_y^{\text{ratio}}|_{i,j,k}}{\Delta x_i} \right). \quad (5.5)$$

Equation (5.5) looks very similar to the conventional staircase FDTD update equation (5.3) except for the additional prefactor  $1/A_z^{\text{ratio}}|_{i,j,k}$ , moreover, the  $E_*$  values are individually shortened by their relative PEC-free lengths  $\Delta_*^{\text{ratio}}$ .

To transform equation (5.5) into the standard FDTD update equation, the permeability  $\mu$  is scaled with  $A_z^{\text{ratio}}|_{i,j,k}$

$$\tilde{\mu} := \mu \cdot A_{\text{ratio}} \quad (5.6)$$

and instead of storing the  $E_*$  value the product  $E_* \cdot \Delta_*^{\text{ratio}}$  is stored in the memory (as in Section 5.3.1).

### ***E* update equation**

The  $H$  update retains the same update equation as in the original Yee update. Therefore the remaining task is that in the  $E$  update, the shortening of the  $E_*$  values is taken into account without modifying

the standard FDTD  $E$  update formula. The conventional  $E$  FDTD updating scheme can be written as

$$E_x^{n+1} = \alpha E_x^n + \beta (\nabla \times H^{n+1/2})_x \quad (5.7)$$

where  $\alpha$  and  $\beta$  are scalars (in the lossless case:  $\alpha = 1$ ,  $\beta = \Delta t/\epsilon$ ). Scaling equation (5.7) with the shortening factor  $\Delta_x^{\text{ratio}}$  gives

$$\Delta_x^{\text{ratio}} E_x^{n+1} = \alpha \Delta_x^{\text{ratio}} E_x^n + \Delta_x^{\text{ratio}} \beta \cdot (\nabla \times H^{n+1/2})_x \quad (5.8)$$

$$\tilde{E}_x^{n+1} = \alpha \tilde{E}_x^n + (\Delta_x^{\text{ratio}} \beta) \cdot (\nabla \times H^{n+1/2})_x \quad (5.9)$$

where  $\tilde{E}_x^* := \Delta_x^{\text{ratio}} E_x^*$  is the shortened  $E_x$  value. In other words, the conventional  $E$  updating coefficient  $\beta$  has to be multiplied by  $\Delta_x^{\text{ratio}}$

$$\tilde{\beta} := \beta \cdot \Delta_x^{\text{ratio}}. \quad (5.10)$$

As a result, the  $E$  value shortening is taken into account with no additional computational effort, and the conventional FDTD update equation is also maintained for the  $E$  update.

### 5.3.2 *A Priori* Known Stability Criterion

The conventional FDTD scheme is stable if the time step fulfills the condition (see for example [6])

$$\Delta t < \frac{\sqrt{\epsilon\mu}}{\sqrt{\frac{1}{\Delta x^2} + \frac{1}{\Delta y^2} + \frac{1}{\Delta z^2}}}, \quad (5.11)$$

where  $c = \sqrt{1/\epsilon\mu}$  is the phase velocity,  $\Delta x$ ,  $\Delta y$ ,  $\Delta z$  are the spatial steps, and  $\Delta t$  is the time increment. For complex material distributions and absorbing boundary conditions a general stability analysis is beyond the intention of this thesis. However, in [31] a rigorous proof for inhomogeneous material distribution in a rectangular metal box is presented. For practical grid sizes, the predicted stable time step in [31] is only slightly larger than the one predicted with equation (5.11). At the limit of an infinitely large number of grid lines the two predicted time steps are equal. In general, the time step formula (5.11) is commonly used for nonuniform grids and inhomogeneous sceneries. Assuming the stability criterion (5.11) predicts a

stable time step for nonuniform grids and complex material distributions, a stable time step for the presented method can be proven.

The algorithm described in this chapter manipulates the permeability (see equation (5.6)) in the  $H$  update and the curl coefficient  $\beta$  (see equation (5.10)) in the  $E$  update. In the lossless case  $\beta = \Delta t/\epsilon$  and therefore a modified  $\tilde{\epsilon}$  can be defined as

$$\tilde{\beta} = \Delta^{\text{ratio}} \cdot \frac{\Delta t}{\epsilon} \quad \implies \quad \tilde{\epsilon} := \frac{\epsilon}{\Delta^{\text{ratio}}}. \quad (5.12)$$

With the modified material parameters (equations (5.6) and (5.12)) and equation (5.11) the reduction of the time step of the original Yee update reads

$$\Delta t_A^{\text{PEC model}} = \sqrt{\frac{A_A^{\text{ratio}}}{\max_{\text{edge} \in A} \Delta_{\text{edge}}^{\text{ratio}}}} \cdot \Delta t_A^{\text{Yee}} \quad (5.13)$$

for each cell face  $A$  where  $\Delta t_A^{\text{Yee}}$  is the conventionally calculated time step of the considered cell face  $A$ . Note that if there is no PEC object in the immediate vicinity, the conventional time step is recovered. Furthermore, if  $A^{\text{ratio}}$  vanishes (face is completely inside PEC) every  $\Delta_{\text{edge}}^{\text{ratio}}$  also vanishes, and therefore this face is not taken into account for the time step calculation. In the special case of a uniform grid with constant dielectric background and only PEC objects within the simulation, the global time step has to be reduced by the factor

$$\text{CFL}_{\text{reduction}}^{\text{uniform grid}} = \min_{\text{all cell faces } A} \sqrt{\frac{A_A^{\text{ratio}}}{\max_{\text{edge} \in A} \Delta_{\text{edge}}^{\text{ratio}}}}. \quad (5.14)$$

An important fact is that the time step can be calculated in advance by knowing only the conformal geometric information and is therefore known *a priori*.

### 5.3.3 Short Simulation Time Versus Accuracy

The stability criterion (5.13) has no lower limit, and therefore in some cases the time step has to be decreased to a tiny fraction of the conventional time step. Reducing the time step too much leads to an

exceedingly high number of iterations in time, which is not convenient for practical purposes.

In the following, a new algorithm is described to overcome this strong practical limitation. The derived stability criterion (5.13) is used to guarantee continuous stability while the time step reduction is kept at user-defined level. In detail, a parameter (here called *CFL*) is introduced which sets the reduction of the standard FDTD time step:

$$\Delta t^{\text{PEC model}} = \text{CFL} \cdot \Delta t^{\text{Yee}}, \quad \text{CFL} \in (0, 1]. \quad (5.15)$$

While calculating the FDTD update coefficients for an  $H$  component, the conformal time step (5.13) is computed. If the conformal time step is below the limit of the time step calculated with equation (5.15), the ratio of the area  $A^{\text{ratio}}$  is increased until the time step is above the conformal time step. The standard  $H$  update coefficient is computed with the modified  $A^{\text{ratio}}$  and equation (5.6).

This algorithm ensures that the local time step  $\Delta t_A^{\text{PEC model}}$  never falls below the global simulation time step. Therefore the scheme guarantees both the continuous stability and the applicability to a wide range of complex models. Furthermore, the parameter *CFL* is used to trade off short simulation time ( $\text{CFL} \rightarrow 1$ ) and accuracy ( $\text{CFL} \cdot \Delta t^{\text{Yee}} \rightarrow$  equation (5.13)).

### 5.3.4 Optimal Geometric Precision for A Given Time Step

This section demonstrates that the proposed scheme optimally connects a given time step with the achievable geometric precision.

#### Nonuniform Grid

On nonuniform grids the conventional local time step of cell faces  $\Delta t_A^{\text{Yee}}$  can vary a lot throughout the grid. Therefore, a conformal coarse cell can incorporate a larger decrement of the conventional local time step and still satisfies the global time step. Hence, without any drawback a coarse cell can be conformally resolved more accurately than a smaller cell.

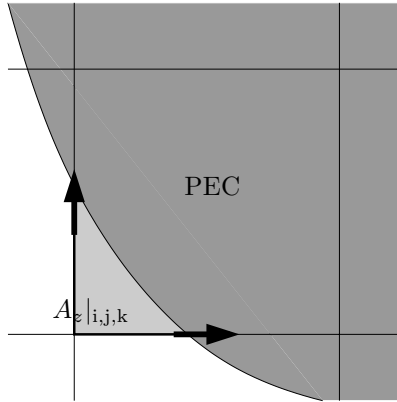


Figure 5.3: A small area fraction.

### Different Surrounding Dielectrics

If the metal object is touching two different dielectrics, the dielectric with the larger permittivity has again a larger conventional local time step for the same cell size. Therefore, it is again conformally resolved more accurately with the presented scheme than the cells with the dielectric with the smaller permittivity.

### Small Largest Dielectric Edge Length in Cell's Face

The case of a small area fractions like in Figure 5.3 is considered. Even if the cell is the smallest of the grid and the time step is not reduced ( $CFL = 1$ ), the area  $A_A^{\text{ratio}}$  can be decreased (YM uses always  $A^{\text{ratio}} = 1$ ) because the maximal metal-free edge ratio  $\max \Delta_{\text{edge}}^{\text{ratio}}$  is less than one (see equation (5.13)). Again the best geometric precision for a given time step is used in that cell.

In summary, the algorithm described in section 5.3.3 ensures the optimal achievable geometric precision for a given time step.

### 5.3.5 Proposed Method Compared to Published Ones

#### DM method

The conformal method of DM uses directly equation (5.2) but may suffer from late time instabilities (see [65]) due to a lack of a derived stability criteria. The simulation-experiment based DM stability criteria (see [64]) were to limit  $A^{\text{ratio}}$  and the  $\max(\Delta^{\text{ratio}})/A^{\text{ratio}}$  of a cell. In Section 5.3.2 it is shown that only the inverse of the second rule is restrictive for the proposed scheme, while the first one has no correspondence and is therefore not limiting. The here proposed scheme averts the need of split coefficients (Section 5.3.1). Furthermore, if the stability criteria are not fulfilled, the proposed scheme limits the non-metal-area reduction whereas DM uses expansion of cells like in the contour path FDTD method (e.g., [40]) for that small area or completely ignores it. For nonuniform grids the criteria of DM are not appropriate to ensure to get the best geometric precision (see section 5.3.4).

#### YM method

To circumvent the instabilities of the DM method, the newer YM method proposes skipping the reduction of the area  $A_z$ . Looking at equation (5.13) with  $A^{\text{ratio}} = 1$  there is obviously no need for the time step reduction. However, the accuracy suffers from this modification (see [65]). Even with the conventional time step ( $\text{CFL} = 1$ ) on a uniform grid the scheme proposed in this chapter can profit more from small areas like in Figure 5.3 than YM's scheme because the  $A^{\text{ratio}}$  can be decreased without violating the stability criterion (5.11) (see section 5.3.4).

#### PFC (partially filled cell, FIT)

Aside from the different context (FIT versus FDTD method), the differences from the presented scheme compared to the PFC method proposed in [67] are that the PFC method does not limit the area reduction  $A^{\text{ratio}}$  and directly alters the permittivity matrix of the FIT-algorithm. Although its performance was shown in 2-D only, the

algorithm fits well into the standard FIT framework. However, the PFC method considers a small metal-free area as completely filled with PEC, whereas the scheme presented here never treats such cells as completely filled. In addition, the PFC method does not allow to optimize the performance towards short simulation time or accuracy.

### **ECT (enlarged cell technique)**

The enlarged cell technique described in [66] uses a different approach to the method presented here. In addition to the proposed scheme, the H update equation of ECT includes conformal information of neighboring cells. Therefore the neighboring cells (called intruded cells in [66]) have a modified H update to conserve the magnetic flux as well. Hence, the algorithm is more complex than the conformal method presented here. As an additional complexity an intruded cell cannot be a candidate to be enlarged (e.g., the metal-free part needs to be more than half for each intruded cell) which may be difficult to satisfy for complex models. On the other hand, a cell face with a metal-free part of more than 50 % is *not* enlarged. However, without a proof, but validations with canonical benchmarks, the authors of ETC report that the conventional time step can be used. For the described case, the method presented in this chapter would need a time step reduction to resolve all geometrical details (favor accuracy).

### **USC (uniformly stable conformal, FIT)**

The uniformly stable conformal FDTD method [67] was published before the ECT method in the context of FIT. The constitutive law  $B = \mu H$  represented with the matrix  $M_\mu$  is altered such that off-diagonal elements link critical conformal cells to their adjacent cells. Again, a cell face with a metal-free part of more than 50 % is considered as non-critical. With validations in two dimensions, but without a general proof, the authors report that the conventional FDTD time step can be used.

## 5.4 Numerical Results

In this Section the robustness and effectiveness of the proposed scheme is demonstrated on the basis of canonical validations as well as real world applications with increased complexity.

### 5.4.1 Mie Scattering of Metal Sphere

To outline the effect of the time step reduction and therefore the trade off of accuracy versus short simulation time, the near and scattered fields of a metal sphere irradiated by an incident plane wave (total field, scattered field) were investigated. The analytical solution is calculated by Mie series. A ten layer PML was used as the absorbing boundary condition. The simulation was run until it reached steady state. The discrete norm  $L_2^h$  (square root of the mean value of squared differences) was used to compare the simulated  $E$  field to the analytical solution. The near field region is a box with side length  $1.21\lambda$  ( $= 14$  cells for the coarsest mesh ( $\lambda/11.54$ )<sup>1</sup>) around the sphere's center<sup>2</sup>. The radius of the sphere is  $\lambda/5.77$  ( $= 2$  cells for the coarsest mesh).

The relative errors of near field and scattered field on different grids were investigated ( $\Delta x = \lambda/11.54$ ,  $\Delta x = \lambda/23.1$ ,  $\Delta x = \lambda/46.2$ ). They revealed all the qualitatively same error plots comparing the staircase simulation and proposed method. Therefore only the relative near field errors on the  $\Delta x = \lambda/46.2$  grid are shown in Figure 5.4.

Looking at Figure 5.4 the improvements of the conformal FDTD method compared to the conventional one are obvious. The YM scheme improves the accuracy compared to the staircase solution. However the proposed scheme with  $\text{CFL} = 1$  can profit more from small cells due to the argument in section 5.3.4. Using the DM scheme, the accuracy can be improved even more. However, it suffers from example dependent late time instabilities as discussed in section 5.3.5. In summary, the optimum solution will be achieved using the method presented in this chapter while applying a slight reduction of the time

---

<sup>1</sup>Five conventional time steps are equal to a quarter of a period, which eases the harmonic field values computations.

<sup>2</sup>Tests with other sizes revealed the qualitatively same error improvements

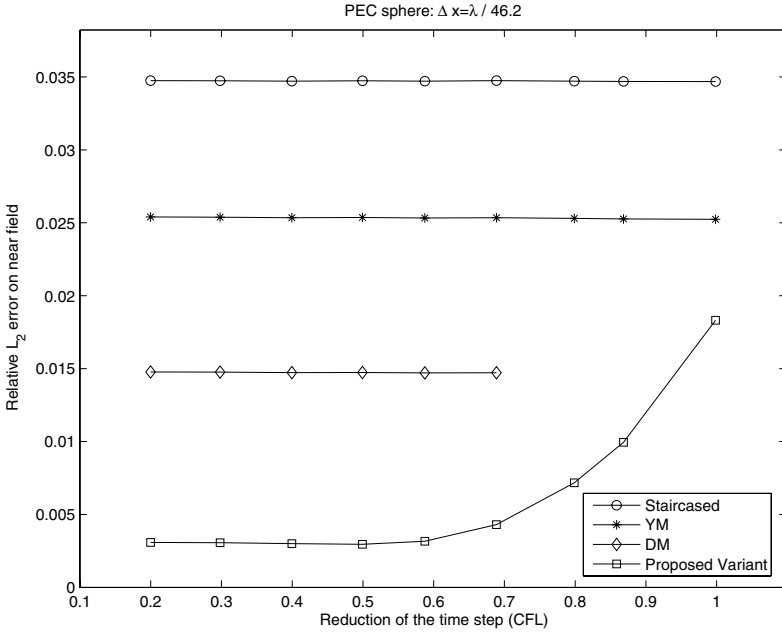


Figure 5.4:  $L_2$  near field error on a grid  $\Delta x = \lambda/46.2$ . The scheme presented in this chapter shows that the user can trade off short simulation time versus accuracy with the chosen CFL number.

step. Observing the curve of the proposed scheme, the accuracy profits from the time step reduction. Time step reductions of more than 30% do not improve considerably the accuracy (trade off short simulation time versus accuracy).

### 5.4.2 Broadband Low Profile Antenna

The next benchmark consists of the broadband low profile antenna described in [98]. A circular patch of 21 mm radius is located at 10 mm above a ground PEC plane. Two 10 mm off-centered metal rods of 1 mm radius short the patch with the ground plane. The antenna is excited at the center metal cylinder (radius 2 mm) with an edge source

and a 1 mm gap between the cylinder and the ground plane (see also Figure 5.5). The excitation signal was a sinusoidal Gaussian with a center frequency of 2 GHz and a bandwidth of 1 GHz. The simulation was run until each field value of the domain has completely decayed. Seven PML layers were used as the absorbing boundary condition.

In Figure 5.6 the return loss is shown. The reference solution was calculated with method of moments (MoM). A significant improvement is achieved by conformal FDTD method with respect to both memory consumption and simulation time: the same accuracy is achieved with conventional FDTD method (18.2 minutes on an Intel P4, 2.7 GHz, 540'000 cells) as with the conformal one (70% CFL, 0.8 minutes, 18'000 cells).

### 5.4.3 Mobile Phone

Whereas Sections 5.4.1 and 5.4.2 mainly focus on an analysis of accuracy and efficiency of the proposed scheme, this Section shall outline its robustness with respect to highly complex configurations, e.g., CAD derived devices. In addition, to also demonstrate its wide application range, a model of a commercially available mobile phone was chosen and simulated at 1.85 GHz. The CFL reduction for the conformal simulation was selected as 50% to ensure that the number of time iterations was not exceedingly high.

The automatic, efficient and robust discretization algorithm described in chapter 4 enables the simulation platform [2] to handle these complex simulations. In Figure 5.7 the staircase and conformal discretizations of the flip phone joint are shown.

The conformal simulation with 2.8 million cells is compared to a fine staircase simulation with 12.1 million cells. The simulation time was 81 minutes for the conformal run and 277 minutes for the staircase run on an Intel P4, 2.7 GHz. The near field RMS  $|\vec{E}|$  was plotted on a plane 5 mm below the lowest point of the antenna. In Figure 5.8 the contour plots of that plane are shown. The maximum is located nearest to the tip of the antenna, and the bright line in the upper picture is along the antenna. Along that line the relative error  $L_2^h$  of the conformal simulation compared to the fine reference one is only 2.4 %, regarding the reduced computational resources achieved. Small deviations are also obtained observing the feed point impedance which

changes from  $45.8 + j 1.07 \Omega$  to  $45.6 - j 1.45 \Omega$  for conformal and fine simulation, respectively. No significant deviations were observed in the far-field.

With the provided stability criterion, even for this complex geometry no instabilities occurred. The proposed scheme is therefore highly suitable for solving real-world problems.

## 5.5 Conclusion

In this chapter a new conformal PEC algorithm for the FDTD method is presented. In contrast to existing models, the proposed scheme fits well into the original Yee FDTD updating scheme, i.e., it only requires changes in the calculation of the two field update coefficients while keeping the implementation of the original Yee FDTD temporal update unmodified. Therefore, the scheme can be added to existing standard FDTD codes with only minor effort. Furthermore, the new method needs fewer multiplications per update cycle, it is faster, and moreover stores only two instead of five coefficients. Finally, it is more memory efficient than the schemes presented in [64] and [65].

A key advantage of the proposed scheme is that a stability criterion has been derived based on the commonly used conventional stability criterion and it was related to the quality of the conformal approximation. Choosing a time step reduction the user can privilege either a short simulation time or accuracy according to the needs of the application.

Validations on the basis of benchmark examples as well as targeting complex industrial applications have shown the performance and robustness of the proposed scheme enabling an improved spatial modeling and simulation of complex 3-D real world structures. Combined with powerful discretization algorithms the new method constitutes a significant benefit and performance increase for electromagnetics related applications in general and for mobile communication and medicine in particular.

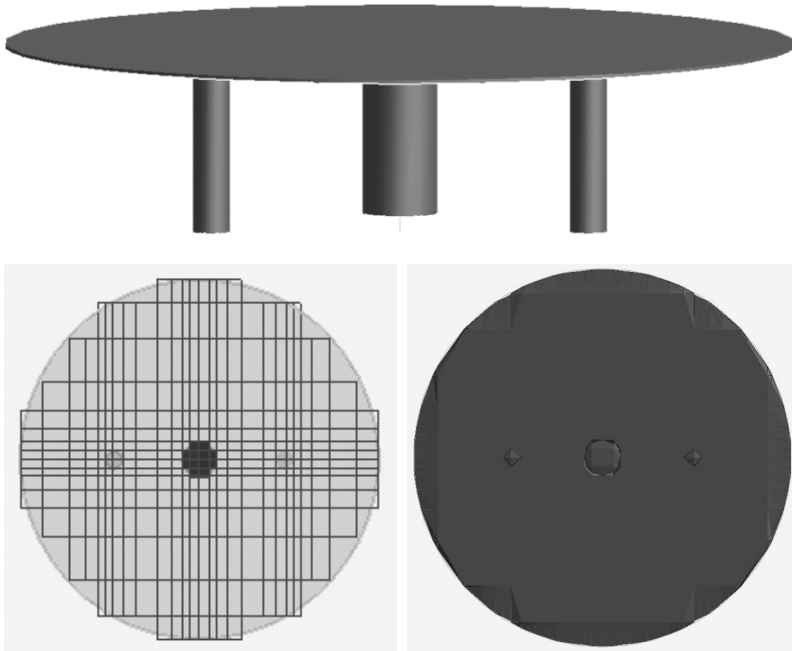


Figure 5.5: In the upper part the CAD model of the broadband low profile antenna [98] is shown. The excitation (small line) is between the center rod and the PEC ground plane. The ground plane is not drawn in the picture. In the lower left corner the staircase discretization is shown while the conformal discretization is depicted to the right.

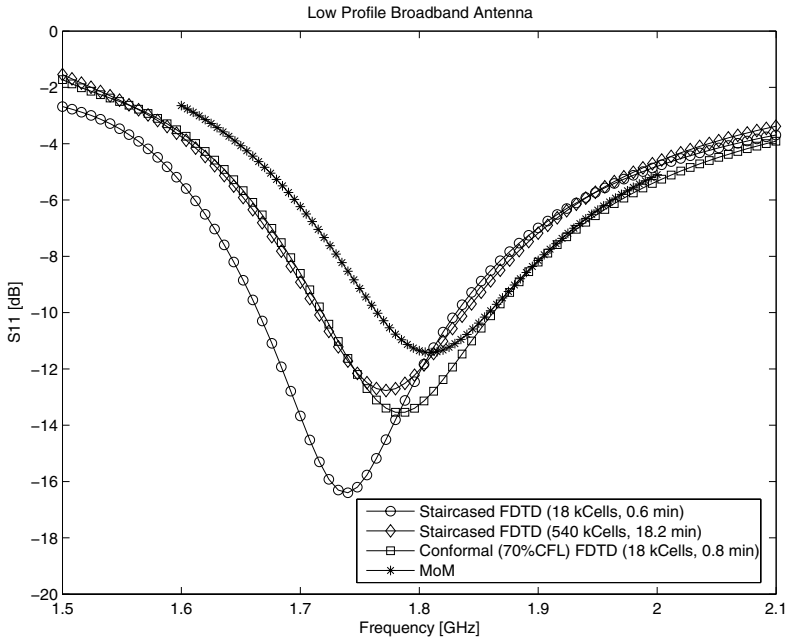


Figure 5.6:  $|S_{11}|$  of the broadband low profile antenna. With a time step reduction of only 30% the return loss is improved considerably.

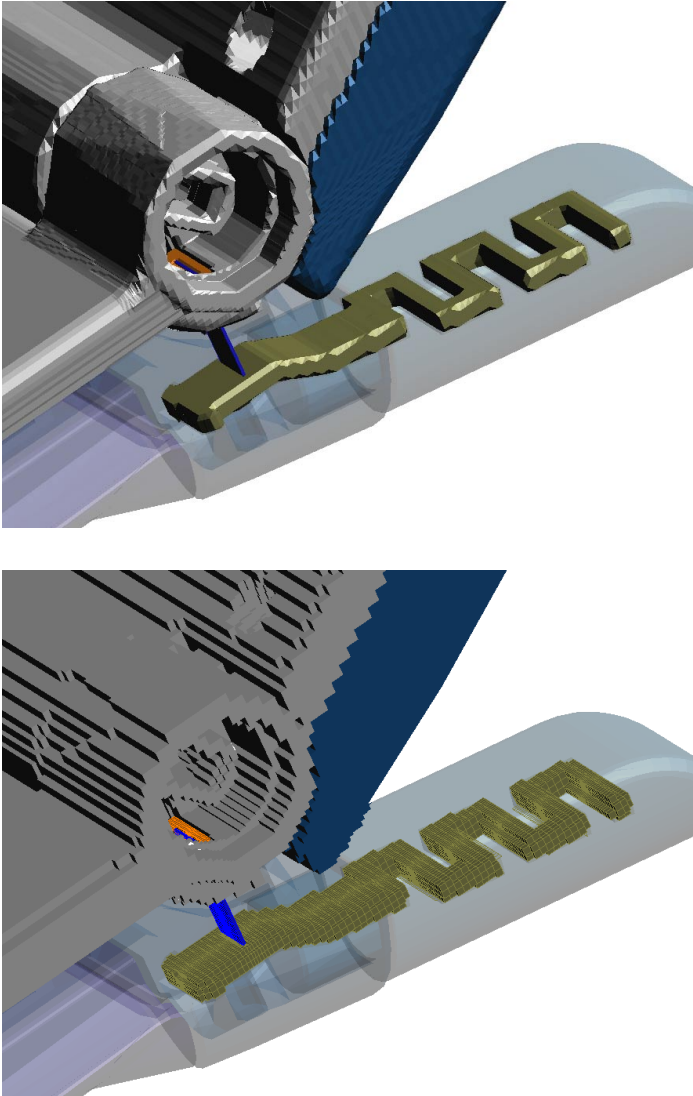


Figure 5.7: The joint of a flip phone discretized conformally (above) and staircased (below).

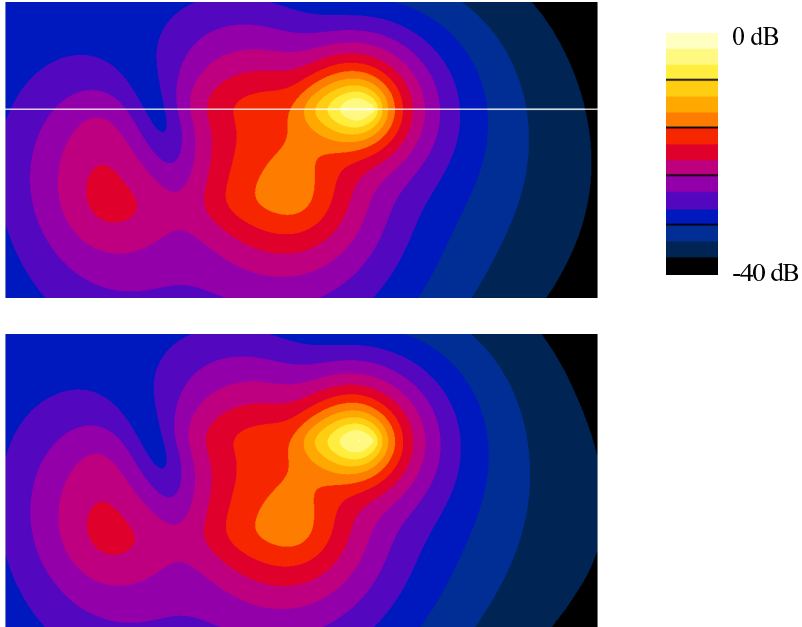


Figure 5.8: Contour plots of  $\text{RMS}|\vec{E}|$  in a plane 5 mm below the lowest point of the antenna. In the above Figure, the fine staircase simulation (up) and the conformal simulation (below) are shown. The dynamic range is 0 to -40 dB, where 0 dB corresponds to the maximum value. The maximum is located nearest to the tip of the antenna. The horizontal line in the upper plot is the line along the antenna and along which the coarse staircase and coarse conformal simulations are compared with respect to the discrete  $L_2^h$  norm.

# Chapter 6

## Conformal Dielectric FDTD Schemes

### 6.1 Introduction

Chapter 5 introduced a novel conformal model to treat curved metal interfaces. This chapter concentrates on interfaces between two dielectrics. As mentioned in section 3.3.1, the most efficient and robust techniques are models based on effective material parameters. Therefore, different techniques to retrieve effective material parameters are investigated in this chapter.

### 6.2 Method

As indicated in the survey of section 3.3.1, the effective material parameters can be obtained in various ways. Figure 6.1 sketches different regions across which the weighted average can be calculated. In (a) the staircase approach is shown, which calculates the parameters out of the four computational cells sharing the electric edge  $E_y|_{i,j,k}$ , e.g., weighted by their volume or simply the mean value. The conformal average region (b) averages along the electric edge, whereas (c) averages across the area defined by the secondary grid face. The conformal

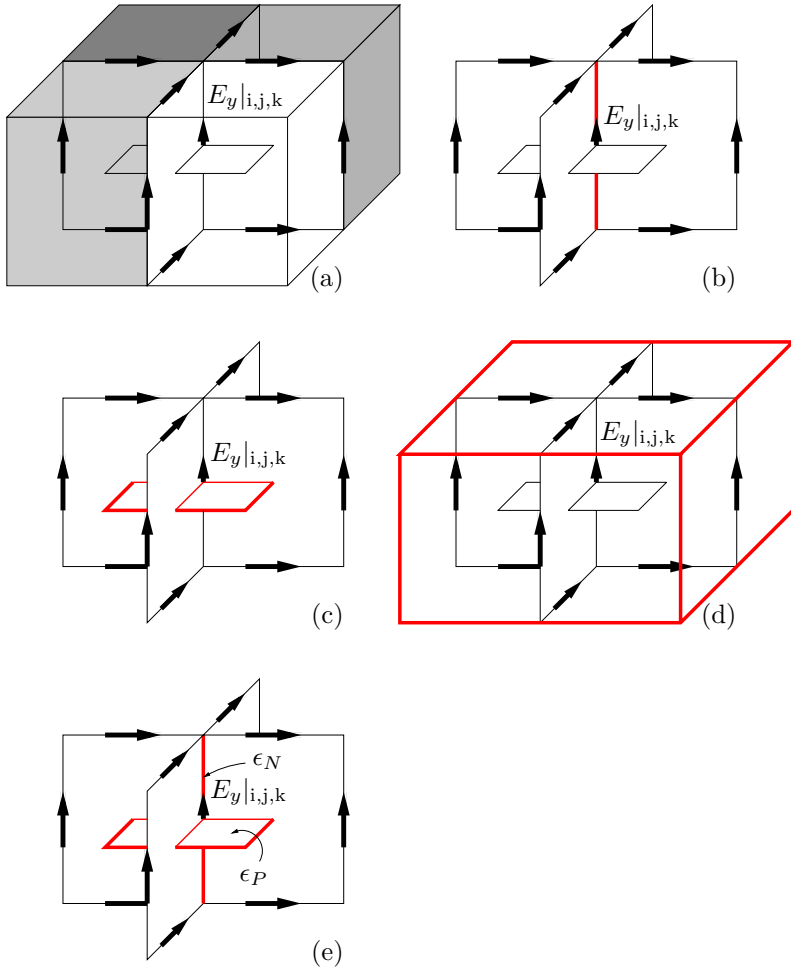


Figure 6.1: Different averaging schemes: (a) staircase model with cell based dielectric parameters; (b) conformal edge based average; (c) conformal area based average; (d) conformal volume based average; (e) conformal edge/area based model taking into account the normal of the interface.

average region (d) consists of the same region as (a) but uses the conformal information.

In addition to different averaging regions, different average formulas can be used:

$$\epsilon_{\text{arithmetic}} := \frac{\sum_{i=1}^n w_i \epsilon_i}{\sum_{i=1}^n w_i} \quad (6.1a)$$

$$\epsilon_{\text{harmonic}} := \frac{\sum_{i=1}^n w_i}{\sum_{i=1}^n \frac{w_i}{\epsilon_i}} \quad (6.1b)$$

where  $w_i$  is a weight, e.g., edge length, area, or volume of material  $i$ .

Within this context the existing conformal FIT algorithm [8] is model (c) with arithmetic averaging, the published scheme of Dey [50] is similar to (d) with arithmetic averaging, and the method of Yu [52] is (b) with arithmetic averaging. The staircase solver of the simulation platform SEMCAD X uses the scheme of Yu [51], which is the model (a) and arithmetic averaging weighted with the cell's volume.

The theoretical results of Hirono [48] and Hwang [49] of perfectly parallel or orthogonal material interfaces can be obtained with arithmetic averaging across face Figure 6.1 (c) and harmonic averaging along edge Figure 6.1 (b), respectively.

These theoretical findings of Hirono and Hwang were the basis to propose a novel dielectric subcell model based on the ideas of Lee [53] and Mohammadi [60] using the 3-D normal of a material interface. In detail,  $\epsilon_N$  is calculated along the primary edge with harmonic averaging (see Figure 6.1 (e))

$$\epsilon_N := \frac{1}{\frac{\Delta_1^{\text{ratio}}}{\epsilon_1} + \frac{\Delta_2^{\text{ratio}}}{\epsilon_2}} \quad (6.2)$$

to exactly fulfill the boundary conditions for object surfaces perpendicularly cutting the considered edge where  $\Delta_i^{\text{ratio}}$  is the edge length fraction belonging to the material  $i$ . Simultaneously,  $\epsilon_P$  is arithmetically averaged across the area on the secondary grid perpendicular to

the considered primary edge

$$\epsilon_P := A_1^{\text{ratio}} \cdot \epsilon_1 + A_2^{\text{ratio}} \cdot \epsilon_2 \quad (6.3)$$

where  $A_i^{\text{ratio}}$  denotes the area fraction belonging to material  $i$ . The parallel electric permittivity  $\epsilon_P$  exactly fulfills the boundary conditions in the case of an object surface normal perpendicular to the edge. The correct interface normal  $\vec{n}$  is used to calculate the projected effective permittivity

$$\epsilon_{\text{eff}} := n_y^2 \epsilon_N + (1 - n_y^2) \epsilon_P \quad (6.4)$$

where  $n_y$  is the  $y$  component of the normalized interface normal  $\vec{n}$  along the considered primary edge  $E_y$ .

### 6.3 Results

Within the simulation framework of SEMCAD X, twenty different models were implemented and validated using the averaging regions in Figure 6.1 and three averaging formulas, i.e., (6.1) and arithmetic averaging of  $\sqrt{\epsilon}$  (refraction index of optics). A discussion of all of the conformal dielectric models is out of scope of this chapter. However, the most popular schemes [51, 52, 8, 50] are compared to the new proposed scheme (6.4) derived in this thesis.

The subcell models are validated using a validation setup similar to the one in section 5.4.1 for the PEC model. The dielectric sphere has a permittivity of  $\epsilon = 4$  and was irradiated by a plane wave at 3 GHz. Again the Mie series serve as an analytical reference solution. To explore the influence of the staircasing approximation, the radius of the sphere is varied from 8 mm up to 36 mm on the uniform grid with  $\Delta = 8 \text{ mm} = \lambda_{\text{vacuum}}/12.5 = \lambda_{\text{sphere}}/6.25$ .

Figure 6.2 shows the relative  $L_2$  error of the near field of the different subcell models versus the radii. Obviously, the *staircase volume arithmetic* model [51] produces a highly varying error along the radii due to staircase approximation. The implementation of the *conformal volume arithmetic* model [50] is across 4 cells and therefore blurs the correct interface location due to its large volume. Therefore, the findings of medium accuracy are not surprising in Figure 6.2. The method

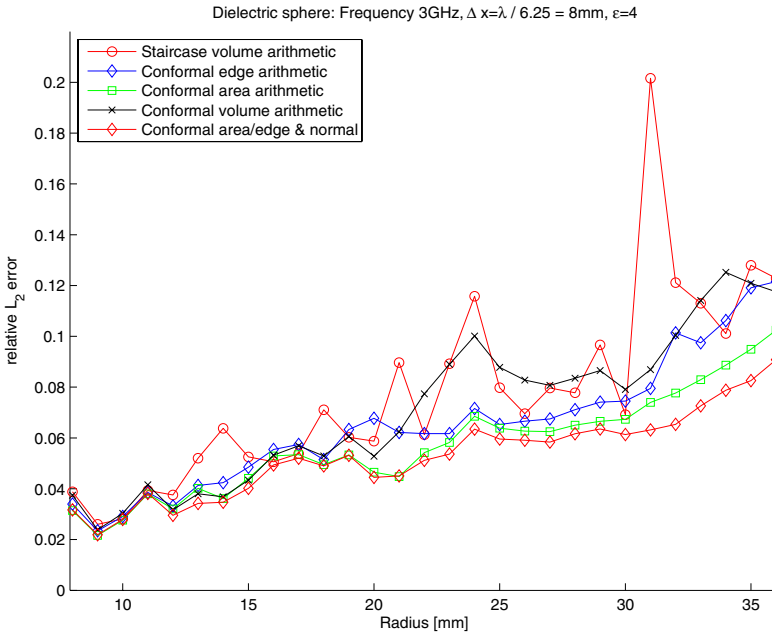


Figure 6.2: The relative  $L_2$  errors of the numerical solution compared to the analytical Mie series solution for different sphere radii and different dielectric subcell models.

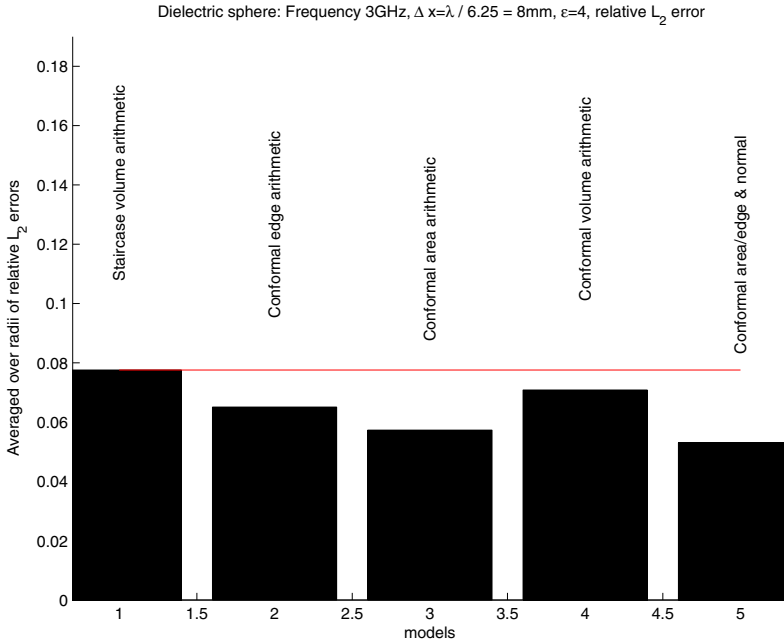


Figure 6.3: The average of the errors of Figure 6.2 plotted for each model. The lower the averaged error, the more accurate is the conformal model.

*conformal edge arithmetic* [52] has medium accuracy as well. The approach of the FIT *conformal area arithmetic* [8] results in a smooth error across the radii. However, the proposed subcell model *conformal area/edge & normal* incorporating the interface's normal (6.4) results in the best accuracy. The mean value of the errors across all radii is shown in Figure 6.3, strengthening the above findings.

# Chapter 7

## Field Singularity Subcell Models

### 7.1 Introduction

This chapter presents the theory of edge field singularity models used later on in the subcell enhanced ADI-FDTD method in chapter 8. In section 3.3.3 the topical literature is summarized.

### 7.2 Method

Quasi-static fields of a sharp edge of an isolated thin metal sheet can be approximated by [68]

$$E_r \propto \frac{\cos(\phi/2)}{\sqrt{r}} \quad (7.1a)$$

$$E_\phi \propto \frac{\sin(\phi/2)}{\sqrt{r}} \quad (7.1b)$$

$$E_z \propto \sqrt{r} \cos(\phi/2) \quad (7.1c)$$

where  $r$  is the distance to the metal edge and  $\phi$  is the angle from the metal surface as depicted in Figure 7.1. Similar formulas hold for the

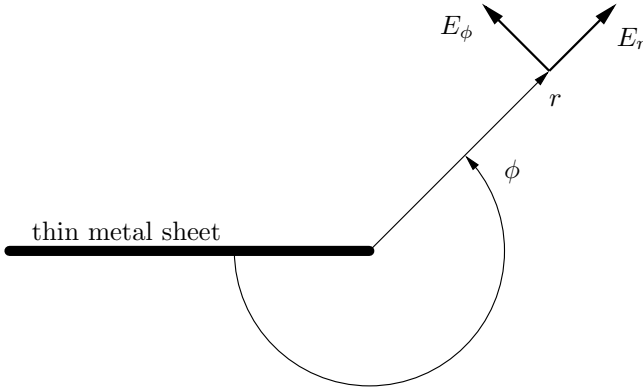


Figure 7.1: Definition of the radial and angular parts of the singular electric field near an edge of a PEC sheet.

behavior of the magnetic field [68].

The line correction factor approach of Shorthouse *et al.* [70] states that

$$\int_{x_1}^{x_2} E_x(x) dx = E_x((x_1 + x_2)/2) \cdot (x_2 - x_1) \cdot c \quad (7.2)$$

where  $c$  is the correction factor between the field value in the center and the integral value. The fact of sharing the same prefactor for all four areas (Chapter 5, Figure 5.2) can again be seen and used in the update. Therefore, the correction factor  $c_r$  for edges directly adjacent to the metallic edge (Figure 7.2) is calculated by

$$c_r := \frac{\int_0^{\Delta x} E_r(r) dr}{\Delta x \cdot E_r(\Delta x/2)} = \frac{\cos(\phi/2) \int_0^{\Delta x} \frac{dx}{\sqrt{r}}}{\cos(\phi/2) \frac{\Delta x}{\sqrt{\Delta x/2}}} = \sqrt{2} \quad (7.3)$$

and is independent of the spatial resolution  $\Delta x$  and the angle  $\phi$ . Thus, the FDTD  $E$  update coefficient is altered by  $\tilde{\beta}_E = c_r \cdot \beta_E$ .

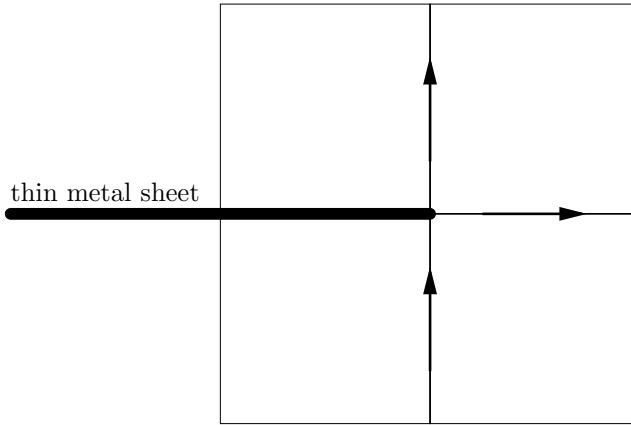


Figure 7.2: The three modified radial electric field edges.

## 7.3 Results

A simple patch antenna designed for 2 GHz mounted on a generic phone serves as the demonstration benchmark. The patch antenna depicted in Figure 7.3 consists of a metal box with the dimensions  $200 \times 70 \times 20 \text{ mm}^3$ , a dielectric substrate ( $70 \times 50 \times 3.175 \text{ mm}^3$ ) with a permittivity of 2.2 and a metallic patch ( $48.44 \times 30 \text{ mm}^2$ ). The voltage edge source excitation is 38.8 mm from the top of the metallic box. A sinusoidal Gaussian pulse is used to excite the broadband simulation. The absorbing boundary conditions were 7 layers of UPML. In the direction of the main radiation, 10 layers of UPML were used. Different grid resolutions starting with 2 computational cells for the height of the dielectric are used to show the convergence to the resonant frequency.

Figure 7.4 shows the return loss at the voltage source. In addition to the measured resonance frequency, a very fine reference FDTD simulation served as the numerical reference. The  $E$  field singularity enhanced FDTD scheme clearly predicts the measured and fine staircase solutions even on the coarsest grid with only 2 computational cells in the gap of the patch. Therefore, the field singularity subcell model outperforms the conventional FDTD simulation with respect

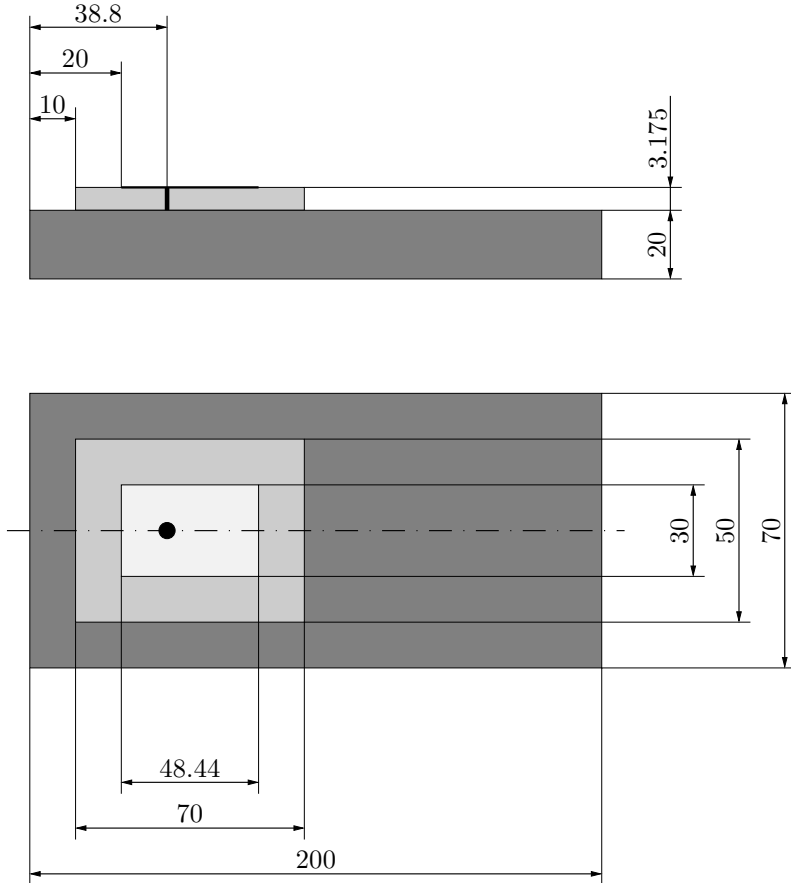


Figure 7.3: Model of a patch antenna. The unit of the numbers is mm. The light gray part is the substrate and the only dielectric material in the model. The voltage source is indicated by the bold line and circle.

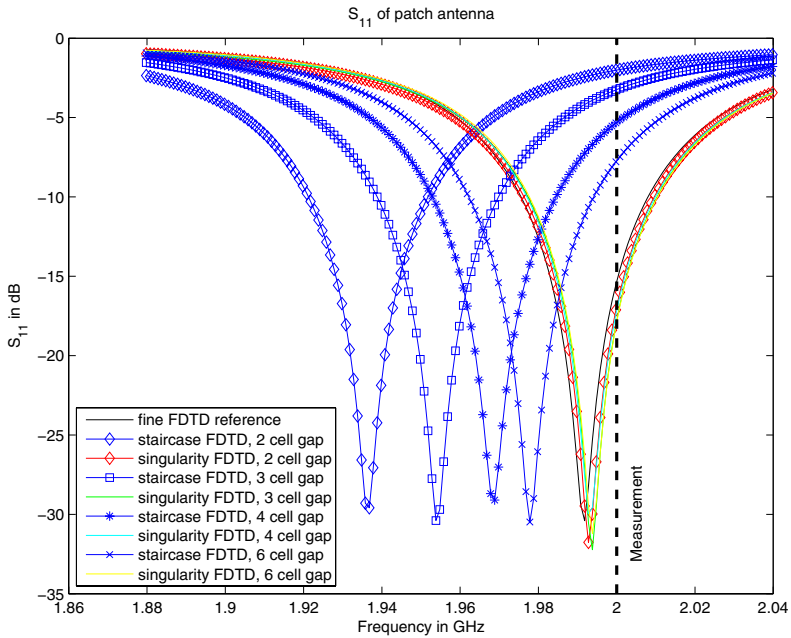


Figure 7.4: Return loss of a patch antenna on different grids with and without singularity model. The fine FDTD solution and the coarse subcell enhanced simulation accurately predict the measured value.

to accuracy and memory or CPU requirements. Because the conventional update equation could be reused, no additional memory nor computational overhead is needed to use the subcell model.

## Chapter 8

# Subcell Model Enhanced ADI-FDTD Algorithm

### 8.1 Abstract

In this chapter, a new versatile concept to integrate subcell models into the three-dimensional alternating direction implicit finite-difference time-domain (ADI-FDTD) method is introduced. The subcell enhanced ADI-FDTD scheme (S-ADI-FDTD,  $S$  refers to subcell) is formulated with the same updating equations as the conventional ADI-FDTD method, but the update coefficients are enhanced with the *a priori* knowledge of the applied subcell model. Therefore, the adaption of a conventional ADI-FDTD code to the proposed S-ADI-FDTD algorithm implies only changes in the calculation of the update coefficients. The time update procedure remains completely unmodified. The new S-ADI-FDTD method is also unconditionally stable and has no additional memory consumption nor an impact on the simulation time. Therefore and because of the increased accuracy, the proposed S-ADI-FDTD scheme should always be favored over the conventional ADI-FDTD method.

The versatile concept is demonstrated on three sample subcell models, but the procedure can be applied to a broad range of existing or new subcell models. Starting with a conformal dielectric model

based on effective material parameters, the concept is successfully applied to a field singularity subcell model and a conformal metal model. Numerical benchmarks demonstrate the benefits of the S-ADI-FDTD method over the conventional ADI-FDTD scheme.

## 8.2 Method

The proposed versatile concept for incorporating subcell models into the ADI-FDTD method enhances the conventional ADI-FDTD updating coefficients but keeps the conventional time updating procedure. Therefore, the description of the method is organized firstly by explaining the connection between the conventional FDTD coefficients and the ADI-FDTD coefficients and secondly by the modifications to the FDTD coefficient functions due to the subcell model enhancements for three typical examples.

### 8.2.1 ADI-FDTD Coefficients Based on FDTD Coefficients

In summary of section 3.4.2, the key point of the well-known ADI-FDTD derivation is that both ADI-FDTD equations (3.11) and (3.12) use the same coefficient functions  $\alpha_E$ ,  $\alpha_H$ ,  $\beta_E$ , and  $\beta_H$  as used during the original Yee update (3.3). Therefore, the final ADI-FDTD update coefficients are expressed in terms of the conventional FDTD coefficient functions  $\alpha_E$ ,  $\alpha_H$ ,  $\beta_E$ , and  $\beta_H$ . Hence, the subcell model enhanced ADI-FDTD scheme presented in this chapter is formulated with the help of the enhanced coefficient functions  $\alpha_E$ ,  $\alpha_H$ ,  $\beta_E$ , and  $\beta_H$ .

### 8.2.2 Stability

So far, there has been no published analytical proof of the unconditional stability of the ADI-FDTD method applied to a non-uniform grid including a heterogeneous material distribution. However the method is considered and has been shown experimentally to be unconditionally stable in this case.

The proposed subcell modeling method modifies only the update coefficients of the spatial integration scheme and, therefore, is incorporated into the spatial discretization of the ADI-FDTD method as modified material parameters. Hence, the proposed S-ADI-FDTD method retains the same unconditional stability as the ADI-FDTD method, which has been verified experimentally.

## 8.3 Subcell Methods

The last section summarized the formulation of the ADI-FDTD algorithm with the FDTD update coefficient functions. This section outlines the new versatile concept of subcell enhanced update coefficient functions. Starting with a conformal dielectric model based on effective material parameters, the flexibility of the approach is demonstrated on a conformal perfectly electric conductor (PEC) model. Furthermore, in the section on the conformal PEC model, a useful procedure to rewrite subcell models with the update coefficient functions is explained in detail. This procedure is reapplied on an edge field singularity subcell model to show its general usability. Finally, the introduced versatile approach is summarized.

### 8.3.1 Conformal Dielectric Model

The simplest kind of subcell model and the first presented in this chapter is a conformal dielectric model based on effective material parameters, e.g., [6]. Because effective material parameters are simply conformally enhanced permittivities, conductivities and permeabilities taking into account the local geometrical details, the FDTD coefficient functions  $\alpha_E$ ,  $\alpha_H$ ,  $\beta_E$ , and  $\beta_H$  are calculated with these modified material parameters instead of the staircase material properties.

Therefore, each dielectric subcell model presented in chapter 6 can be used to adapt to the ADI-FDTD method.

Using the procedure in section 8.2 with the coefficient functions evaluated with the effective material parameters, the adaption to the ADI-FDTD method is straightforward.

### 8.3.2 Conformal PEC Model

The next presented subcell model conformally resolves curved metallic objects based on the contour path approach. The conformal PEC technique introduced in chapter 5 will be used to adapt to the ADI-FDTD scheme. As already pointed out, a major advantage is the formulation in terms of modified coefficient functions instead of altering the update equation itself. Therefore, this novel method fits perfectly into the generalized subcell modeling ADI-FDTD approach of this thesis.

Again, the conformally modified update coefficient functions  $\tilde{\beta}_H$  and  $\tilde{\beta}_E$  serve as the basis for the adaption to the ADI-FDTD algorithm (section 8.2).

### 8.3.3 Edge Singularity Model

The last subcell model example incorporates the field singularities near sharp edges of material discontinuities. In the close vicinity of sharp edges of metal structures the electromagnetic field behaves like a quasistatic field. Knowledge about these quasistatic fields have been successfully incorporated into the FDTD method [6, 70, 75, 76]. Most methods can be transformed into the conventional update equation with a procedure similar to the one described in section 5.3.1.

As an example, the incorporation of the  $E$  field singularity of a thin metal sheet into the ADI-FDTD scheme is used here based on the formulation found in chapter 7.

Using the field singularity enhanced update coefficient function  $\tilde{\beta}_E$ , the corresponding field singularity subcell model for the ADI-FDTD method is again derived with the procedure in section 8.2.

### 8.3.4 Versatile Concept for Subcell Modeling

The last three sections have demonstrated the versatility of adapting existing FDTD subcell models to the ADI-FDTD method. Using the fact depicted in Figure 5.2 and procedure described in section 5.3.1, many of the existing subcell models can be reformulated with the standard FDTD update equation. Therefore, the procedure of section 8.2.1 can be used to benefit from these subcell models within the

ADI-FDTD method.

The adaption of the subcell models to the ADI-FDTD scheme implies only minor changes of the conventional ADI-FDTD algorithm, because only the update coefficient calculation needs modification. The generation of the tridiagonal system and performance of the subiterations remain unchanged.

## 8.4 Numerical Results

The effectiveness of the subcell models in terms of computational efficiency and memory consumption for a certain accuracy has been demonstrated in the context of the FDTD method in many publications, e.g., [6, 61, 70, 96]. Therefore, only a few selected benchmarks are presented in this chapter showing their benefits within the context of the ADI-FDTD method. The first two benchmarks show the benefits of the conformal enhancements of sections 8.3.1 and 8.3.2. The third benchmark consists of a thin metal sheet demonstrating the improvements of the singularity model of section 8.3.3. The S-ADI-FDTD implementation was carried out within the simulation platform [2] enabling user-friendly modeling and post processing.

### 8.4.1 Mie Scattering

To outline the effect of the conformal subcell model and the enlargement of the time step on the accuracy, the near field of a metal sphere was investigated to show the improvements of the conformal method. The total field, scattered field technique [6] adapted to ADI-FDTD was used to irradiate the sphere by an incident plane wave. Mie series served as the analytical reference solution. The boundary was terminated with 10 layers of UPML similar to [86]. The simulation was performed at 100 MHz with a uniform grid resolution of 8 mm, which gives overdiscretized 375 grid points per wavelength. The radius of the sphere was two computational cells, whereas the near field region covered 14-by-14-by-14 cells around the sphere's center<sup>1</sup>. The discrete norm  $L_2^h$  (square root of the mean value of squared differences) was used to compare the simulated  $E$  field to the analytical solution.

---

<sup>1</sup>Tests with other sizes revealed the qualitatively same error curves.

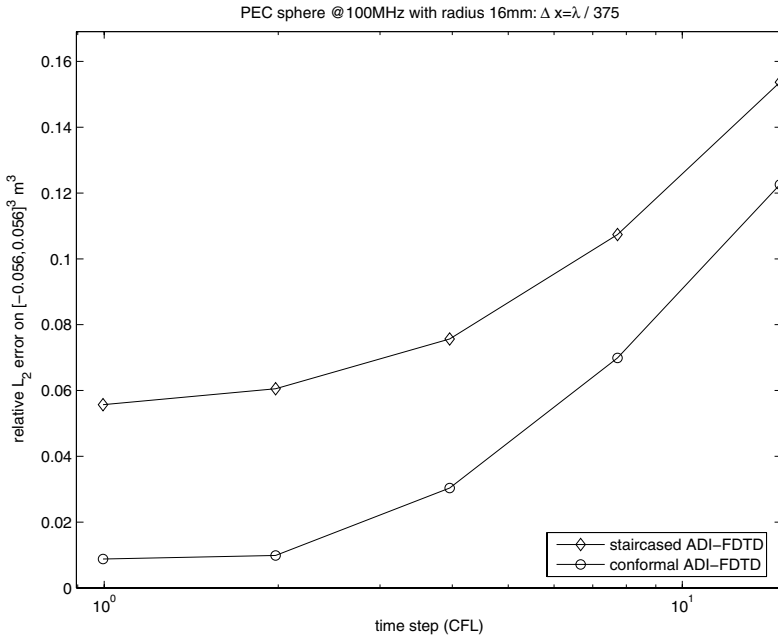


Figure 8.1: Canonical benchmark: scattering at a PEC sphere. The relative  $L_2^h$  error of the numerical near field to the analytical Mie solution is plotted.

Figure 8.1 depicts the relative norms of the errors of ADI-FDTD and conformal ADI-FDTD methods. With the conventional FDTD time step ( $\text{CFL} = 1$ ), the accuracy of the two ADI algorithms recovers the accuracy of the FDTD and conformal FDTD methods (not shown). As expected, the accuracy of the conformal and staircase ADI-FDTD methods slightly suffer while increasing the time step above the FDTD time step limit  $\text{CFL} > 1$ . However, the conformal ADI-FDTD method is always more accurate than the conventional ADI-FDTD scheme, because the conformal method benefits the most from geometrical details.

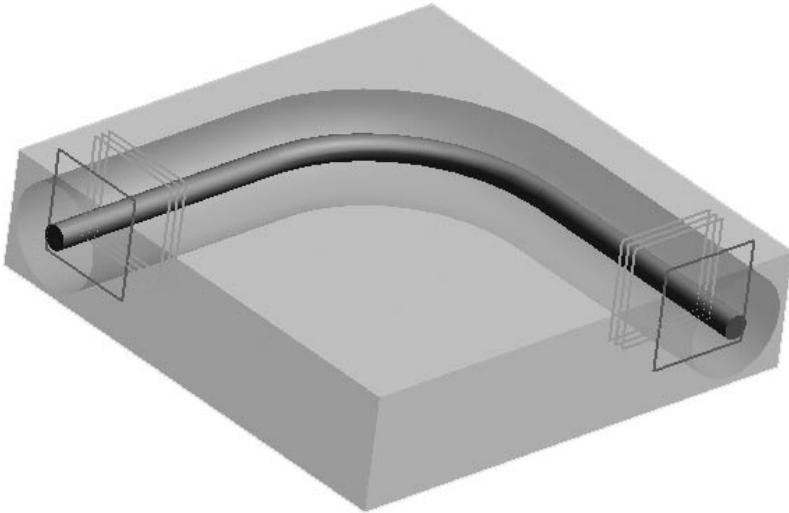


Figure 8.2: Model of the bent coaxial cable.

### 8.4.2 Bent Coaxial Cable

To increase the model's complexity and to show the accuracy gain using the conformal methods even for large CFL numbers, a bent coaxial cable was chosen. The outer and inner radii of the cable are 0.1435 mm and 0.6 mm, respectively. The relative permittivity of the dielectric is 2.7. The coaxial cable is bent 90 degrees with a radius of 2 mm of the coaxial center line. The non-uniform grid resolves the inner and outer radii with 4 and 13 cells, respectively. The two open boundaries are terminated with a 10 layered UPML absorbing boundary. Figure 8.2 shows the model in the graphical user interface of the simulation platform.

Figure 8.3 shows the return loss  $S_{11}$  for the four different solvers FDTD, conformal FDTD, ADI-FDTD, conformal ADI-FDTD. The conformal techniques outperform the conventional staircase techniques by orders in terms of accuracy. Comparing the two conformal schemes reveals that the conformal ADI-FDTD method requires less than 17 times fewer time steps to complete the simulation. The immediate

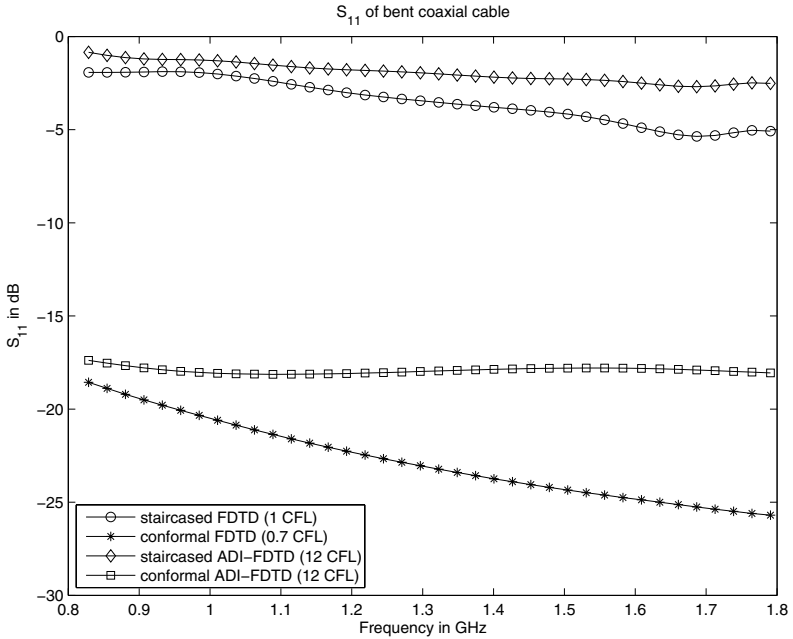


Figure 8.3: Return loss  $S_{11}$  of the bent coaxial cable. The lower the reflection, the better is the accuracy. The conformal subcell technique outperforms the staircase meshing technique.

benefit of the conformal ADI-FDTD scheme proposed in this chapter therefore becomes obvious.

### 8.4.3 Patch Antenna

Whereas sections 8.4.1 and 8.4.2 showed the benefits of conformal subcell modeling, this section demonstrates the improvements of the field singularity model of section 8.3.3. Therefore, the patch antenna of section 7.3 and depicted in Figure 7.3 serves as the next benchmark. The simulation settings are the same except of the different solver ADI-FDTD and S-ADI-FDTD, respectively. Only the simulations on the coarsest mesh are presented in this chapter. However and in addition, the effect of an increased time step on the accuracy is studied.

Figure 8.4 shows the return loss at the voltage source. In addition to the measured resonance frequency, a very fine reference FDTD simulation served as the numerical reference. Using the conventional FDTD time step  $CFL = 1$ , the ADI-FDTD simulation with the singularity model outperforms the staircase ADI-FDTD simulation. Increasing the time step by a factor of three ( $CFL = 3$ ) results for the singularity enhanced ADI-FDTD simulation in the same accuracy as the conventional ADI-FDTD simulation with  $CFL = 1$ . In contrast, the accuracy of the staircase ADI-FDTD simulation with  $CFL = 3$  decreases. Therefore, the singularity model ADI-FDTD simulation needs only a third of the simulation time of the staircase ADI-FDTD simulation for the same accuracy.

## 8.5 Conclusion

In this chapter a new versatile concept for integrating subcell models into a 3-D ADI-FDTD solver was introduced. The key feature was the formulation with the standard ADI-FDTD update coefficients, which were enhanced with FDTD subcell model knowledge. A versatile strategy to incorporate an existing FDTD subcell model into the conventional FDTD equation was explained in detail. These two key features render the new S-ADI-FDTD method applicable and advantageous to a wide range of applications. The presented ADI-FDTD

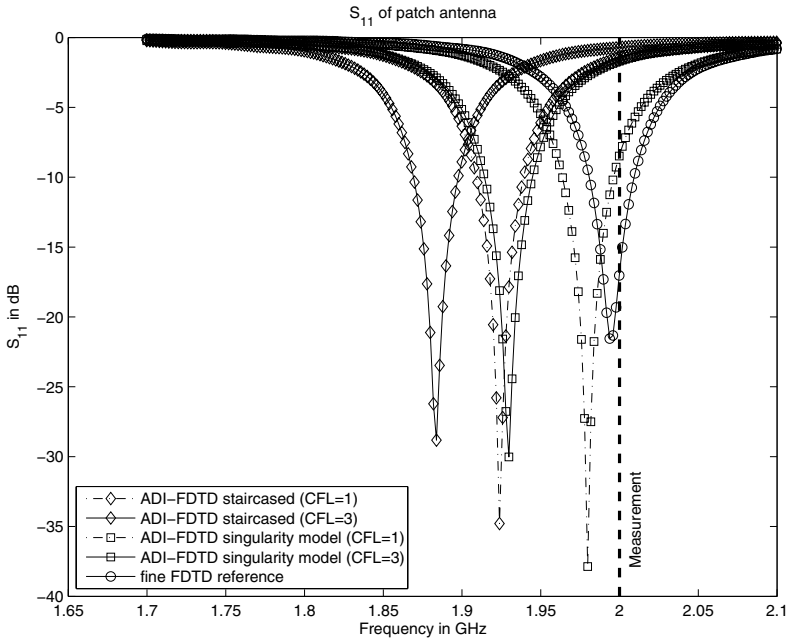


Figure 8.4: Return loss of a patch antenna on the same grid, with  $\text{CFL} \in \{1, 3\}$  and with/without singularity model. The fine FDTD solution accurately predicts the measured value.

subcell models and their applications included a conformal dielectric and PEC model and a field singularity subcell model near edges of thin metal sheets. Implemented within the simulation platform [2], the numerical benchmarks showed the accuracy benefit of the subcell enhanced ADI-FDTD solver over the staircase ADI-FDTD simulations. In addition, no additional memory nor simulation time is required for the subcell model enhanced ADI-FDTD algorithm compared to the conventional ADI-FDTD method. Therefore, the proposed subcell enhanced ADI-FDTD method should always be favored over the ADI-FDTD scheme.



# Chapter 9

## ADI-FDTD Benchmark: NOKIA 8310

### 9.1 Introduction

The objective of this benchmark was to replicate with the ADI-FDTD solver a previous joint study carried out with the Nokia Research Center (NRC, Finland) aimed at evaluating to which degree FDTD is capable of accurately simulating an entire CAD derived model (IGES) of the NOKIA 8310. An important aspect of this study concerns the near-field analysis in which  $E$ -fields (dB normalized to maximum) are compared for the DCS1800 band in two horizontal planes located at 3 mm from either side of the phone. Figure 9.1 shows the CAD model and the discretized model of the mobile phone. The mesh is truncated by 8 layers of UPML media leading to an overall mesh size of 5.6 million computational cells, whose size varies between 0.01 mm and 12 mm. More than 500 CAD parts describe the mobile phone's geometry. A voltage source is used as the excitation model [84].

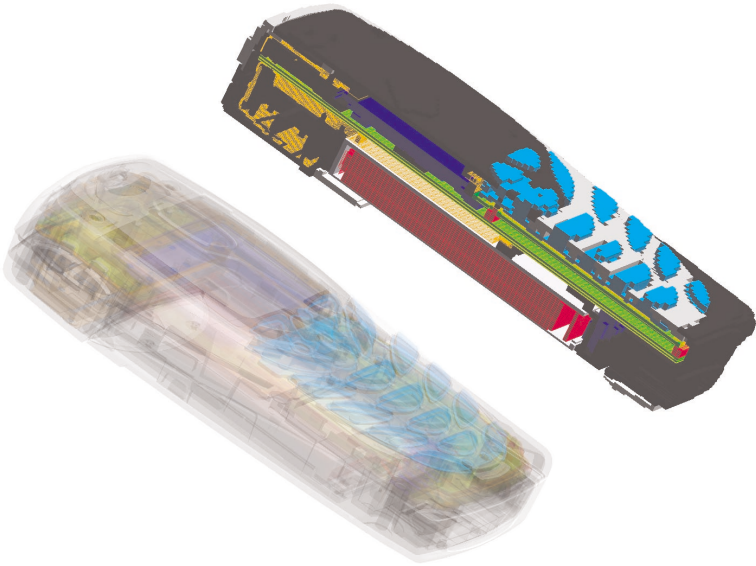


Figure 9.1: CAD model and discretized model of the NOKIA 8310. The CAD model consists of 526 distinguished parts.

## 9.2 Simulation Results

Comparisons between ADI-FDTD simulations and the FDTD reference simulation are based on  $E$  field modules and are characterized by their deviation  $dev$  calculated by

$$dev := \frac{\|\vec{E}_{rms}^{ADI-FDTD} - \vec{E}_{rms}^{FDTD}\|}{\|\vec{E}_{rms}^{FDTD}\|}. \quad (9.1)$$

ADI-FDTD simulations have been run for different time steps and are compared with their corresponding FDTD simulation (used as the reference simulation). The time steps of the ADI-FDTD simulations are specified as multiples of the conventional FDTD time step, i.e., the CFL criteria. All excitations are harmonic, and all fields are extracted in the frequency domain.

Both the ADI-FDTD and FDTD simulations (Figure 9.2) show that the energy is radiated mostly out of the back of the phone through the high  $E$ -fields located above the antenna. This is desirable because the energy is thus directed away from the user, as intended with the use of an integrated patch-type antenna.

In Figure 9.3 the deviations  $dev$  of the ADI-FDTD simulations compared to the FDTD reference are plotted versus the CFL number. With increased CFL number the accuracy of the  $E$  field is slightly diminished. Therefore and depending on the desired accuracy, the simulation time can be drastically reduced using the ADI-FDTD method.

## 9.3 Conclusion

The deviations between the FDTD reference simulation and the ADI-FDTD simulations are small up to a time step of 32 CFL. This benchmark shows not only that ADI-FDTD is as robust as FDTD for complex simulations but also that it is significantly more efficient for this benchmark.

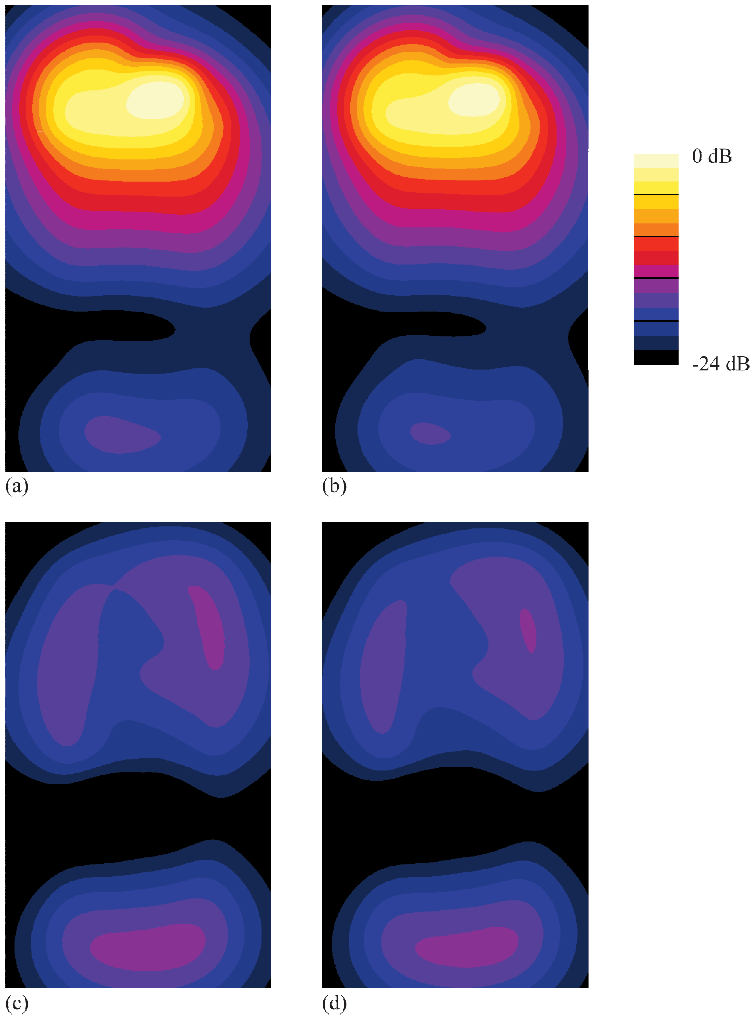


Figure 9.2: (a) and (b) show the  $|\vec{E}|_{\text{rms}}$  of the back plane of the FDTD (a) and ADI-FDTD (b) simulations. Below the radiation pattern of the front plane is presented: FDTD (c) and ADI-FDTD (d) schemes. Good agreement between the ADI-FDTD simulation with  $\text{CFL} = 32$  and the FDTD reference is obtained.

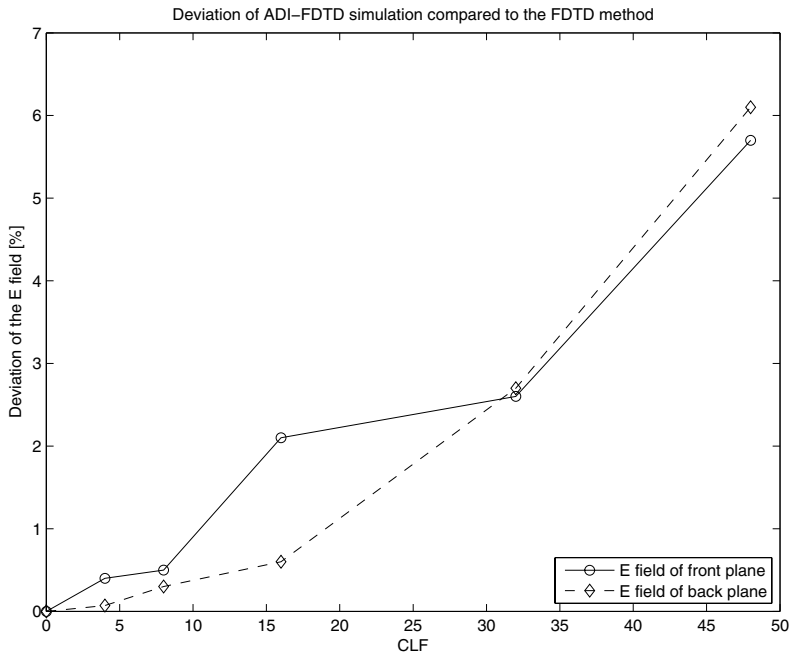


Figure 9.3: Deviations of the  $E$  field calculated with the ADI-FDTD method with increasing time step (CFL) compared to the conventional Yee FDTD simulation.



**Part III**

**Conclusions**



## Chapter 10

# Conclusion and Outlook

Summing up the range of results and scientific contributions achieved performed within the presented PhD thesis, all objectives listed in section 1.1 have been thoroughly fulfilled. A set of novel algorithms has been theoretically derived, developed and subsequently implemented into the commercial simulation platform SEMCAD X. The CTI supported project TRINITY, in strong cooperation with IT'IS, IIS and SPEAG allowed the research and implementation performed in this thesis. SEMCAD X has proven to be an excellent basis for implementation, testing and finally releasing and exposing the work to end-customers. In particular, the novel conformal discretization scheme has been heavily used by SEMCAD X customers on a daily basis since April 2005. The fast algorithm has proven to be robust even for thousands of distinguished CAD parts on grid sizes up to a billion cells.

The consequent reformulation of the subcell algorithm with conventional but modified FDTD update coefficients was the key point for the derivation of a stability criterion for all subcell models. In the case of the conformal PEC subcell model, the stability formula was inverted to provide the user with the possibility to favor either a short simulation time or geometrically detailed resolution of the curved material interface. This unique and new feature is the basis of the robust and versatile conformal PEC model and a necessary requirement for conformal real-world simulations.

Moreover, reformulation with the conventional FDTD update coef-

ficients enabled use of the hardware acceleration card even for subcell models. Therefore, the novel proposed subcell models can profit from the tremendous acceleration of electromagnetic (EM) simulations using the graphics card. Furthermore and because of the heavily reduced simulation time and the robust discretization scheme, optimizations using genetic algorithms with dozens of parameters can be performed with the subcell enhanced EM solver.

If no hardware acceleration option is available, implicit time integration schemes can be used to overcome the time step limitation for electrically highly overdiscretized simulation scenarios. The introduced pioneering concept to incorporate subcell models into the ADI-FDTD scheme has the same memory and CPU requirements as the conventional method. Therefore, ADI-FDTD schemes can also benefit from the *a priori* known local field behavior, and the new subcell technique enhanced ADI-FDTD solver should thus be favored over the standard ADI-FDTD method.

Looking back to the beginning of this thesis in 2002, major pioneering work has been performed towards the improvement of FDTD and simulation of CAD derived structures. Within IT<sup>2</sup>IS research group focusing on mobile devices, simulations of CAD based phones consisting of hundreds of parts, featuring resolutions down to 100 microns could be performed in about one day with a grid size of 5 million cells. Today it is possible to analyze structures with thousands of distinguished CAD parts and resolutions smaller than 50 microns in less than 10 minutes (20 million cells). It has mainly been the contributions performed within the framework of this thesis or within our research group — related to the subcell modeling technique, robust discretization of the model, ADI-FDTD method, hardware acceleration and graphics processing — which have made this possible. Furthermore, our contributions have allowed the extension of extend the FDTD method to the medical and automotive fields, requiring much larger computational resources but still delivering solutions within an appropriate amount of time. Features also enable companies to perform so-called ‘virtual prototyping’, i.e., the assessment of possible device deficiencies due to manufacturing tolerances at an early stage. In addition, subparts of the ‘virtual prototype’ can be optimized according to the specifications.

Future research following this thesis’ outcome will include:

- The general concept of incorporating the *a priori* known local field behavior can be applied to every numerical scheme using the same spatial discretization as the Yee scheme, e.g., the Crank-Nicolson scheme, frequency domain solvers based on a staggered rectilinear grid, etc.
- The conformal PEC scheme can be applied to thin PEC sheets, splitting a computational cell into ‘left’ and ‘right’ parts and then using the proposed scheme on each part.
- The subcell model technique will be extended to other local and *a priori* known field behaviors and reformulated within the conventional FDTD update equation. Stefan Schild is currently developing a subcell model for the treatment of thin conductive sheets.

Based on current trends, optimization of even complex virtual prototypes will become possible in the future. Optics is becoming more and more interested in accurately modeling the three-dimensional field behavior of optical waveguides, for which the conformal FDTD method with hardware acceleration is a promising simulation software candidate. In the medical sector, thermal ablation treatment will be optimized using FDTD simulations based on individual patient MRI data. My PhD colleague Esra Neufeld is conducting his research in this area. Furthermore, there are trends toward combining numerical and measured electromagnetic compliance tests to obtain more detailed insight.

The follow-up CTI project HYCUNET addresses the upcoming challenges of the widening variety of applications of electromagnetic simulations using the FDTD method.



# Appendix A

## List of Acronyms

ABC	Absorbing Boundary Condition
ADI	Alternating Direction Implicit
BIOEM	Bioelectromagnetics
CAD	Computer Aided Design
C-FDTD	Conformal Finite-Difference Time-Domain
CFL	Courant-Friedrichs-Lewy
CP-FDTD	Contour Path Finite-Difference Time-Domain
COM	Complementary Operators Method
CSCIENCE	Compliance Science
DASY	Dosimetric Assessment System
DCS	Digital Communications System
ETH	Eidgenössische Technische Hochschule
EM	Electromagnetic
EMC	Electromagnetic Compatibility
EMI	Electromagnetic Interference
FDTD	Finite-Difference Time-Domain
FEM	Finite Element Method
FETD	Finite Element Time-Domain
FIT	Finite Integration Technique

FVTD	Finite-Volume Time-Domain
GB	Gigabyte
GHz	Gigahertz
GMT	Generalized Multipole Technique
GSM	Global System for Mobile Communications
IEEE	Institute of Electrical and Electronics Engineers
IIS	Institut für Integrierte Systeme
ISE	Integrated Systems Engineering AG
IT'IS	Foundation for Research on Information Technologies in Society
KTI/CTI	Kommission für Technologie und Innovation
MoM	Method of Moments
P4	Pentium 4
PEC	Perfectly Electric Conductor
PMC	Perfectly Magnetic Conductor
PML	Perfectly Matched Layer
RAM	Random Access Memory
RF	Radio Frequency
RMS	Root Mean Square
S-ADI-FDTD	Subcell enhanced ADI-FDTD
SAM	Specific Anthropomorphic Mannequin
SAR	Specific Absorption Rate
SEMCAD	Simulation Platform for Electromagnetic Compatibility Antenna Design and Dosimetry
SPEAG	Schmid & Partner Engineering AG
TCAD	Technical Computer Aided Design
TFSF	Total-Field Scattered-Field
TLM	Transmission Line Method

# Appendix B

## List of Symbols

$\vec{A}$	Surface with area $ \vec{A} $ and normal $\vec{A}/ \vec{A} $ [ $m^2$ ]
$A^{\text{ratio}}$	Fraction of area on a Yee cube face belonging to $XY$ material [1]
$\vec{B}$	Magnetic flux vector [ $\frac{Vs}{m^2}$ ]
$c$	Speed of light [ $\frac{m}{s}$ ]
$c_0$	Speed of light in vacuum: 299 792 458 $\frac{m}{s}$
$\vec{D}$	Electric displacement current vector [ $\frac{As}{m^2}$ ]
$\vec{E}$	Electric field vector [ $\frac{V}{m}$ ]
$f$	Frequency [ $1/s = \text{Hz}$ ]
$\vec{H}$	Magnetic field vector [ $\frac{A}{m}$ ]
$\vec{J}$	Current density vector [ $\frac{A}{m^2}$ ]
$\vec{k}$	Wave vector [ $\frac{1}{m}$ ]
$\vec{n}$	Normal of surface [1]
$P_i$	Point $i$ of a triangle
$Q$	Charge [ $As$ ]
$\vec{\mathcal{R}}$	Curl operator $\nabla \times$ in matrix form
$\tilde{\mathcal{R}}_e$	Even part of curl matrix (ADI-FDTD)
$\tilde{\mathcal{R}}_o$	Odd part of curl matrix (ADI-FDTD)
$\vec{s}$	Distance vector [ $m$ ]

$s_i$	Barycentric coordinate value [1]
$t$	Time [s]
$V$	Volume [ $m^3$ ]
$\vec{x}$	Vector in space [ $m$ ]
$x$	Cartesian vector component $x$ [ $m$ ]
$y$	Cartesian vector component $y$ [ $m$ ]
$z$	Cartesian vector component $z$ [ $m$ ]
$\alpha_E$	Function for FDTD $E$ update coefficient in front of the $E$ field
$\alpha_H$	Function for FDTD $H$ update coefficient in front of the $H$ field
$\beta_E$	Function for FDTD $E$ update coefficient in front of the curl of the $H$ field
$\beta_H$	Function for FDTD $H$ update coefficient in front of the curl of the $E$ field
$\Delta i$	Distance between two grid lines on axis $i \in \{x, y, z\}$ [ $m$ ]
$\Delta i^p$	Distance between two grid lines on the primary axis $i \in \{x, y, z\}$ [ $m$ ]
$\Delta i^s$	Distance between two grid lines on the secondary axis $i \in \{x, y, z\}$ [ $m$ ]
$\Delta^{\text{ratio}}$	Fraction of edge length belonging to $XY$ material [1]
$\Delta t$	Time step [s]
$\epsilon$	Electric permittivity [ $\frac{As}{Vm}$ ]
$\epsilon_0$	Electric permittivity of vacuum: $\frac{1}{c_0^2 \mu_0} \approx 8.8542 \cdot 10^{-12} \frac{As}{Vm}$
$\epsilon_r$	Relative electric permittivity $\epsilon/\epsilon_0$ [1]
$\lambda$	Wavelength [ $m$ ]
$\mu$	Magnetic permeability [ $\frac{Vs}{Am}$ ]
$\mu_0$	Magnetic permeability of vacuum: $4\pi \cdot 10^{-7} \frac{Vs}{Vm} \approx 1.2566 \cdot 10^{-6} \frac{Vs}{Vm}$
$\mu_r$	Relative magnetic permeability $\mu/\mu_0$ [1]
$\nabla$	Nabla operator $(\partial/\partial x, \partial/\partial y, \partial/\partial z)^T$
$\nu$	Frequency [ $1/s = \text{Hz}$ ]

- $\omega$  Angular frequency *rad/s*  
 $\rho$  Charge density [ $\frac{As}{m^3}$ ]  
 $\sigma$  Electric conductivity [ $\frac{A}{Vm} = \frac{1}{\Omega m}$ ]



# Appendix C

## Publications

### C.1 Journal Publications Included in this Thesis

Within the framework of this thesis, the following scientific journal contributions have been written by the author.

1. S. Benkler, N. Chavannes, and N. Kuster, “A new 3-D conformal PEC FDTD scheme with user-defined geometric precision and derived stability criterion,” *IEEE Transactions on Antennas and Propagation*, vol. 54, no. 6, pp. 1843–1849, June 2006.
2. S. Benkler, N. Chavannes, and N. Kuster, “Mastering conformal meshing for complex CAD based C-FDTD simulations,” *IEEE Antennas and Propagation Magazine*, 2006 submitted.
3. S. Benkler, N. Chavannes, and N. Kuster, “Versatile approach of incorporating subcell models into the 3-D ADI-FDTD method,” *IEEE Transactions on Antennas and Propagation*, 2006 submitted.

## C.2 Other Journal Publications

In addition, the author of this thesis has co-authored the following journal publication.

4. A. Christ, S. Benkler, J. Fröhlich, and N. Kuster, “Analysis of the accuracy of the numerical reflection coefficient of the finite-difference time-domain method at planar material interfaces,” *IEEE Transactions on Electromagnetic Compatibility*, vol. 48, no. 2, pp. 264–272, May 2006.

## C.3 Other Publications

Furthermore, the author has presented and co-authored various other publications.

5. S. Benkler, N. Chavannes, J. Fröhlich, H. Songoro, and N. Kuster, “Accurate representation of complex 3—D geometries for conformal FDTD simulations including solids and thin sheets,” in *2004 AP-S/URSI International Symposium*, Monterey, California, June 2004, p. 254.
6. S. Benkler, H. Songoro, N. Chavannes, and N. Kuster, “Robust and fully automated conformal mesh generation for complex conformal FDTD applications,” in *2005 IEEE AP-S/URSI International Symposium and USNC/URSI National Radio Science Meeting*, Washington DC, USA, July 2005, poster, 3–8 July.
7. H. Songoro, S. Benkler, N. Chavannes, and N. Kuster, “On the real world performance of ADI-FDTD,” in *2005 IEEE AP-S/URSI International Symposium and USNC/URSI National Radio Science Meeting*, Washington DC, USA, July 2005, poster, 3–8 July.
8. S. Benkler, H. Songoro, N. Chavannes, and N. Kuster, “Automated and robust conformal mesher for complex conformal FDTD applications,” in *Progress In Electromagnetics Research Symposium (PIERS)*, vol. Abstracts. Hangzhou, China: The

Electromagnetics Academy, MA, August 2005, p. 170, session 2P5b: FDTD.

9. H. Songoro, S. Benkler, N. Chavannes, and P. Futter, “The real-world performance of staircased and conformal ADI-FDTD,” in *Progress in Electromagnetics Research Symposium (PIERS)*, vol. Abstracts. Hangzhou, China: The Electromagnetics Academy, August 2005, p. 165, session 2P5b: FDTD.
10. S. Benkler, N. Chavannes, and N. Kuster, “New conformal PEC FDTD model with user-defined geometric precision and derived stability criterion,” in *28th Annual Meeting of the Bioelectromagnetics Society*, Cancun, Mexico, June 2006, pp. 147–148, pA-141 in Poster Session A, (12 June).
11. S. Benkler, N. Chavannes, and N. Kuster, “Three-dimensional conformal alternating direction implicit finite-difference time-domain solver (C-ADI-FDTD),” in *28th Annual Meeting of the Bioelectromagnetics Society*, Cancun, Mexico, June 2006, pp. 363–364, pB-142 in Poster Session B, (13 June).
12. S. Benkler, N. Chavannes, and N. Kuster, “New conformal PEC FDTD model with user-defined geometric precision and derived stability criterion,” in *Final Program of the 2006 IEEE Antennas and Propagation Society International Symposium with USNC/URSI National Radio Science Meeting*, Albuquerque, NM USA, July 2006, p. 508, July 12, Poster # 381.7 in Session 381: Posters Different EQ Methods: Advances in FDTD (URSI).
13. S. Benkler, N. Chavannes, and N. Kuster, “Three-dimensional conformal alternating direction implicit finite-difference time-domain solver (C-ADI-FDTD),” in *Final Program of the 2006 IEEE Antennas and Propagation Society International Symposium with USNC/URSI National Radio Science Meeting*, Albuquerque, NM USA, July 2006, p. 507, July 12, Poster # 381.6 in Session 381: Posters Different EQ Methods: Advances in FDTD (URSI).
14. S. Benkler, “Dielectric sub-cell models,” IT’IS Foundation for Research on Information Technologies in Society, 8004 Zürich, Switzerland, Tech. Rep., April 2004.

15. S. Benkler and J. Fröhlich, “Behaviour of electromagnetic fields at lossy material boundaries,” IT’IS Foundation for Research on Information Technologies in Society, 8004 Zürich, Switzerland, Tech. Rep., August, 2003.

# Bibliography

- [1] K. S. Yee. Numerical solution of initial boundary value problems involving Maxwell's equations in isotropic media. *IEEE Transactions on Antennas and Propagation*, 14(3):302–307, March 1966.
- [2] SEMCAD X. Reference manual for the SEMCAD X simulation platform for electromagnetic compatibility, antenna design and dosimetry. *SPEAG - Schmid & Partner Engineering AG*, Version 11.0, MOENCH, 07 2006.
- [3] J. D. Jackson. *Classical Electrodynamics*. John Wiley & Sons, Inc., third edition, 1998.
- [4] Ch. Hafner. *Numerische Berechnung elektromagnetischer Felder: Grundlagen, Methoden, Anwendungen*. Springer Verlag, 1987.
- [5] Todd H. Hubing. Survey of numerical electromagnetic modeling techniques. Technical Report TR91-1-001.3, Electromagnetic Compatibility Laboratory, University of Missouri-Rolla, September 1991.
- [6] A. Taflov and S. Hagness. *Computational Electrodynamics: The Finite-Difference Time-Domain Method*, 3 ed. Artech House, Boston, MA, 2005.
- [7] T. Weiland. A discretization method for the solution of Maxwell's equations for six-component fields. *Electronics and Communications AEÜ*, 31(3):116–120, 1977.

- [8] M. Clemens and T. Weiland. Discrete electromagnetism with the finite integration technique. In *Progress in Electromagnetic Research (PIER)*, volume 32, pages 65–87. 2001.
- [9] M. Krumpholz, C. Huber, and P. Russer. A field theoretical comparison of FDTD and TLM. *IEEE Transactions on Microwave Theory and Techniques*, 43(8):1935–1950, August 1995.
- [10] U. Andersson. *Time-Domain Methods for the Maxwell Equations*. PhD thesis, Royal Institute of Technology, Stockholm, 2001.
- [11] Peter Monk. An analysis of Nédélec method for the spatial discretization of Maxwell’s equation. *Journal of Computational and Applied Mathematics*, 47:101–121, 1993.
- [12] J. C. Nédélec. Mixed finite elements in  $R^3$ . *Numerische Mathematik*, 35:315–341, 1980.
- [13] A. Bossavit and L. Kettunen. Yee-like schemes on a tetrahedral mesh, with diagonal lumping. *International Journal of Numerical Modelling*, 12(1–2):129–142, 1999.
- [14] F. L. Teixeira and W. C. Chew. Lattice electromagnetic theory from a topological viewpoint. *Journal of Mathematical Physics*, 40(1):169–187, 1999.
- [15] A. Bossavit, L. Kettunen, and T. Tarhassaari. Some realizations of a discrete Hodge operator: A reinterpretation of the finite element technique. *IEEE Transactions on Magnetics*, 35:1494–1497, May 1999.
- [16] A. Bossavit and L. Kettunen. Yee-like schemes on staggered cellular grids: A synthesis between FIT and FEM approaches. *IEEE Transactions on Magnetics*, 36(4):861–867, July 2000.
- [17] P. Bonnet, X. Ferrieres, B. L. Michielsen, P. Klotz, and J. L. Roumiguères. Finite-volume time domain method. In S. M. Rao, editor, *Time Domain Electromagnetics*, pages 307–367. Academic Press, 1997.

- [18] Dirk Baumann. *A 3-D Numerical Field Solver Based on the Finite-Volume Time-Domain Method*. PhD thesis, Swiss Federal Institute of Technology (ETH), Zürich, Switzerland, 2006.
- [19] C. Fumeaux, D. Baumann, P. Leuchtman, and R. Vahldieck. A generalized local time-step scheme for efficient FVTD simulations in strongly inhomogeneous meshes. *IEEE Transactions on Microwave Theory and Techniques*, 52(3):1067–1076, March 2004.
- [20] R. F. Harrington. *Field Computation by Moment Methods*. The Macmillan Co., New York, 1968.
- [21] Z. D. Chen and Shuiping Luo. Generalization of the finite-difference-based time-domain methods using the method of moments. *IEEE Transactions on Antennas and Propagation*, 54(9):2515–2524, September 2006.
- [22] Tatsuo Itoh. *Numerical Techniques for Microwave and Millimeter-wave Passive Structures*. John Wiley & Sons, New York, 1989.
- [23] Ch. Hafner. *The Generalized Multipole Technique for Computational Electromagnetics*. Artech House, Boston, MA, 1990.
- [24] M. Celuch-Marcysiak and W. K. Gwarek. On the nature of solutions produced by finite difference schemes in time domain. *International Journal of Numerical Modelling: Electronic Networks, Devices and Fields*, 12(1–2):23–40, January–April 1999.
- [25] A. Christ. *Analysis and Improvement of the Numerical Properties of the FDTD Algorithm*. PhD thesis, Swiss Federal Institute of Technology (ETH), Zürich, Switzerland, 2003.
- [26] K. L. Shlager and J. B. Schneider. A selective survey of the finite-difference time-domain literature. *IEEE Antennas and Propagation Magazine*, 37(4):39–56, August 1995.
- [27] K. L. Shlager and J. B. Schneider. A survey of the finite-difference time-domain literature. In A. Taflove, editor, *Advances in Computational Electrodynamics: The Finite-*

- Difference Time-Domain Method*, chapter 1, pages 1–62. Artech House, Boston, MA, 1998.
- [28] K. L. Shlager and J. B. Schneider. FDTD.org – Finite-difference time-domain literature database. <http://www.fDTD.org>.
- [29] A. Taflove and S. Hagness. *Computational Electrodynamics: The Finite-Difference Time-Domain Method, 1 ed.* Artech House, Boston, MA, 1995.
- [30] A. Taflove and S. Hagness. *Computational Electrodynamics: The Finite-Difference Time-Domain Method, 2 ed.* Artech House, Boston, MA, 2000.
- [31] B. Denecker, L. Knockaert, F. Olyslager, and D. De Zutter. A new state-space-based algorithm to assess the stability of the finite-difference time-domain method for 3D finite inhomogeneous problems. *AEÜ International Journal of Electronics and Communications*, 58(5):339–348, 2004.
- [32] A. C. Cangellaris and D. B. Wright. Analysis of the numerical error caused by the stair-stepped approximation of a conducting boundary in FDTD simulations of electromagnetic phenomena. *IEEE Transactions on Antennas and Propagation*, 39(10):1518–1525, October 1991.
- [33] R. Holland. Pitfalls of staircase meshing. *IEEE Transactions on Electromagnetic Compatibility*, 35(4):434–439, November 1993.
- [34] J. B. Schneider and C. L. Wagner. FDTD dispersion revisited: Faster-than-light propagation. *IEEE Microwave Guided Wave Letters*, 9(2):54–56, February 1999.
- [35] P. H. Harms, J.-F. Lee, and R. Mittra. A study of the nonorthogonal FDTD method versus the conventional FDTD technique for computing resonant frequencies of cylindrical cavities. *IEEE Transactions on Microwave Theory and Techniques*, 40(4):741–746, April 1992.
- [36] P. H. Harms, J.-F. Lee, and R. Mittra. Corrections to “A study of the nonorthogonal FDTD method versus the conventional

- FDTD technique for computing resonant frequencies of cylindrical cavities". *IEEE Transactions on Microwave Theory and Techniques*, 40(11):2115–2116, November 1992.
- [37] N. K. Madsen. Divergence preserving discrete surface integral methods for Maxwell's curl equations using non-orthogonal unstructured grids. *Journal of Computational Physics*, 119:34–45, 1995.
- [38] T. I. Kosmanis and T. D. Tsiboukis. A systematic and topologically stable conformal finite-difference time-domain algorithm for modeling curved dielectric interfaces in three dimensions. *IEEE Transactions on Microwave Theory and Techniques*, 51(3):839–847, March 2003.
- [39] C. J. Railton and I. J. Craddock. Analysis of general 3-D PEC structures using improved CPFDTD algorithm. *Electronics Letters*, 31(20):1553–1554, September 1995.
- [40] T. G. Jurgens, A. Taflove, K. Umashankar, and T. G. Moore. Finite-difference time-domain modeling of curved surfaces. *IEEE Transactions on Antennas and Propagation*, 40(4):357–366, April 1992.
- [41] T. G. Jurgens and A. Taflove. Three-dimensional contour FDTD modeling of scattering from single and multiple bodies. *IEEE Transactions on Antennas and Propagation*, 41(12):1703–1708, December 1993.
- [42] Y. Hao and C. J. Railton. Analyzing electromagnetic structures with curved boundaries on cartesian FDTD meshes. *IEEE Transactions on Microwave Theory and Techniques*, 46(1):82–88, January 1998.
- [43] N. Chavannes. *Local Mesh Refinement Algorithms for Enhanced Modeling Capabilities in the FDTD Methods*. PhD thesis, Swiss Federal Institute of Technology (ETH), Zürich, Switzerland, 2002.
- [44] B. Donderici and F. L. Teixeira. Improved FDTD subgridding algorithms via digital filtering and domain overriding. *IEEE*

- Transactions on Antennas and Propagation*, 53(9):2938–2951, September 2005.
- [45] B. Donderici and F. L. Teixeira. Domain-overriding and digital filtering for 3-d fdtd subgridded simulations. *IEEE Microwave and Wireless Components Letters*, 16(1):10–12, January 2006.
- [46] J. G. Maloney and G. S. Smith. The efficient modeling of thin material sheets in the finite-difference time-domain (FDTD) method. *IEEE Transactions on Antennas and Propagation*, 40(3):323–330, March 1992.
- [47] N. Kaneda, B. Houshmand, and T. Itoh. FDTD analysis of dielectric resonators with curved surfaces. *IEEE Transactions on Microwave Theory and Techniques*, 45(9):1645–1649, September 1997.
- [48] T. Hirono, Y. Shibata, W. W. Lui, S. Seki, and Y. Yoshikuni. The second-order condition for the dielectric interface orthogonal to the Yee-lattice axis in the FDTD scheme. *IEEE Microwave Guided Wave Letters*, 10(9):359–361, September 2000.
- [49] K.-P. Hwang and A. C. Cangellaris. Effective permittivities for second-order accurate FDTD equations at dielectric interfaces. *IEEE Microwave and Wireless Components Letters*, 11(4):158–160, April 2001.
- [50] S. Dey and R. Mittra. A conformal finite-difference time-domain technique for modeling cylindrical dielectric resonators. *IEEE Transactions on Microwave Theory and Techniques*, 47(9):1737–1739, September 1999.
- [51] W. Yu, S. Dey, and R. Mittra. On the modeling of periodic structures using the finite-difference time-domain algorithm. *Microwave and Optical Technology Letters*, 24(3):151–155, 2000.
- [52] W. Yu and R. Mittra. A conformal finite difference time domain technique for modeling curved dielectric surfaces. *IEEE Microwave and Wireless Components Letters*, 11(1):25–27, January 2001.

- [53] J.-Y. Lee and N.-H. Myung. Locally tensor conformal FDTD method for modeling arbitrary dielectric surfaces. *Microwave and Optical Technology Letters*, 23(4):245–249, 1999.
- [54] J. Nadobny, D. Sullivan, W. Wlodarczyk, and P. Wust. A 3-D tensor FDTD-formulation for treatment of sloped interfaces in electrically inhomogeneous media. *IEEE Transactions on Antennas and Propagation*, 51(8):1760–1770, August 2003.
- [55] K. H. Dridi, J. S. Hesthaven, and A. Ditkowski. Staircase-free finite-difference time-domain formulation for general materials in complex geometries. *IEEE Transactions on Antennas and Propagation*, 49(5):749–756, May 2001.
- [56] A. Ditkowski, K. H. Dridi, and J. S. Hesthaven. Convergent cartesian grid methods for Maxwell’s equations in complex geometries. *Journal of Computational Physics*, 170:39–80, May 2001.
- [57] M. Fujii, D. Lukashevich, I. Sakagami, and P. Russer. Convergence of FDTD and wavelet-collocation modeling of curved dielectric interface with the effective dielectric constant technique. *IEEE Microwave and Wireless Components Letters*, 13(11):469–471, November 2003.
- [58] T. Xiao and Q. H. Liu. A staggered upwind embedded boundary (SUEB) method to eliminate the FDTD staircasing error. *IEEE Transactions on Antennas and Propagation*, 52(3):730–741, March 2004.
- [59] A. Christ, S. Benkler, J. Fröhlich, and N. Kuster. Analysis of the accuracy of the numerical reflection coefficient of the finite-difference time-domain method at planar material interfaces. *IEEE Transactions on Electromagnetic Compatibility*, 48(2):264–272, May 2006.
- [60] Ahmad Mohammadi, Hamid Nadgaran, and Mario Agio. Contour-path effective permittivities for the two-dimensional finite-difference time-domain method. *Optics Express*, 13(25):10367–10381, December 2005.

- [61] C. J. Railton and J. B. Schneider. An analytical and numerical analysis of several locally conformal FDTD schemes. *IEEE Transactions on Microwave Theory and Techniques*, 47(1):56–66, January 1999.
- [62] I. J. Craddock, C. J. Railton, and J. P. McGeehan. Derivation and application of a passive equivalent circuit for the finite difference time domain algorithm. *IEEE Microwave Guided Wave Letters*, 6(1):40–42, January 1996.
- [63] J. Anderson, M. Okoniewski, and S. S. Stuchly. Practical 3-D contour/staircase treatment of metals in FDTD. *IEEE Microwave Guided Wave Letters*, 6(3):146–148, March 1996.
- [64] S. Dey and R. Mittra. A locally conformal finite-difference time-domain (FDTD) algorithm for modeling three-dimensional perfectly conducting objects. *IEEE Microwave Guided Wave Letters*, 7(9):273–275, September 1997.
- [65] W. Yu and R. Mittra. A conformal FDTD algorithm for modeling perfectly conducting objects with curve-shaped surfaces and edges. *Microwave and Optical Technology Letters*, 27(2):136–138, October 2000.
- [66] T. Xiao and Q. H. Liu. Enlarged cells for the conformal FDTD method to avoid the time step reduction. *IEEE Microwave and Wireless Components Letters*, 14(12):551–553, December 2004.
- [67] I. A. Zagorodnov, R. Schuhmann, and T. Weiland. A uniformly stable conformal FDTD-method in cartesian grids. *International Journal of Numerical Modelling*, 16:127–141, 2003.
- [68] J. Van Bladel. *Singular Electromagnetic Fields and Sources*. IEEE Press, 1991.
- [69] G. Mur. The modeling of singularities in the finite-difference approximation of the time-domain electromagnetic-field equations. *IEEE Transactions on Microwave Theory and Techniques*, MTT-29(10):1073–1077, October 1981.

- [70] D. B. Shorthouse and C. J. Railton. The incorporation of static field solutions into the finite difference time domain algorithm. *IEEE Transactions on Microwave Theory and Techniques*, 40(5):986–994, May 1992.
- [71] C. J. Railton. Use of static field solutions in the FDTD method for the efficient treatment of curved metal surfaces. *Electronics Letters*, 29(16):1466–1467, August 1993.
- [72] K. P. Esselle, M. Okoniewski, and M. A. Stuchly. Analysis of sharp metal edges at  $45^\circ$  to the FDTD grid. *IEEE Microwave Guided Wave Letters*, 9(6):221–223, June 1999.
- [73] S. M. Foroughipour and K. P. Esselle. The theory of a singularity-enhanced FDTD method for diagonal metal edges. *IEEE Transactions on Antennas and Propagation*, 51(2):312–321, February 2003.
- [74] Y.-I. Cho, D.-H. Choi, and S.-O. Park. FDTD analysis of bow-tie antenna by incorporating approximated static field solutions. *IEEE Antennas and Wireless Propagation Letters*, 3(1):176–179, December 2004.
- [75] C. J. Railton, D. L. Paul, I. J Craddock, and G. S. Hilton. The treatment of geometrically small structures in FDTD by the modification of assigned material parameters. *IEEE Transactions on Antennas and Propagation*, 53(12):4129–4136, December 2005.
- [76] H. Zscheile, F. J. Schmückle, and W. Heinrich. Finite-difference formulation accounting for field singularities. *IEEE Transactions on Microwave Theory and Techniques*, 54(5):2000–2010, May 2006.
- [77] T. Namiki. A new FDTD algorithm based on alternating-direction implicit method. *IEEE Transactions on Microwave Theory and Techniques*, 47(10):2003–2007, October 1999.
- [78] H. R. Schwarz. *Numerische Mathematik*. B. G. Teubner Stuttgart, 1997.

- [79] T. Namiki. 3-D ADI-FDTD method—Unconditionally stable time-domain algorithm for solving full vector Maxwell’s equations. *IEEE Transactions on Microwave Theory and Techniques*, 48(10):1743–1748, October 2000.
- [80] F. Zheng, Z. Chen, and J. Zhang. Toward the development of a three-dimensional unconditionally stable finite-difference time-domain method. *IEEE Transactions on Microwave Theory and Techniques*, 48(9):1550–1558, September 2000.
- [81] S. G. Garcia, T.-W. Lee, and S. C. Hagness. On the accuracy of the ADI-FDTD method. *Antennas and Wireless Propagation Letters*, 1(1):31–34, 2002.
- [82] Harald Songoro, Stefan Benkler, Nicolas Chavannes, and Niels Kuster. On the real world performance of ADI-FDTD. In *2005 IEEE AP-S/URSI International Symposium and USNC/URSI National Radio Science Meeting*, Washington DC, USA, July 2005. Poster, 3–8 July.
- [83] S. G. Garcia García, A. R. Bretones, R. G. Martín, and S. C. Hagness. Accurate implementation of current sources in the ADI-FDTD scheme. *IEEE Antennas and Wireless Propagation Letters*, 3(1):141–144, December 2004.
- [84] B. Donderici and F. L. Teixeira. Symmetric source implementation for the ADI-FDTD method. *IEEE Transactions on Antennas and Propagation*, 53(4):1562–1565, April 2005.
- [85] B. Donderici and F. L. Teixeira. Corrections to “symmetric source implementation for the ADI-FDTD method”. *IEEE Transactions on Antennas and Propagation*, 54(3):1051, March 2006.
- [86] A. P. Zhao. Uniaxial perfectly matched layer media for an unconditionally stable 3-D ADI-FD-TD method. *IEEE Microwave and Wireless Components Letters*, 12(12):497–499, December 2002.
- [87] S. D. Gedney, G. Liu, J. A. Roden, and A. Zhu. Perfectly matched layer media with CFS for an unconditionally stable

- ADI-FDTD method. *IEEE Transactions on Antennas and Propagation*, 49(11):1554–1559, November 2001.
- [88] G. Liu and S. D. Gedney. Perfectly matched layer media for an unconditionally stable three-dimensional ADI-FDTD method. *IEEE Microwave Guided Wave Letters*, 10(7):261–263, July 2000.
- [89] G. Sun and C. W. Trueman. Efficient implementations of the Crank-Nicolson scheme for the finite-difference time-domain method. *IEEE Transactions on Microwave Theory and Techniques*, 54(5):2275–2284, May 2006.
- [90] M. Chai, T. Xiao, and Q. H. Liu. Conformal method to eliminate the ADI-FDTD staircasing errors. *IEEE Transactions on Electromagnetic Compatibility*, 48(2):273–281, May 2006.
- [91] Y. Srisukh, J. Nehrbass, F. L. Teixeira, J. F. Lee, and R. Lee. An approach for automatic grid generation in three-dimensional FDTD simulations of complex geometries. *IEEE Antennas and Propagation Magazine*, 44(4):75–80, August 2002.
- [92] T. Su, Y. Liu, W. Yu, and R. Mittra. A conformal mesh-generating technique for the conformal finite-difference time-domain (CFDTD) method. *IEEE Antennas and Propagation Magazine*, 46(1):37–49, February 2004.
- [93] G. Waldschmidt and A. Taflove. Three-dimensional CAD-based mesh generator for the Dey-Mittra conformal FDTD algorithm. *IEEE Transactions on Antennas and Propagation*, 52(7):1658–1664, July 2004.
- [94] Acceleware Inc. <http://www.acceleware.com>.
- [95] ACIS®. <http://www.spatial.com/>.
- [96] S. Benkler, N. Chavannes, and N. Kuster. A new 3-D conformal PEC FDTD scheme with user-defined geometric precision and derived stability criterion. *IEEE Transactions on Antennas and Propagation*, 54(6):1843–1849, June 2006.

- [97] P. Futter, N. Chavannes, R. Tay, M. Meili, A. Klingenböck, K. Popovic, and N. Kuster. Reliable prediction of mobile phone performance under real usage conditions using the FDTD method. Presentation at the 2005 International Symposium on Antennas and Propagation (ISAP2005), Seoul, Korea, August 3–5, August 2005. Session TB2-1: Handset antennas II.
- [98] Jeen-Sheen Row, Shih-Huang Yeh, and Kin-Lu Wong. A broadband low-profile cylindrical monopole antenna. *Microwave and Optical Technology Letters*, 29(2):77–79, April 2001.
- [99] Stefan Benkler, Nicolas Chavannes, and Niels Kuster. Mastering conformal meshing for complex CAD based C-FDTD simulations. *IEEE Antennas and Propagation Magazine*, 2006 submitted.
- [100] Stefan Benkler, Nicolas Chavannes, and Niels Kuster. Versatile approach of incorporating subcell models into the 3-D ADI-FDTD method. *IEEE Transactions on Antennas and Propagation*, 2006 submitted.
- [101] Stefan Benkler, Nicolas Chavannes, Jürg Fröhlich, Harald Songoro, and Niels Kuster. Accurate representation of complex 3—D geometries for conformal FDTD simulations including solids and thin sheets. In *2004 AP-S/URSI International Symposium*, page 254, Monterey, California, June 2004.
- [102] Stefan Benkler, Harald Songoro, Nicolas Chavannes, and Niels Kuster. Robust and fully automated conformal mesh generation for complex conformal FDTD applications. In *2005 IEEE AP-S/URSI International Symposium and USNC/URSI National Radio Science Meeting*, Washington DC, USA, July 2005. Poster, 3–8 July.
- [103] Stefan Benkler, Harald Songoro, Nicolas Chavannes, and Niels Kuster. Automated and robust conformal mesher for complex conformal FDTD applications. In *Progress In Electromagnetics Research Symposium (PIERS)*, volume Abstracts, page 170, Hangzhou, China, August 2005. The Electromagnetics Academy, MA. Session 2P5b: FDTD.

- [104] Harald Songoro, Stefan Benkler, Nicolas Chavannes, and Peter Futter. The real-world performance of staircased and conformal ADI-FDTD. In *Progress in Electromagnetics Research Symposium (PIERS)*, volume Abstracts, page 165, Hangzhou, China, August 2005. The Electromagnetics Academy. Session 2P5b: FDTD.
- [105] S. Benkler, N. Chavannes, and N. Kuster. New conformal PEC FDTD model with user-defined geometric precision and derived stability criterion. In *28th Annual Meeting of the Bioelectromagnetics Society*, pages 147–148, Cancun, Mexico, June 2006. PA-141 in Poster Session A, (12 June).
- [106] S. Benkler, N. Chavannes, and N. Kuster. Three-dimensional conformal alternating direction implicit finite-difference time-domain solver (C-ADI-FDTD). In *28th Annual Meeting of the Bioelectromagnetics Society*, pages 363–364, Cancun, Mexico, June 2006. PB-142 in Poster Session B, (13 June).
- [107] Stefan Benkler, Nicolas Chavannes, and Niels Kuster. New conformal PEC FDTD model with user-defined geometric precision and derived stability criterion. In *Final Program of the 2006 IEEE Antennas and Propagation Society International Symposium with USNC/URSI National Radio Science Meeting*, page 508, Albuquerque, NM USA, July 2006. July 12, Poster # 381.7 in Session 381: Posters Different EQ Methods: Advances in FDTD (URSI).
- [108] Stefan Benkler, Nicolas Chavannes, and Niels Kuster. Three-dimensional conformal alternating direction implicit finite-difference time-domain solver (C-ADI-FDTD). In *Final Program of the 2006 IEEE Antennas and Propagation Society International Symposium with USNC/URSI National Radio Science Meeting*, page 507, Albuquerque, NM USA, July 2006. July 12, Poster # 381.6 in Session 381: Posters Different EQ Methods: Advances in FDTD (URSI).
- [109] Stefan Benkler. Dielectric subcell models. Technical report, IT'IS Foundation for Research on Information Technologies in Society, 8004 Zürich, Switzerland, April 2004.

- [110] Stefan Benkler and Jürg Fröhlich. Behaviour of electromagnetic fields at lossy material boundaries. Technical report, IT'IS Foundation for Research on Information Technologies in Society, 8004 Zürich, Switzerland, August 2003.

# Curriculum Vitae

## Education

- Dipl. Rech. Wiss. ETH, degree 2002  
ETH Zürich, Switzerland  
Major: Computational Fluid Dynamics
- Dipl. Ingenieur Mikrotechnik, degree 1997  
Ingenieurschule Biel, Switzerland
- Apprenticeship as Maschinenmechaniker, 1990–1994  
Lehrwerkstätten der Stadt Bern, Switzerland
- Secondary School, 1985–90  
Niederscherli, Switzerland
- Primary School, 1981–85  
Niederscherli, Switzerland

## Professional Experience

- Graduate Research Assistant, 10/2002–present  
Laboratory of Integrated Systems  
Faculty of Electrical Engineering, ETH Zürich, Switzerland
- Traineeship, 2000, 2 months  
Simulation of Surface Charges in Proton Beam Simulation  
Dr. Adelman, PSI Villigen, Switzerland
- Undergraduate Research Assistant, winter term 1999/2000  
Linear Algebra and Numerical Mathematics  
Prof. Stoffer, ETH Zürich, Switzerland

Teacher at TEKO (Technikerschule), 1999–2000  
Mathematics, 4 lectures per week, 2 terms  
TEKO, Bern, Switzerland

**Personal Data**

Date of Birth: 4 June 1974  
Citizenship: Swiss  
Parents: Ruth and Thomas Benkler